

Modeling and characterization of wire harnesses for digital  
manufacturing applications

Dissertation

Presented in Partial Fulfillment of the Requirements for the Degree  
Doctor of Philosophy in the Graduate School of The Ohio State  
University

By

Sai Siddhartha Vemula, B.S., M.S.

Graduate Program in Department of Mechanical Engineering

The Ohio State University

2021

Dissertation Committee:

Dr. Marcelo Dapino, Advisor

Dr. Soheil Soghrati

Dr. Noriko Katsube

© Copyright by  
Sai Siddhartha Vemula  
2021

## **Abstract**

Digital manufacturing is the use of an integrated, computer-based system comprised of simulation, 3D visualization, analytics, and collaboration tools to simultaneously create product and manufacturing process definitions. Digital manufacturing has become more feasible with the rise in the quantity and quality of computer systems. The advantage of digital manufacturing is the ability to modify or create manufacturing procedures within a virtual and controlled environment before being physically implemented. This enables the designers to see the results of their procedure before investing in physical products. The focus of this work is digital manufacturing of automotive wire harnesses. Current digital manufacturing software lack the ability to accurately simulate flexible components such as cables, hoses, and harnesses. The specific purpose of this work is to develop experimental procedures to characterize wire harnesses and obtain homogenized material properties for incorporation into digital manufacturing software. Experimental procedures are presented to characterize harness components and harness bundles. The different sizes of the components and various possible combinations of harness bundles make it difficult to experimentally characterize each one of them. Hence, limited experiments were conducted, and analytical models are proposed to characterize the components and use the available test data to validate the models. This research can fundamentally

change the way harnesses are manufactured, designed and assembled. The experimental characterization and analytical models will help in harness routing, designing correct harness lengths to reduce vibration and rattling, residual stresses, and mechanical failure.

This is dedicated to my parents

## Acknowledgments

The work presented in this dissertation has been possible through guidance and support from a number of people. I would like to thank Prof. Marcelo Dapino, Prof. Soheil Soghrati, Prof. Noriko Katsube, and Prof. Herman Shen for serving on my Ph.D. committee. My Ph.D. journey has been an enriching experience thanks to my advisor, Prof. Marcelo Dapino. His guidance has been invaluable on all fronts ranging from developing research ideas to honing my communication and presentation skills. I Would also like to thank Dr. Leon Headings for his creative ideas and critical feedback of my research. Our brainstorming sessions and his attention to detail in our papers have been of great help, especially early on in my research.

I thank Honda Research Americas (Marysville, OH) for initiating my research project, especially Mr. Kushal Gargesh and Mr. Allen Sheldon. I would like to thank the member organization of the NSF IUCRC Smart Vehicle Concepts center for funding me as a Graduate Research Associate.

I would like to thank all the MAE staf for supporting me throughout my graduate program. Special thanks to SVC staff Tommie Blackledge, graduate advisors Janeen Sands and Nick Breckenridge, machine shop staff Chad Bivens, Joe West, and Aaron Osborn. It has been a pleasure to work with my colleagues at the Smart Materials and Structures Lab. These highly-motivated individuals have fostered a work culture that is ideal for sharing each other's ideas and providing feedback. I would like to

especially thank Dr. Venkata Siva Chaitanya Chillara and Yitong Zhou for teaching me to use the various instruments in the lab. Other students I have worked with are too many to list here but I would like to mention Bryant Gingerich, Tianyang Han, Gowtham Venkatraman, Hongqi Guo, Arun Ramanathan, Ismail Nas, Brad Losey, and Shuting Wang.

This research would not have been possible without the support from my friends and family. I am very grateful to my parents, brother, cousins, and grandparents for their unconditional love and encouragement throughout my academic pursuit.

## Vita

January 26, 1993 ..... Born - Khammam, India

2015 ..... B.Tech. Indian Institute of Technology  
Madras

2019 ..... M.S. Ohio State University

2015-present ..... Graduate Research Associate,  
The Ohio State University.

## Publications

### Research Publications

S. S. Vemula, M. Ji, L. M. Headings, K. Gargesh, S. Soghrati, M. J. Dapino “Analytical model for large deflection bending of helically stranded electrical wires”. *International Journal of Mechanical Sciences*, 105355, Mar. 2020.

E. Taghipour, S. S. Vemula, K. Gargesh, L. M. Headings, M. J. Dapino, S. Soghrati “Finite element analysis of mechanical behavior of electrical wire harnesses: High fidelity and reduced-order models”. *International Journal of Mechanical Sciences*, 105188, Jan. 2020.

E. Taghipour, S. S. Vemula, Z. Wang, Y. Zhou, H. Qarib K. Gargesh, L. M. Headings, M. J. Dapino, S. Soghrati “Characterization and computational modeling of electrical wires and wire bundles subject to bending loads”. *International Journal of Mechanical Sciences*, 211-277, May 2018.

## **Fields of Study**

Major Field: Department of Mechanical Engineering

Studies in:

Experimental Mechanics  
Computational Mechanics

# Table of Contents

	<b>Page</b>
Abstract . . . . .	ii
Dedication . . . . .	iv
Acknowledgments . . . . .	v
Vita . . . . .	vii
List of Tables . . . . .	xii
List of Figures . . . . .	xiv
1. Introduction . . . . .	1
1.1 Background and motivation . . . . .	1
1.2 Modeling of wire harnesses . . . . .	2
1.3 Mechanical characterization of wire harnesses . . . . .	4
1.4 Analytical modeling of electrical wires . . . . .	6
1.5 Dissertation outline . . . . .	8
2. Characterization of individual components . . . . .	10
2.1 Electrical wire . . . . .	11
2.1.1 Test setup . . . . .	12
2.1.2 Motion capture system . . . . .	15
2.1.3 Results and discussion . . . . .	17
2.2 Protective conduits . . . . .	20
2.2.1 Corrugated tube test setup . . . . .	21
2.2.2 Corrugated tube results . . . . .	23
2.2.3 Twist tube setup . . . . .	26
2.2.4 Twist tube results . . . . .	28

2.3	Insulation tape . . . . .	30
2.3.1	Test setup . . . . .	31
2.3.2	Results . . . . .	31
3.	Wire Analytical Model . . . . .	33
3.1	Wire geometry . . . . .	34
3.2	Stick-slip model . . . . .	37
3.2.1	Stick state . . . . .	37
3.2.2	Slip state . . . . .	38
3.2.3	Plastic state . . . . .	41
3.3	Large deflection formulation . . . . .	43
3.4	Model calibration and evaluation . . . . .	45
3.5	Comparison with FEA . . . . .	51
3.6	Application . . . . .	54
4.	Wire harness characterization . . . . .	59
4.1	Introduction . . . . .	60
4.2	Taped wire bundles . . . . .	60
4.2.1	Sample preparation . . . . .	60
4.2.2	Test setup . . . . .	63
4.2.3	Results . . . . .	64
4.3	Conduit wire bundles . . . . .	70
4.3.1	Sample preparation . . . . .	71
4.3.2	Test setup . . . . .	71
4.3.3	Results . . . . .	73
5.	Conclusion . . . . .	77
5.1	Summary of findings . . . . .	77
5.2	Contributions . . . . .	79
	Appendices . . . . .	81
A.	MATLAB Codes . . . . .	81
B.	Cosserat simulation of wire harnesses . . . . .	112
B.1	Introduction . . . . .	112
B.2	Modeling framework . . . . .	113

B.3 Preliminary results . . . . .	115
-----------------------------------	-----

## List of Tables

<b>Table</b>		<b>Page</b>
2.1	Wire diameter, conductor area, number of conductors, lay angles of the conductors, sample lengths, and conductor layouts of the five types of wires tested. A-type wires have cylindrical conductors and B-type wires have compressed conductors. . . . .	12
2.2	Inner diameter, outer diameter, and wall thickness of the three types of corrugated tubes tested. . . . .	23
2.3	Normalized liner stiffness of the twist tube. . . . .	29
3.1	Initial and optimized values of analytical model parameters: radial force exerted by the insulation ( $F_{rad}$ ), inter-conductor friction coefficient ( $\mu_s$ ), and insulation-conductor friction coefficient ( $\mu_p$ ). . . . .	46
3.2	Stick-state bending stiffness of the wires as calculated by the analytical model. . . . .	50
3.3	Sum of squared errors (SSE) and root of mean squares of error (RMSE) for the analytical model relative to experimental measurements. All of the wire types have an error $\ll 1$ , indicating that the analytical model provides a good fit. . . . .	51
3.4	Wire diameter, conductor area, number of conductors, and lay angles of the conductors of the five types of wires characterized using the analytical model. . . . .	57
3.5	Stick-state bending stiffness and predicted cross section of the five different sizes of C-type wires. . . . .	58
4.1	Types of taped wire bundles tested as part of this study. . . . .	61

4.2	Types of composite wire bundles tested as part of this study. . . . .	70
-----	---	----

## List of Figures

Figure	Page
1.1 An automotive wire harness showing the various components of the harness. . . . .	3
2.1 Architecture of a typical helically-wound stranded electrical wire modeled in this paper. . . . .	11
2.2 Cantilever bending setup. . . . .	14
2.3 (a) Initial and (b) final shapes of a wire sample during the cantilever bending test used for model development. . . . .	15
2.4 Motive software interface. . . . .	16
2.5 (a) Raw and (b) filtered force versus displacement data for cantilever bending test of A1-type wire. . . . .	17
2.6 Motion capture of an A1-type wire under cantilever bending. . . . .	18
2.7 Force versus displacement data for cantilever bend test of A1-type wire samples showing the mean and the 95% confidence interval. . . . .	19
2.8 Force versus displacement data for cantilever bending tests of (a) A2-type and (b) A3-type wires. . . . .	19
2.9 Force versus displacement data for cantilever bending test of (a) 85 mm and (b) 100 mm long B1-type wire samples. . . . .	20
2.10 Force versus displacement data for cantilever bending test of (a) 85 mm and (b) 100 mm long B2-type wire samples. . . . .	20

2.11	Typical automotive wire harness. . . . .	21
2.12	(a) Initial and (b) final stage of 10 mm diameter corrugated tube tensile test. . . . .	22
2.13	Preparation of corrugated tube tensile test samples. . . . .	24
2.14	Force versus displacement data for tensile testing of (a) slit and (b) unslit corrugated tube with 10 mm inner diameter. . . . .	24
2.15	Force versus displacement data for tensile testing of 7 mm diameter unslit corrugated tube. . . . .	25
2.16	Twist tube test setup schematic showing the sample and the setup. .	26
2.17	(a) Initial and (b) final state of 10 mm diameter twist tube tensile test.	27
2.18	The six samples of the twist tube tested. . . . .	28
2.19	Normalized force versus displacement plot of the twist tube tensile test showing the six samples tested. . . . .	29
2.20	Characterizing the twist tube tensile stiffness from the normalized force versus displacement plot. . . . .	30
2.21	Polyethylene (PET) tape sample. . . . .	31
2.22	Polyethylene (PET) tape tensile test setup showing the load frame and the mounting grips. . . . .	32
2.23	Normalized load versus displacement plots for tensile testing of polyethylene (PET) tape. . . . .	32
3.1	(a) Initial guess for conductor configuration; (b) optimized conductor configuration obtained using a circle packing algorithm. The dashed circle represents the inner surface of the insulation and the solid circles represent the outlines of the individual conductors. . . . .	34
3.2	Estimated and actual cross sections of a typical (a) 7-conductor wire and (b) 19-conductor wire. . . . .	36

3.3	Static force diagram for a differential element of the $p^{th}$ conductor in the $q^{th}$ layer subjected to an axial force $F_{p,q}$ , normal forces $H_{p,q}$ and $G_{p,q}$ from adjacent layers, friction forces $h_{p,q}$ and $g_{p,q}$ resulting from relative sliding of adjacent layers, and the resulting increment in axial force $dF_{p,q}$ . . . . .	39
3.4	(a) Cross section of a generic beam showing a layer of differential thickness $dy$ ; (b) stress distribution across a beam's cross section for elastic and elasto-plastic bending, showing stress reduction due to plasticity.	42
3.5	Large deflection bending of a cantilever beam subjected to a point load at its free end, showing the beam length $L$ and the projected length $l$ .	44
3.6	(a) Measured and simulated force versus displacement curves for cantilever bending of A2-type wire and (b) measured wire marker locations (dots), polynomial fits of marker locations (dashed lines), and the simulated wire shapes (solid lines) at various bending intervals. . . . .	47
3.7	Bending stiffness versus curvature for the three A-type wires showing the difference in stick, slip, and plastic regions of the wires. A3-type wire has a more gradual transition from stick to slip state due to having two layers compared to a single layer for A1 and A2-type wires. . . .	48
3.8	Measured and simulated force versus displacement curves for (a) A1-type wire (sample length = 85 mm) and (b) A3-type wire (sample length = 120 mm). . . . .	48
3.9	Measured and simulated force versus displacement curves for (a) 85 mm and (b) 100 mm long samples of B1-type wire. . . . .	49
3.10	Measured and simulated force versus displacement curves for (a) 85 mm and (b) 100 mm long samples of B2-type wire. . . . .	50
3.11	FE models of (a) A2-type and (b) B2-type wires showing portions of the mesh and simulated bent shape of the wires. . . . .	52
3.12	Force versus displacement plots showing the experimental data, analytical model output, and FE model output for wires (a) A2 and (b) B2. . . . .	53

3.13	Von Mises stress distribution at the fixed end for (a) A2-type and (b) B2-type wires. The symmetric stress distribution in each wire supports the laminated stress distribution assumption presented in subsection 3.2.3. . . . .	54
3.14	Logic flow of the analytical model. . . . .	56
4.1	Taped wire B1 bundle mounted in drill chucks for taping. . . . .	61
4.2	Schematic showing taping wire bundle cross sections for different number of wires. . . . .	62
4.3	TWB sample preparation and setup showing the epoxy cast, polycarbonate clamp and the mounting of the sample. . . . .	63
4.4	(a) Initial and (b) final stage of cantilever bending test of taped wire bundle. . . . .	64
4.5	(a) Normalized force versus displacement and (b) motion capture data for cantilever bending test of B1-type nineteen wire bundle. . . . .	65
4.6	Plot showing the normalized force versus displacement of (a) B1-type and (b) B2-type seven-wire bundles. . . . .	66
4.7	Plot showing the normalized force versus displacement of (a) B1-type and (b) B2-type twelve-wire bundles. . . . .	66
4.8	Plot showing the normalized force versus displacement of (a) B1-type and (b) B2-type nineteen-wire bundle. . . . .	67
4.9	Mixed TWB samples showing two different configurations of the wire bundles. . . . .	68
4.10	Normalized force versus displacement plots of two different cases of mixed wire TWBs. . . . .	68
4.11	Plot showing the normalized force versus displacement of (a) B1-type and (b) B2-type nineteen-wire bundle with PET tape. . . . .	69
4.12	Conduit wire bundle test setup showing the load frame, fixtures, data acquisition, and motion capture system. . . . .	72

4.13	(a) Initial, (b) fully bent, and (c) final shape of a conduit wire bundle under three-point-bending. . . . .	74
4.14	Normalized force versus displacement and motion capture plot of a B1-type nineteen-wire CWB sample. . . . .	74
4.15	Normalized force versus displacement of a B2-type 19-wire CWB sample. The three cases of no tape, coarse tape, and half-lap tape are shown . . . . .	75
4.16	Normalized force versus displacement of B2-type twelve-wire sample and a mixed wire CWB sample. . . . .	76
4.17	Normalized force versus displacement of B1-type and B2-type nineteen-wire CWB samples made with twist tube. . . . .	76
B.1	Proposed harness simulation framework. . . . .	113
B.2	A discrete Cosserat rod. . . . .	114
B.3	(a) The initial and final shape of a chain being lifted off a table and (b) the variation in the chain length. . . . .	115

# **Chapter 1: Introduction**

## **1.1 Background and motivation**

Automobiles have multiple electronic, electrical, and electro-mechanical systems connected by a network of electrical wire harnesses. The function of a wire harness is similar to the nervous system in a human body, i.e., the wire harness allows the exchange of information between various components of an automobile in the form of electrical signals. Wire harness related issues are a root cause of a significant number of customer-reported problems [8]. Additionally, increasing vehicle electrification due to technological advances has increased the complexity of wire harnesses [34]. This has increased the demand for reliable wire harnesses capable of maintenance free operation. Additionally, shorter development periods and reduced number of prototypes has also called for a greater efficiency in harness design. This can be achieved with digital manufacturing tools to identify and mitigate any performance issues that may arise during and after manufacturing. Digital manufacturing also helps to identify variability in harness features such as excess harness lengths or insufficient tape layers, neither of which damage the harness but can cause unwanted noise due to rattling.

Digital manufacturing is the computer simulation of the assembly process, where a digital mock-up of the actual assembly process is performed before moving on to the

prototyping stage. Automotive companies specifically use a range of commercial software such as CATIA, IPS, and IC.IDO for this purpose. However, current commercial software is intrinsically inaccurate for mechanical modeling of wire harness networks since they typically assume linear elasticity, whereas in practice, harnesses are complex multi-material structures that undergo elasto-plastic deformations. Hence, there is a need to accurately model the elasto-plastic response of harness components for use in digital manufacturing applications. Another issue to be addressed is the lack of accurate material properties for use in the modeling software. Wire harnesses are typically designed for their electrical performance, hence, the mechanical behavior of wire harnesses is often neglected. This creates a need to design experiments to characterize and study the mechanical behavior of harness components under different loading modes. In this thesis, experimental techniques are presented to mechanically characterize the wire harness components.

## **1.2 Modeling of wire harnesses**

A typical wire harness is made of various components such as electrical wires, protective conduits, insulation taping, and mounting clips as shown in Figure 1.1. Studies on wire harnesses have predominantly focused on reducing the manufacturing cost and installation time. Narayana et. al. [28] have simulated the wire harness assembly and have concluded that the performance of a wire harness is not affected even after experiencing high forces during installation. Hermansson et. al. [15] performed a study on the installation of flexible pipes and cables and have developed methods to reduce the propagation of uncertainties in the object shape during installation. [15] assumed the the cables as flexible 1D structures which can undergo

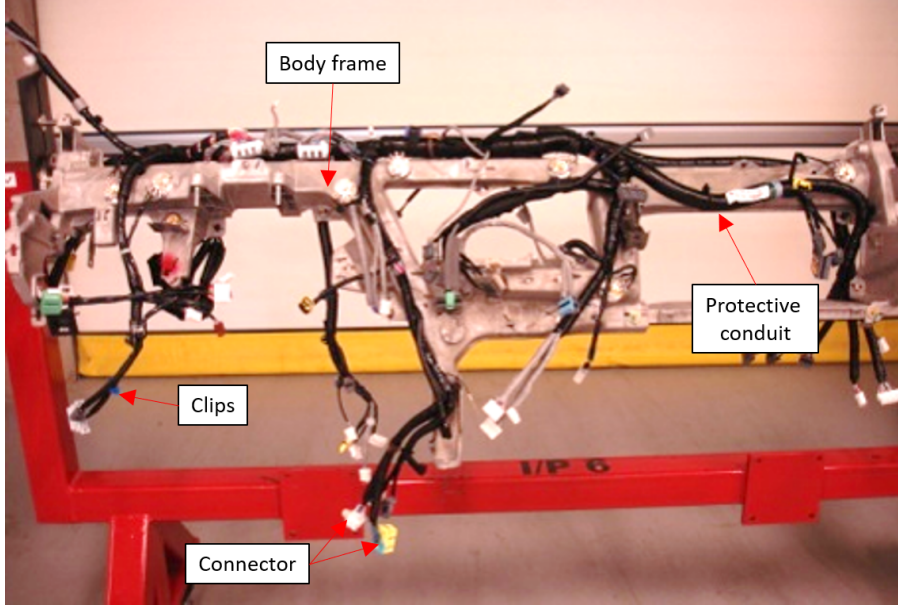


Figure 1.1: An automotive wire harness showing the various components of the harness.

large deflection. Theetten et al [40] developed a model to simulate the mechanical behavior of 1D slender objects by taking into account tension, bending and torsion. They modeled the cables as geometrically exact splines and the model was validated with the a cable position system to compare the actual and simulated cable shape.

Kim et al. [23] performed fatigue analysis of an automotive door wire harness. The door was operated at a frequency of 10 closures/min and the wires stiffness was measured every 10,000 cycles for a total of 350,000 cycles. The experimental results were compared with FEM of door harness in both cases, larger wire harnesses showed longer life. But their FEA modeled the wire harnesses as bare copper wires enclosed in a tube and both the wires and the tube were assumed to have similar mechanical properties, which is not accurate for wiring harness. Goebbels et al. [12] studied the dynamic behavior of wire harnesses by modeling the harness as a 1D beam. Their

model takes into account the effect of contact on the dynamic simulation. However, the material properties of the harnesses were calculated analytically without experimental validation. Spak et al. [36] modeled the vibration response of an aircraft cable harness using a distributed transfer function and also included hysteretic damping. They presented a new method to model the stiffness of a harness mounting points and experimentally validated the model on four different harness configurations.

### **1.3 Mechanical characterization of wire harnesses**

Previous studies on the mechanical behavior of wire harnesses have focused mainly on computer simulation with inadequate experimental validation. The simulations were inaccurate due to the lack of proper mechanical properties such as Young's modulus and Poisson's ratio. Wright et al.[46] performed experiments on stripped single core electrical wires to measure the Young's modulus of the conductor and compared the results of the tensile testing with analytical calculation of the Young's modulus. However, the analytical calculations are based on the rule of mixtures between copper and PVC and only works for small deflections. Hence, there is a necessity to develop experiments to characterize the electrical wires with insulation.

Many experimental studies have been performed on multi-strand conductors, wire ropes, electric cables, and transmission lines. This is due to the fact that wire-rope structures are used in load bearing applications such as cable swayed bridges and electrical transmission lines. These cables typically undergo combined loading, i.e. both tension and bending. McConnell and Zemke [27] developed three different test methods to measure the static bending stiffness of a cable structure. They tested several ACSR wire strands and tabulated the bending stiffness for two extreme cases:

stick state and slip state. In stick state the conductor strands are in contact with one another and the cable behaves as a homogeneous structure. In slip state the conductor strands freely slip against each other and each conductor behaves as an individual beam. These cases represent the highest and lowest possible bending stiffness of a cabled structure.

Papailiou [32] designed a similar test setup though his model takes into account the effect of friction through a function which can be used to measure the bending stiffness at all states between the stick and slip states. In this experimental setup, a laser sensor was used to measure the deflection curve of the conductor. The sensor was set to scan 800 points on the conductor surface and the scans are repeated every few millimeters. Inagaki et al. [19] designed an experiment setup with an ACSR cable fixed at both ends and a compressive force is applied to the upper end so that the cable is bent in the shape of a circular arc. A load cell at the upper end of the cable is used to measured the force. They compared the bending stiffness vs curvature response between theoretical and experimental results in the curvature range between 1 and 10, which showed a good match. However, the experimental results are not shown for small curvatures since the measured data was affected due to residual stress.

Colozza [5] designed three point bending tests to measure the flexibility of wire or cable used on a lunar rover. They performed tests at both room temperature and extreme cold conditions (similar to the moon). The bending test results were used to estimate the torque required to unwind the harness at extreme temperatures. Van der Heijden et al. [42] studied the mechanical behavior of pre-twisted rods undergoing large axial deformations. Force and torque transducers were used at both ends of a wire to measure the torque and the tensile force. Goss et al. [13] extended the

above experiment by applying both axial and torsional deformation. Dörlich et al. [9] studied heterogeneous cabled structures made with strands of various materials. They concluded that increasing the torsion decreases the tensile stiffness and vice versa. Rothenburg et al. [35] designed a more complex experiment setup where the cables were simultaneously loaded in bending, torsion, and compression..

Wienss et al. [45] designed a test to simultaneously apply both the bending and torsion. But, the test measured only the torsion and not the bending moment. Hence, there was a disagreement between the model and the experiment results. They also neglected the effect of friction. Automotive harnesses undergo combined loading with predominately bending. Hence, uni-axial tensile tests are not sufficient to characterise a harness and their components.

## 1.4 Analytical modeling of electrical wires

Electrical wires are key building blocks of wire harnesses and a starting point for addressing the complex structure of wire harnesses. A typical electrical wire is made by helically winding conductors around a core in one or multiple layers, and then encasing them in polymeric insulation. Harnesses are predominantly subjected to bending loads during the assembly process [20], so this modeling effort focuses on the bending response of wires.

Costello [6] proposed a model for bending of wire ropes with single layers, which posits that the bending stiffness reaches a minimum value corresponding to the slip state. This model was generalized for wires with complex cross sections by Velinsky [43]. However, neither of these models includes the effect of interlayer friction.

Lanteigne [25] formulated a general stiffness matrix for aluminum conductor steel reinforced (ACSR) cables subjected to bending, torsion, and elongation which includes only the contribution of radial force towards interlayer friction. Papailiou [32] presented a model for bending of ACSR cables taking into account interlayer friction and derived a moment-curvature relationship. Hong et al. [17] have modified the model by including the change in inter-layer lay angle for calculating the radial contact forces.

Inagaki et al. [19] extended Papailiou's model to second-order helical cables and modeled the effect of axial and torsional forces on the bending moment of wire conductors, incorporating a model for the contact between insulation and conductors. Foti and Martinelli [11] extended this model by including the effect of residual radial contact forces between layers and also proposing a substantially different approach to evaluate the axial force in the wires. Another extension of Papailiou's model is presented in Foti and Martinelli [10], which accounts for the coupled axial-bending behavior of wire ropes. Jiang et al. [21] presented a finite element model to predict the elasto-plastic behavior of a straight wire under pure bending loads. In our previous work [39], a methodology was presented to determine Holloman's material constants [16] for homogenized electrical wires.

A new analytical formulation is presented in this research work for large deflection elastic-plastic bending of electrical wires. The overall bending behavior of the electrical wire is modeled based on Euler-Bernoulli beam theory [24]. The friction between conductors is defined using Amontons-Coulomb friction laws. The kinematic state of the wire is determined by comparing stick and slip axial forces acting on each conductor. Plasticity is modeled by treating the conductors as laminated composite

beams with each lamina having a different bending modulus. The change in helix angle is neglected since the conductors are enclosed in insulation, which limits twisting of the helix and separation of the conductors. The total bending moment of the wire is the sum of moments in the individual conductors and the insulation.

An effective bending stiffness versus curvature relation is derived by homogenizing the wire as a cylindrical beam. The effective bending stiffness can then be used in digital manufacturing applications. An algorithm for packing circles in a circle [18] is used to determine the conductor layout in the wire cross section, i.e., the radial and angular positions of the conductors in the cross-section. This is required as most manufacturers of electrical wires (e.g., [26]) specify only the number of conductors in a wire, but the arrangement of conductors needs to be known to model the forces acting on individual conductors. The packing algorithm and the analytical model together form a tool to automate the process of determining the bending stiffness for an arbitrary number of electrical wires based on their geometric and material properties.

## 1.5 Dissertation outline

This thesis presents the design and modeling of experiments to characterize the mechanical properties of automotive wire harnesses and their components. The discussion of these topics is broken up into 4 chapters. Chapter 2 presents methods to characterize the wire harness components such as electrical wires, conduits and insulation tape. Chapter 3 explains the analytical formulation to model the elasto-plastic bending behavior of helical electrical wires subjected to large deflections. Chapter 4 presents methods to characterize harness bundles such as taped wire bundles and

conduit wire bundles. The wire bundles help in understanding the effect of various components on the bundle stiffness and also the interactions between components. Concluding remarks are presented in Chapter 5.

## Chapter 2: Characterization of individual components

### Overview

*This chapter introduces methodologies to characterize the individual components of a wire harness such as the electrical wires, protective conduits, and insulation tape. A Wire harness is typically designed for its electrical performance. Hence, there exist no standards for characterizing the mechanical behavior of harness components. As a result, the literature for mechanical characterization of harness components is limited. The experimental methods were developed based on modeling requirements and ASTM standards.*

## 2.1 Electrical wire

A typical electrical wire is made by helically winding copper conductors around a core in one or multiple layers, and then encasing them in a polymeric insulation (Figure 2.1). Two types of electrical wires were tested in this study, namely type A and type B. The dimensions of the wires tested in this dissertation are shown in Table 2.1.

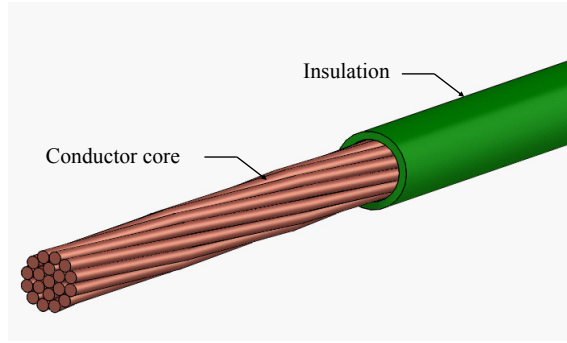







Figure 2.1: Architecture of a typical helically-wound stranded electrical wire modeled in this paper.

A-type wires have cylindrical conductors and are used for low voltage applications, whereas B-type wires have compressed conductors and used in applications with space constraints as compressed conductors ensure a higher electrical performance with thinner wires. For example, A2-type and B2-type wires have a similar conductor cross-section area but the diameter of B2-type wire is 25% less than that of A2-type wire.

Table 2.1: Wire diameter, conductor area, number of conductors, lay angles of the conductors, sample lengths, and conductor layouts of the five types of wires tested. A-type wires have cylindrical conductors and B-type wires have compressed conductors.

Wire	$d_w$ (mm)	$A_c(\text{mm}^2)$	$N_s$	$\alpha_q(^{\circ})$	L (mm)	Cross-section
A1	1.4	0.37	7	12	85	
A2	1.6	0.56	7	12	85	
A3	1.8	0.86	19	12, -15	85	
B1	1.1	0.35	7	12	85, 100	
B2	1.25	0.49	7	12	85, 100	

Wire harnesses are predominantly subjected to bending loads during the assembly process [20], so this section focuses on characterizing the response of wires subjected to such loads. Hence, a custom inverted cantilever bending test is designed to characterize the bending behavior of electrical wires. In this test, one end of the wire is fixed and a vertical load is applied on the other end. The load displacement data obtained from this test is used in the analytical modeling of the electrical wires presented in Chapter 3.

### 2.1.1 Test setup

Figure 2.2 shows the cantilever bending test setup. A support frame was built from aluminum Unistrut. Figure 2.3 shows the test setup in detail including the load frame and wire initial and bent states. One end of the wire sample is clamped in an adapter creating the fixed boundary condition, and the adapter is mounted on a shaft connected to a stepper motor. The stepper motor provides displacement to the

fixed end of the cantilever beam. A 2g Cooper load cell is fixed to the upper Unistrut beam and a 760 mm long aramid strand connects the load cell and free end of the wire. Cyanoacrylate glue was used to attach the aramid strand to the wire, to ensure the connection is intact during the test. A 2.7 g counterweight was tied to the end of the wire to eliminate any slack in the aramid strand and keep the wire sample straight. A dSPACE 1103 control box is used to control the stepper motor and to record tension in the aramid strand as measured by the load cell.

Additionally, the shape of the wire sample during bending and the tip displacement are measured with a motion capture system. This avoids error due to the possibility of missing stepper motor steps at low speeds. The data is sampled at 10 kHz. A Simulink model was designed to control the speed and direction of the stepper motor. The frequency to actuate the motor was set up to be 8000 Hz so that the vertical speed of the motor is 1 mm/s (2.4 in/min). The loading time was set up as 53 secs so that the vertical displacement is 53 mm. Here, 53 mm is the travel limit of the load frame.

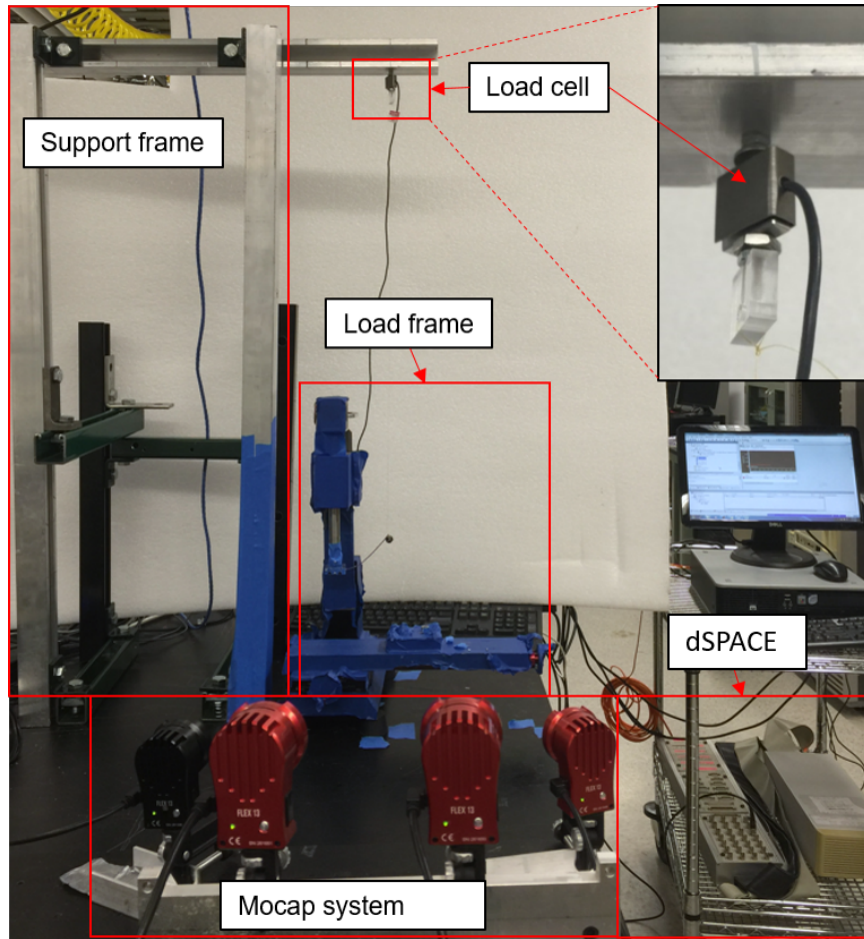


Figure 2.2: Cantilever bending setup.

The procedure of the test is:

1. Cut a sample with an appropriate length from a spool and gently straighten it
2. Stick Infrared (IR) reflective tape markers along the length of wire sample
3. Mount one end of the wire sample in the adapter
4. Connect the free end of the wire sample to the load cell with an aramid fiber and hang the counterweight to the free end

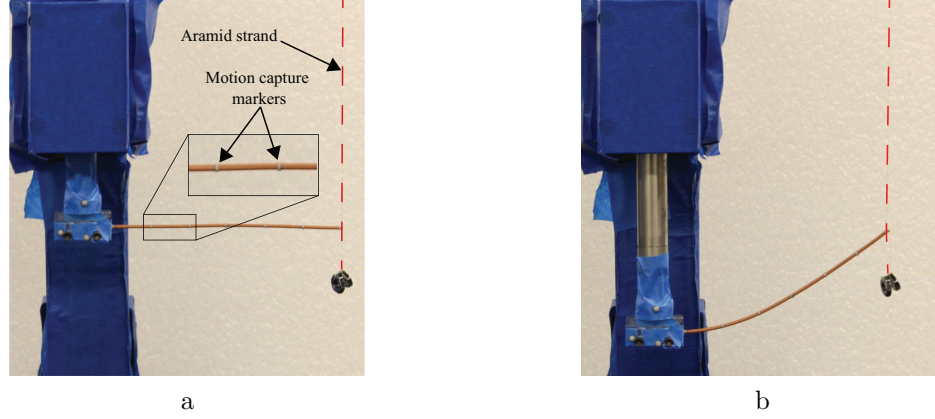


Figure 2.3: (a) Initial and (b) final shapes of a wire sample during the cantilever bending test used for model development.

5. Use cyanoacrylate glue on the tie
6. Simultaneously start the test in dSPACE ControlDesk software and the motion capture process
7. Output the force vs. displacement plots and motion capture output

### 2.1.2 Motion capture system

An OptiTrack motion capture system is used to record the shape of the wire as it undergoes deflection. The system consists of 10 OptiTrack Flex 13 cameras. These cameras have 1.3 MP resolution, 56 degrees of field of view, can measure up to 4 ft distance, and can record up to 120 frames per second [30]. Each camera has 28 infrared (IR) LEDs. The light emitted from these LEDs reflects off the markers placed on the sample and the reflected IR light is used by the cameras to measure the position of the marker. Using the measurements from multiple cameras, the exact position of the marker can be determined by the principle of triangulation.

Cameras are placed strategically such that each marker is in the field of view of at least three cameras [29]. The camera setup is shown in Figure 2.2. The software used for motion capture is Motive, which is an optical motion capture software developed by OptiTrack. Figure 2.4 shows the interface of the Motive software.

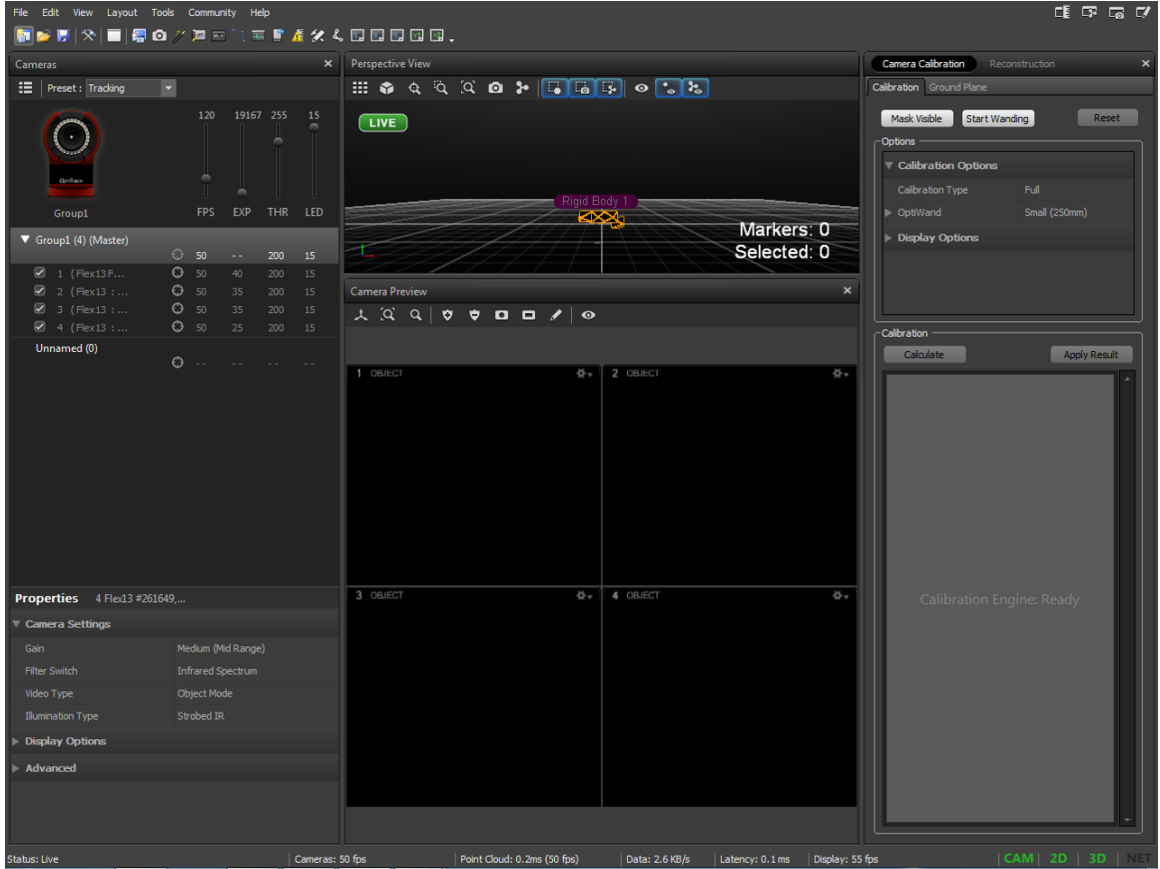


Figure 2.4: Motive software interface.

The distance between the reflective markers need to be at least  $3\times$  the marker size so as not to confuse the cameras. The mocap system records the coordinates of

the center of the marker. Hence, the data needs to be adjusted to account for the measurement error arising from the marker size.

### 2.1.3 Results and discussion

Three samples of each wire type were tested. Each sample was loaded and unloaded for three cycles. The force data was sampled at 10 kHz. The noise was filtered during post-processing using a moving average filter in MATLAB. Figure 2.5 shows the raw and filtered data for A1-type wire.

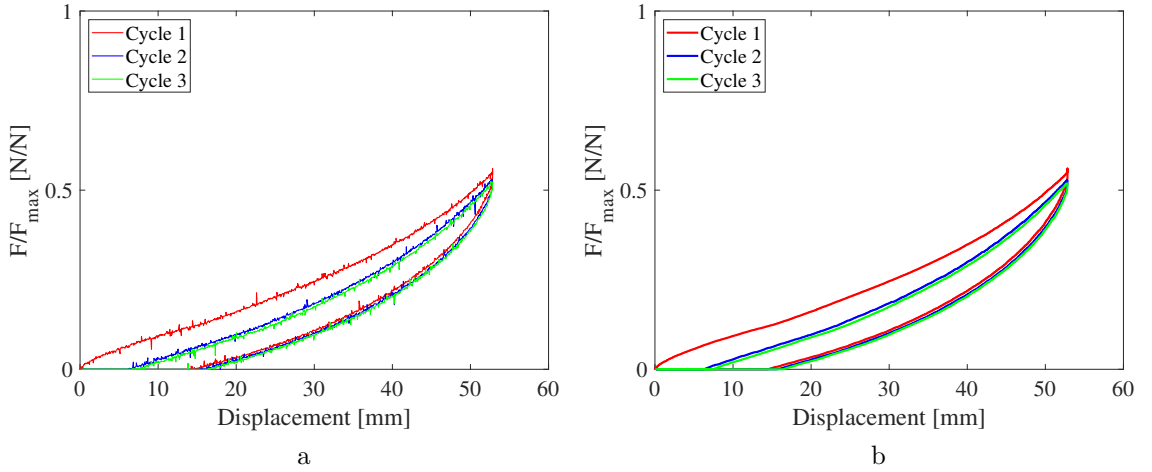


Figure 2.5: (a) Raw and (b) filtered force versus displacement data for cantilever bending test of A1-type wire.

The motion capture data is sampled at 50 frames per second. Figure 2.6 shows the motion capture data for an A1-type wire sample. The data is shown at five intervals each interval corresponding to a vertical deflection of 10 mm.

Figure 2.5 shows strain hardening between loading profiles of (cycle 2, cycle 3) and cycle 1. This implies that the sample has undergone plastic deformation. The

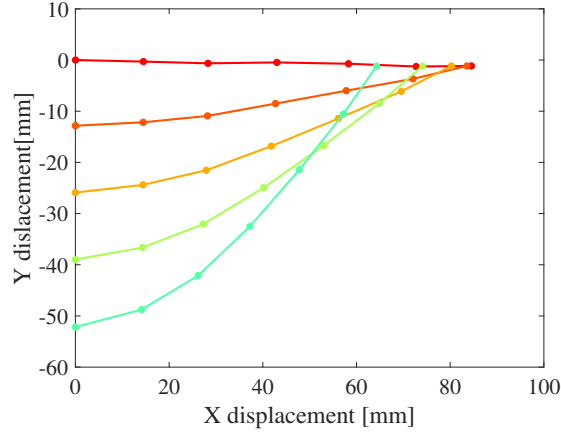


Figure 2.6: Motion capture of an A1-type wire under cantilever bending.

loading profile of the first cycle is used to characterize the electrical wires. For comparison with the analytical model in Chapter 3, a 95% confidence interval is estimated based on the experimental data as shown in Figure 2.7. The confidence limits at any displacement  $[\delta]$  for unknown population standard deviation are given by

$$F_{limits,\delta} = \bar{x}_\delta \pm t_{0.95,n} \frac{s}{\sqrt{n}}, \quad (2.1)$$

where  $\bar{x}_\delta$  is the mean force of all samples at displacement  $\delta$ ,  $n$  is the number of samples,  $t_{0.95,n}$  is the t-statistic for  $n$  samples, and  $s$  is the standard deviation.

A1 and A2-type wires were tested in two different lengths. The data is used to prove the independence of length of the analytical model output presented in Chapter 3.

For a cantilever beam with fixed deflection, the force at the free end is inversely proportional to the beam length. This can be observed in Figure 2.9 and Figure 2.10, where the longer beams are experiencing less force than shorter beams.

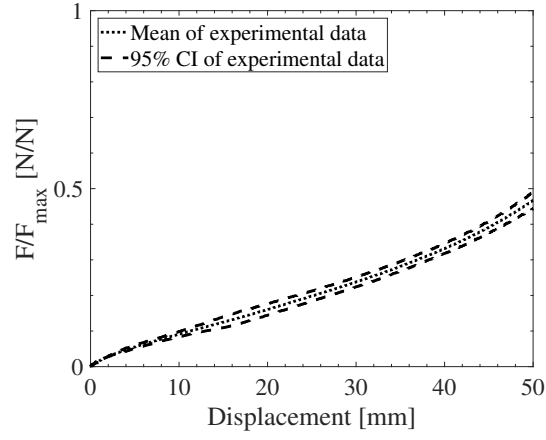


Figure 2.7: Force versus displacement data for cantilever bend test of A1-type wire samples showing the mean and the 95% confidence interval.

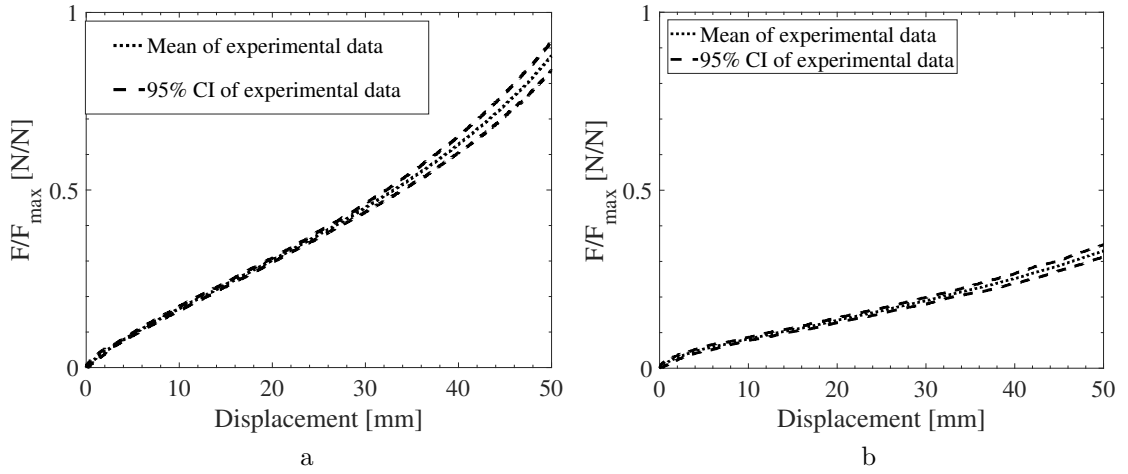


Figure 2.8: Force versus displacement data for cantilever bending tests of (a) A2-type and (b) A3-type wires.

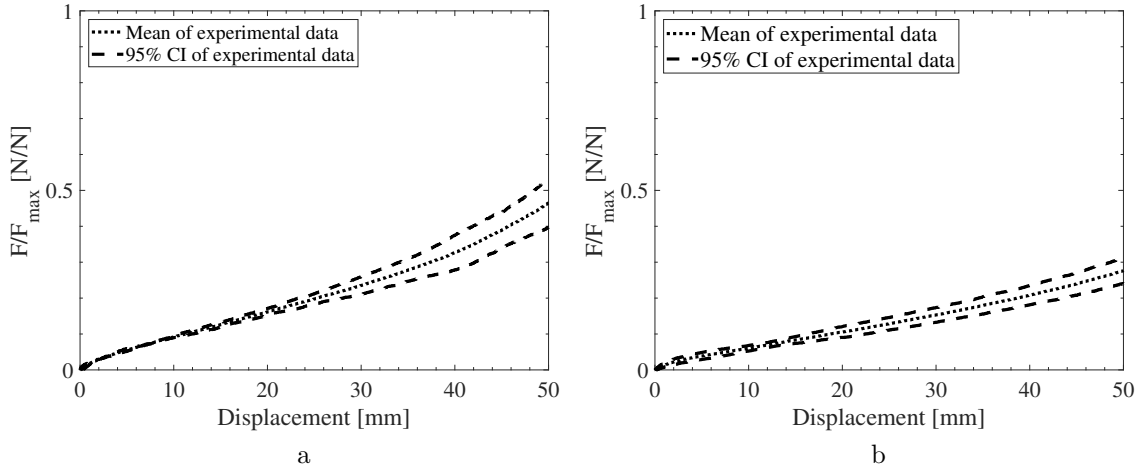


Figure 2.9: Force versus displacement data for cantilever bending test of (a) 85 mm and (b) 100 mm long B1-type wire samples.

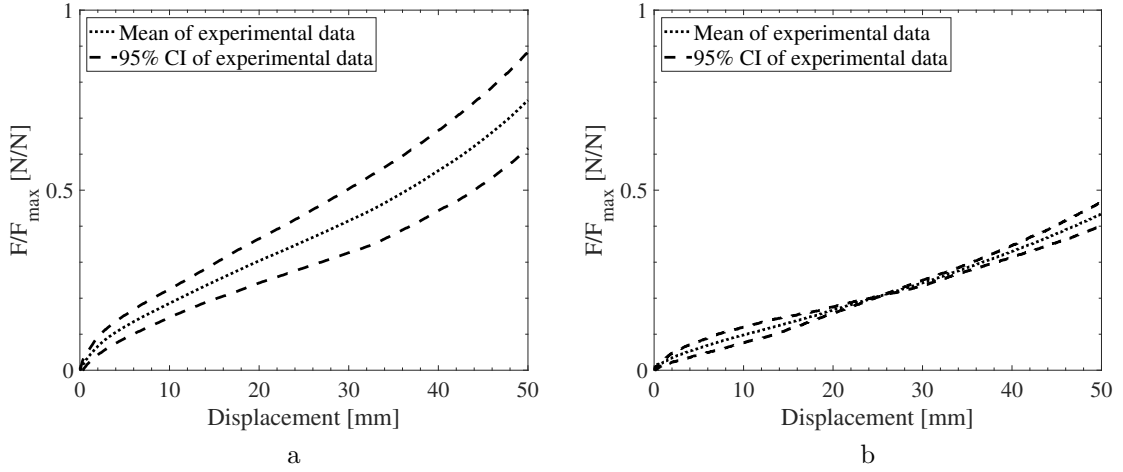


Figure 2.10: Force versus displacement data for cantilever bending test of (a) 85 mm and (b) 100 mm long B2-type wire samples.

## 2.2 Protective conduits

Electrical wires are enclosed in a protective conduit as shown in Figure 2.11. As part of this dissertation two types of protective conduits are studied - corrugated

tubes and twist tubes. Corrugated tubes are made by extrusion blow molding of molten polypropylene. These tubes can either be slit or unslit. Slit tubes are cut along the length of the tube. Twist tube is a self-wrapping sleeve made with woven polypropylene fabric. Twist tubes are used in applications where the harness experiences high frequency loads as the fabric helps in damping the vibrations. The dimensions of the conduits tested are shown in Table 2.2

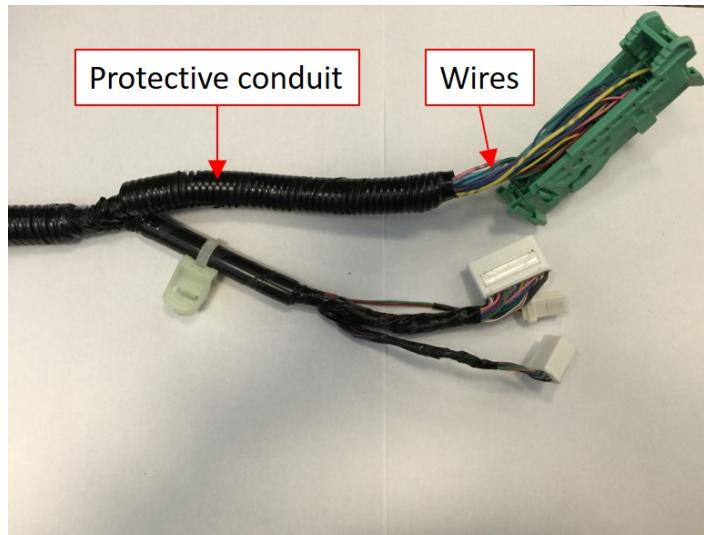


Figure 2.11: Typical automotive wire harness.

### 2.2.1 Corrugated tube test setup

The detailed experimental setup is shown in Figure 2.12. Corrugated tube test samples are prepared by cutting pieces off the spool and casting the ends of the tubes in epoxy. A custom silicon mold as shown in Figure 2.13 is used to cast the ends of the corrugated tube in epoxy as shown in Figure 2.13. The sample length was chosen as 140 mm (5.5 in) so that the gauge length is 114.3 mm (4.5 in) and the epoxied ends are

12.7 mm (0.5 in) long on either side. The samples are mounted in a TestResources<sup>©</sup> load frame by clamping the epoxy casts with MTS Advantage<sup>®</sup> screw action grips. The sample is extended by 50 mm at a rate of  $0.423 \text{ mm s}^{-1}$  (1 in/min). The sample is tested until break as soft polypropylene is highly stretchable. The displacement is measured using an built-in LVDT sensor and the force is measured using a Test Resources 500 lbf load cell. R-controller software is used to set the test parameters and to record the force and the displacement as measured by the sensors. The initial and final stages of the corrugated tube test are shown in Figure 2.12

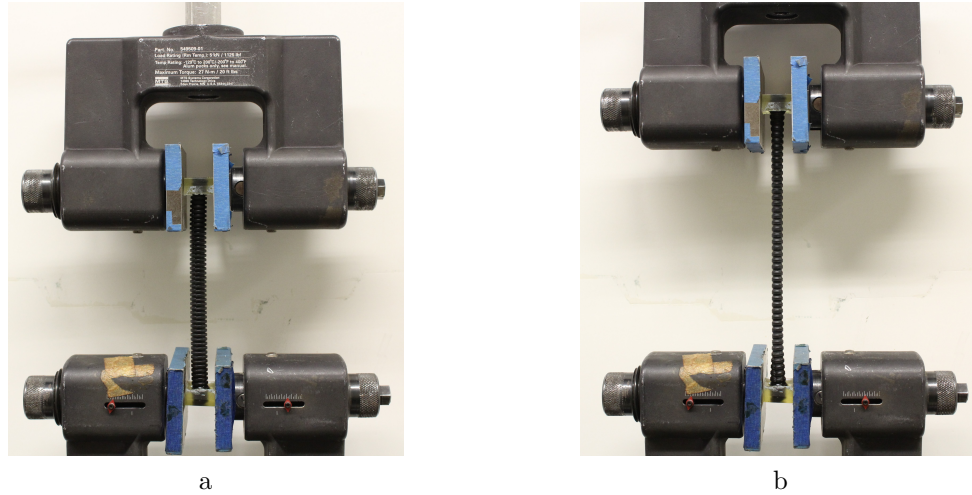


Figure 2.12: (a) Initial and (b) final stage of 10 mm diameter corrugated tube tensile test.

Table 2.2: Inner diameter, outer diameter, and wall thickness of the three types of corrugated tubes tested.

Type	<i>I.D.</i> (mm)	<i>O.D.</i>	<i>t</i> (mm)
Unslit	7.4	10.2	0.27
Unslit	10.7	14.1	0.27
Slit	10.7	14.1	0.27

Table 2.2 shows the three types of corrugated tubes tested and their dimensions. The procedure of the test is:

1. Cut a (5.5 in) long sample from a corrugated tube spool
2. Stand the sample on one end in the silicon mold and pour epoxy such that 12.7 mm (0.5 in) of the sample is submerged and let it cure for 12 hours
3. Repeat step 2 for the other end
4. Mount the epoxy casts in the load frame grippers as shown in Figure 2.12
5. Set the displacement and the loading rate in the R-controller software and start the test
6. Record the force and displacement as measured by the sensors

## 2.2.2 Corrugated tube results

Three samples of each tube type are tested and the force versus displacement plots are presented in this section. The normalized force versus displacement plot shows a linear profile up to 10 mm extension (8.7%). The corrugated tube is characterized by fitting a straight line to the initial linear region.

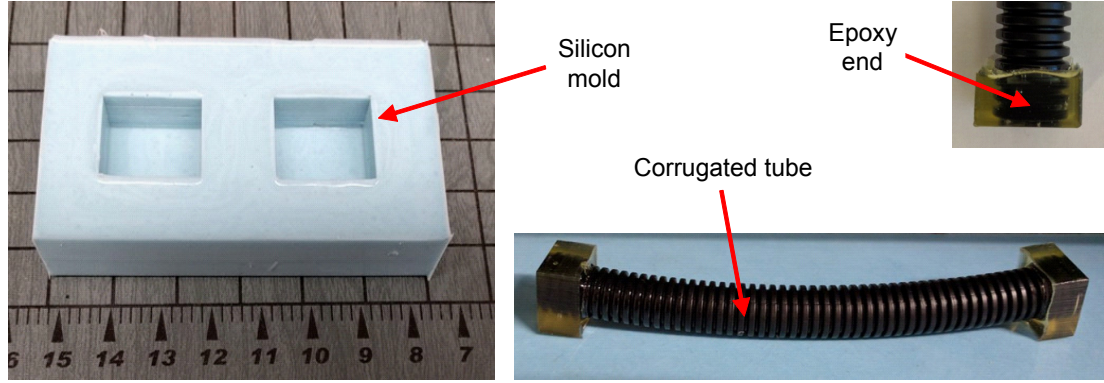


Figure 2.13: Preparation of corrugated tube tensile test samples.

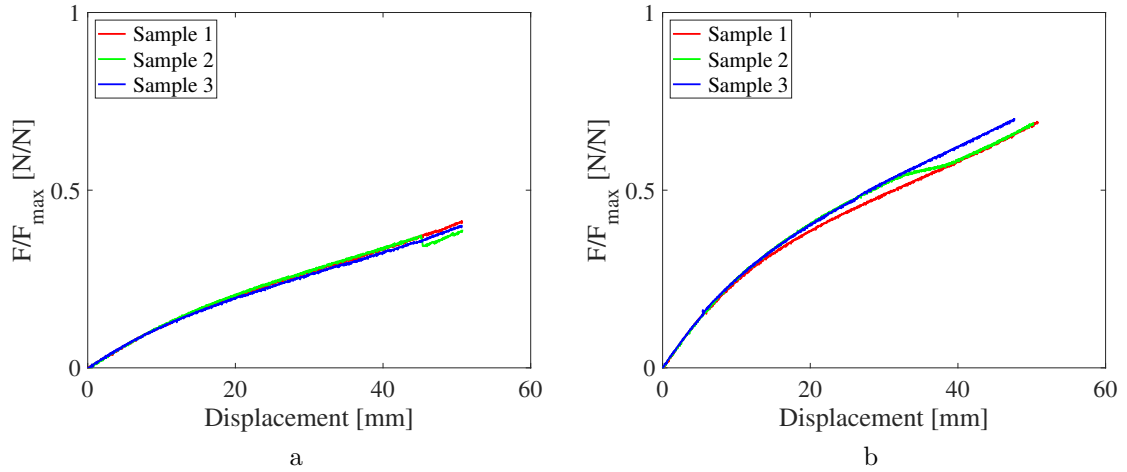


Figure 2.14: Force versus displacement data for tensile testing of (a) slit and (b) unslit corrugated tube with 10 mm inner diameter.

Due to the cylindrical profile of the tube, circumferential stress affects the force response of the corrugated tube. This can be observed in Figure 2.14, where the slit tube has a lower force-displacement response compared to the unslit tube. The slit allows the tube to warp about its length. The circumferential stress increases with a

decrease in the tube diameter. Hence, the force response of a 10 mm diameter tube is lower than that of a 7 mm diameter tube as shown in Figure 2.14b and Figure 2.15.

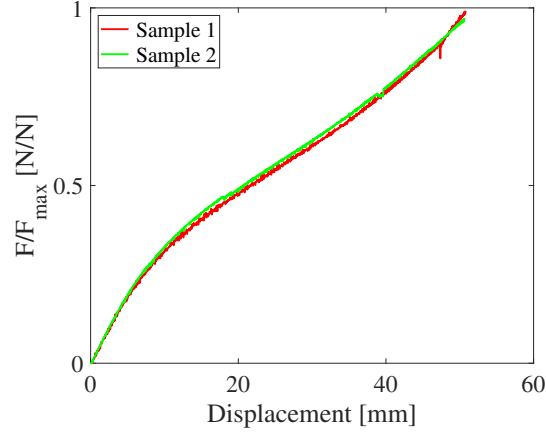


Figure 2.15: Force versus displacement data for tensile testing of 7 mm diameter unslit corrugated tube.

The corrugated tube is modeled as a hollow cylinder with a longitudinal modulus equivalent to the value calculated from the force displacement plots. The vertical shift in the force response observed in Figure Figure 2.14a is due to the sample slipping in the grips. A confidence region was not calculated as the test results show very little variance qualitatively.

### 2.2.3 Twist tube setup

The twist tube has an architecture similar to that of a textile fabric. Hence, the test setup was designed based on ASTM D5034-09, the standard for characterizing the tensile strength of textile fabrics. A schematic of the twist tube tensile test setup is shown in Figure 2.16. The samples were tested using an MTS CriterionC43.504 load frame and a LPS.155 low profile shear beam load cell with a force rating of 50 kN. The sample is mounted using MTS Advantage<sup>®</sup> screw action grips with serrated faces and manual screw clamps. The test specimen is 200 mm long and 25 mm wide, and the gauge length is 75 mm. The loading rate of the specimen is 5 mm/s. Sample failure triggers the machine to stop loading. The load frame is an electro-mechanical machine and the cross-head is driven by a servo motor. The displacement is calculated by multiplying the motor angular speed and the driving gear diameter.

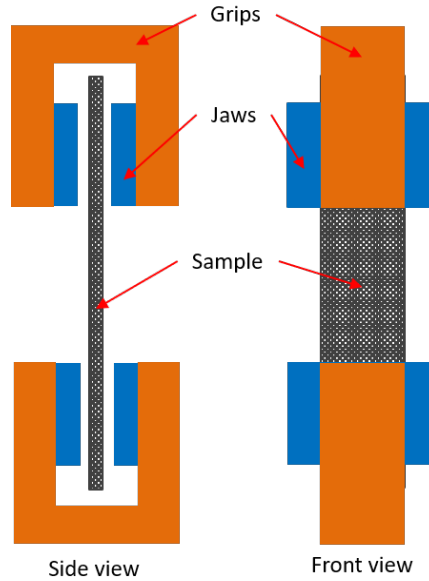


Figure 2.16: Twist tube test setup schematic showing the sample and the setup.

The procedure of the test is:

1. Cut a 200 mm (7.87 in) long sample from a twist tube spool
2. Unwrap the sample and mount it on the load frame in the manual screw clamps
3. Set the displacement and the loading rate in the MTS test suite software and start the test
4. Set the test to stop at breakage, i.e., once the sample tear is detected
5. Record the force and displacement as measured by the sensors

The initial and final shape of the sample are shown in Figure 2.17.

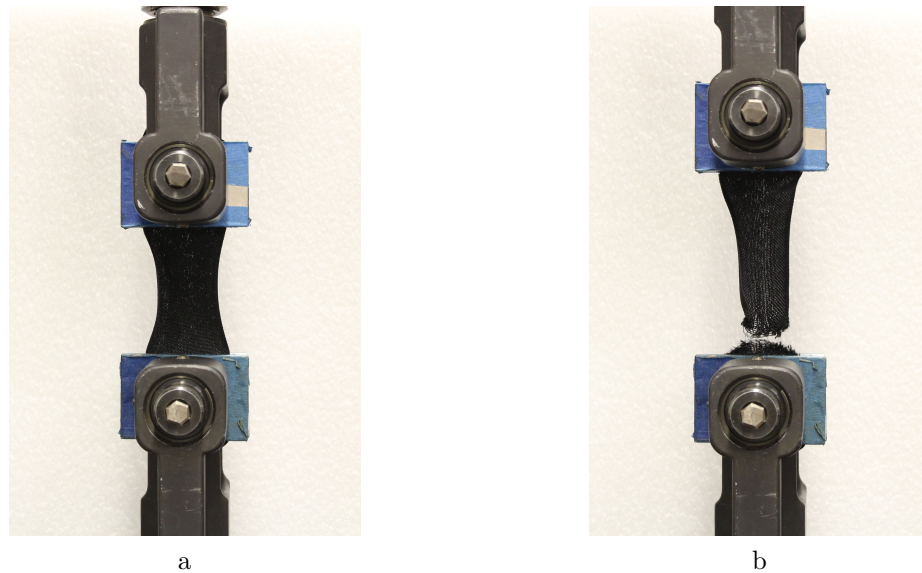


Figure 2.17: (a) Initial and (b) final state of 10 mm diameter twist tube tensile test.

### 2.2.4 Twist tube results

Six twist tube samples were tested from 2 different spools were tested. All samples are shown in Figure 2.18. The break point is closer to the jaws for all six samples. This might be due to a higher force at the region closer to the jaws as the twist tube is initially warped but is stretched open while mounting in the jaws.

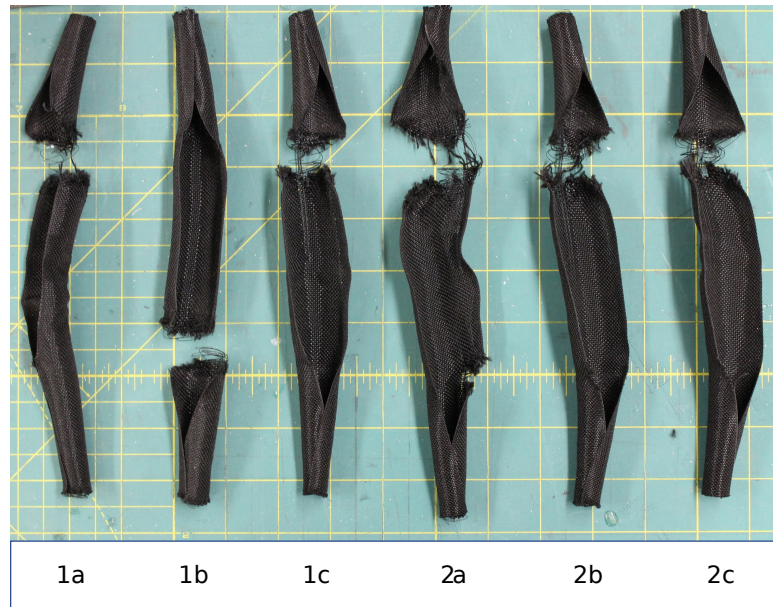


Figure 2.18: The six samples of the twist tube tested.

The normalized force versus displacement data of all the six samples is shown in Figure 2.19. The plot shows a clear bi-linear profile. A first linear region up to 10 mm extension and a second linear region beyond 10 mm are observed.

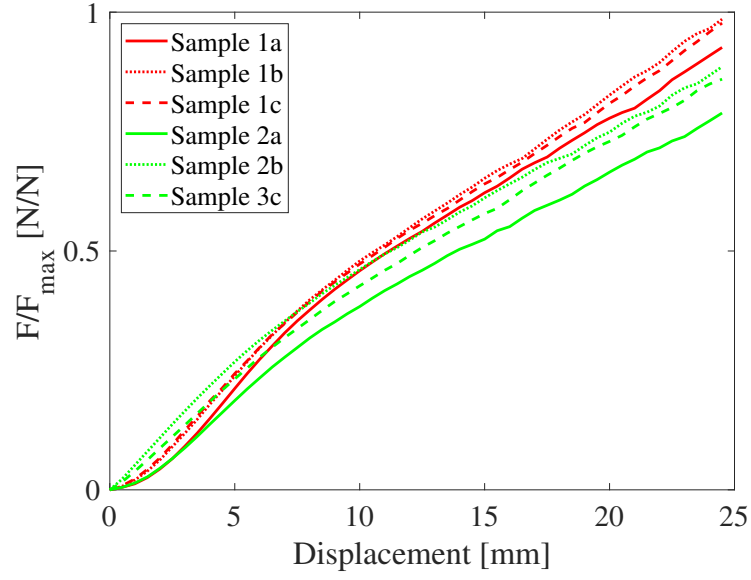


Figure 2.19: Normalized force versus displacement plot of the twist tube tensile test showing the six samples tested.

To characterize the twist tube, two straight lines are fit to the force versus displacement plot as shown in Figure 2.20. The normalized stiffness values are tabulated in Table 2.3.

Table 2.3: Normalized linear stiffness of the twist tube.

Sample	1st linear region (1/m)	2nd linear region (1/m)
1a	58.33	31.78
1b	57.71	33.98
1c	56.28	32.98
2a	47.09	27.38
2b	48.19	28.81
2c	46.08	30.50

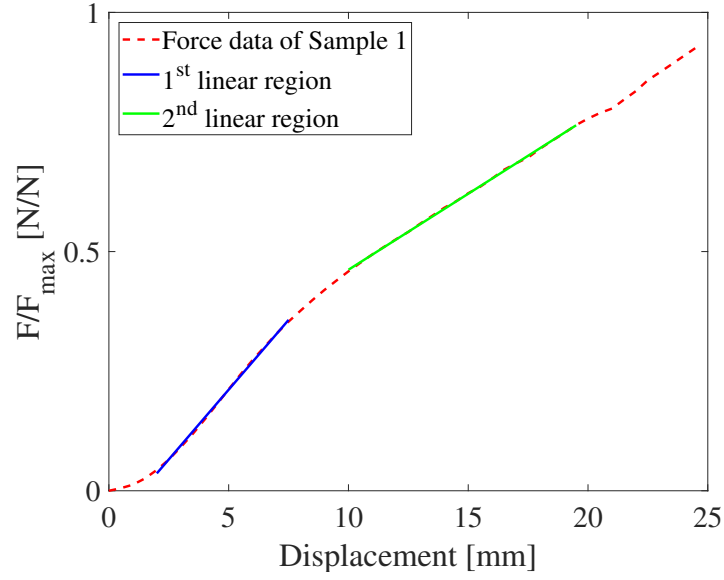


Figure 2.20: Characterizing the twist tube tensile stiffness from the normalized force versus displacement plot.

## 2.3 Insulation tape

As part of this thesis two different types of tape were used: Polyvinyl chloride (PVC) tape and Polyethylene (PET) tape. The characterization of PVC tape has been covered by Zhou [47] as part of her Masters thesis. In this section, the method to characterize the PET tape is presented. The structure of PET tape is similar to a non-woven fabric and is used in applications where the harness vibrations need to be attenuated.



Figure 2.21: Polyethylene (PET) tape sample.

### 2.3.1 Test setup

Figure 2.21 shows a Tesa<sup>®</sup> PET tape sample and Figure 2.22 shows the experiment setup. The setup is designed based on ASTM D7744 [2] for tensile testing of high performance polyethylene tapes. Crosshead travel rate has to be between 50% to 100% of the nominal gauge length of the specimen [2]. The sample gauge length is 300 mm (11.81 in), the sample width is 18.79 mm, and the sample thickness is 0.28 mm . The loading rate is 0.5 mm/sec which leads to a strain rate of 0.1 mm/mm/min. The samples were stretched until full breakage. The MTS load frame and the Advantage screw action grips described in section 2.2 are used in the tape tensile testing.

### 2.3.2 Results

For the tensile testing, five samples were tested from two different spools. Sample 2 failed at 40 mm elongation, but the other four samples failed around 60 mm elongation. The load versus elongation curves of the 5 samples are shown in Figure 2.23. The load profile shows that the samples have a low variance and the load profile suggests a bi-linear elasto-plastic behavior. The first linear region is chosen as the elastic region and the tape stiffness is calculated by fitting a straight line to the curve.



Figure 2.22: Polyethylene (PET) tape tensile test setup showing the load frame and the mounting grips.

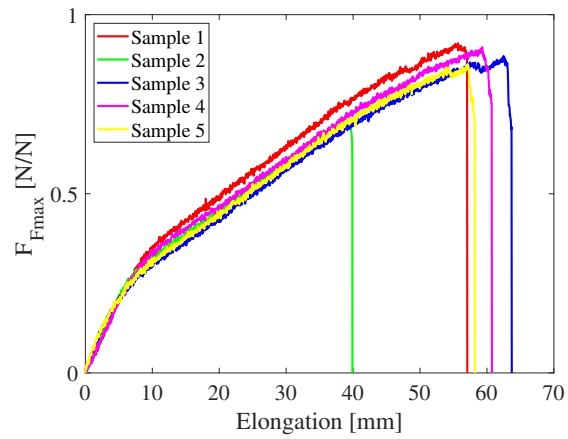


Figure 2.23: Normalized load versus displacement plots for tensile testing of polyethylene (PET) tape.

## Chapter 3: Wire Analytical Model

### Overview

*In this chapter an analytical model is presented to mathematically determine the homogenized bending modulus of an electrical wire. In Chapter 2 a methodology was presented to characterize the bending behavior of electrical wire. However, due to a large number of wires being used in applications, it is time consuming to test and characterize each wire. It is noted that an electrical wire is made by helical winding of copper conductors within a polymer insulation. This helical structure makes it possible to analytically simulate the cantilever bending test presented in Chapter 2. The goal of this analytical model is to simulate the cantilever bending test and output an effective bending modulus, which can be used in digital manufacturing software.*

### 3.1 Wire geometry

In a wire, the positions of the conductors in the cross section affect the bending stiffness of the wire. Hence, in order to automate the process of defining conductor layouts for a large number of wire types and sizes in digital manufacturing applications, an algorithm is written for packing smaller circles in a larger bounding circle. The smaller circles represent the conductors and the larger circle represents the inner surface of the insulation. Initial values for the center coordinates of each conductor are guessed using a random number generator. The conductor layout is estimated by minimizing the elastic energy of the system, defined as the sum of distances squared.

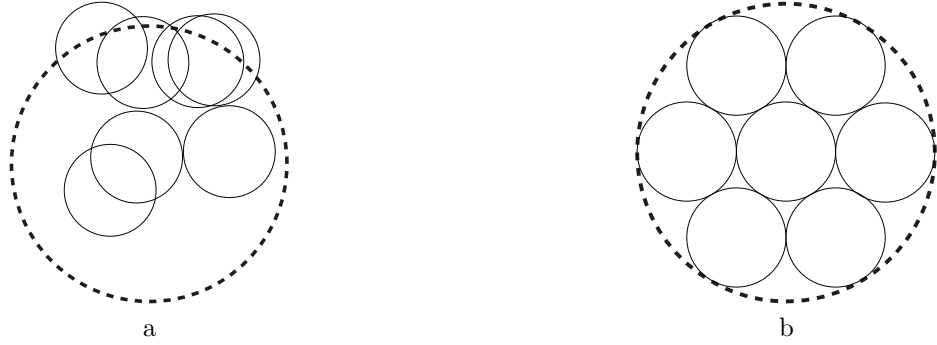


Figure 3.1: (a) Initial guess for conductor configuration; (b) optimized conductor configuration obtained using a circle packing algorithm. The dashed circle represents the inner surface of the insulation and the solid circles represent the outlines of the individual conductors.

Assume  $N$  smaller circles with equal radii  $r$  are to be packed in a larger bounding circle of radius  $R$ . The minimum distance between an  $i^{\text{th}}$  circle with center  $(x_i, y_i; i = 1, 2, 3, \dots, N)$  and a  $j^{\text{th}}$  circle with center  $(x_j, y_j; j = 1, 2, 3, \dots, N)$  is given by

$$d_{i,j} = \begin{cases} 2r - \sqrt{(x_i - x_j)^2 + (y_i - y_j)^2} & \text{if } \sqrt{(x_i - x_j)^2 + (y_i - y_j)^2} < 2r \\ 0 & \text{otherwise.} \end{cases} \quad (3.1)$$

The minimum distance between the  $i^{\text{th}}$  circle and the bounding circle with center at origin  $(0, 0)$  is given by

$$d_{i0} = \begin{cases} r - R + \sqrt{x_i^2 + y_i^2} & \text{if } \sqrt{x_i^2 + y_i^2} + r > R \\ 0 & \text{otherwise.} \end{cases} \quad (3.2)$$

Assuming a unit proportionality constant, the potential energy of the  $i^{\text{th}}$  body is given by

$$U_i = d_{i0}^2 + \sum_{j=1, j \neq i}^N d_{ij}^2, \quad (3.3)$$

and the total potential energy  $U$  of the system is given by

$$U = \sum_{i=1}^N U_i. \quad (3.4)$$

Conductor centerline coordinates are solved by multi-variable optimization of  $U(x_1, y_1, x_2, y_2, \dots, x_N, y_N)$  using the MATLAB<sup>®</sup> function *fminunc*. This function uses a quasi-Newton search method to find the function minimum; the search direction is determined by estimating the approximate Hessian matrix using the Broyden—Fletcher—Goldfarb—Shanno (BFGS) formula. Initial values of the center locations are randomly chosen such that conductor centers are within the insulation as shown in Figure 3.1a. The final conductor arrangement after packing is shown in Figure 3.1b. Comparisons between the estimated conductor arrangements and actual wire cross sections for 7-conductor and 19-conductor wires are shown in Figure 3.2.



Figure 3.2: Estimated and actual cross sections of a typical (a) 7-conductor wire and (b) 19-conductor wire.

The wire conductors are sorted into groups based on the radial distances of the conductor centerlines to the wire centerline. Here, the number of groups equals the number of layers in the helix. For simplicity, a  $p^{\text{th}}$  conductor in a  $q^{\text{th}}$  layer is identified as  $(p, q)$ . The values taken by  $(p, q)$  are

$$(p, q) = \begin{pmatrix} 1, 1 & 1, 2 & \dots & 1, Q \\ 2, 1 & 2, 2 & \dots & \vdots \\ \vdots & \vdots & \ddots & \vdots \\ N_1, 1 & \vdots & \ddots & \vdots \\ & N_2, 2 & \ddots & \vdots \\ & & \ddots & \vdots \\ & & & N_Q, Q \end{pmatrix}, \quad (3.5)$$

with the columns representing the helix layers and the rows representing the conductors in a layer. For example, the 7-conductor wire shown in Figure 3.2a has one core and one layer with 6 conductors, so  $Q = 1$  and  $N_1 = 6$ . Similarly, for the 19-conductor wire shown in Figure 3.2b,  $Q = 2$ ,  $N_1 = 6$ , and  $N_2 = 12$ . In Figure 3.2b there is a slight mismatch between the calculated and actual positions of the conductors in

the second layer. Hence, the analytical model was applied both to the algorithm-generated and true configurations and it was observed that the difference between the model outputs was not significant. For modeling, the wire layout is oriented by defining the neutral axis by a vector connecting the wire centerline and the centerline for a randomly chosen conductor in the first layer. For the wires tested in this work (lay angle  $< 15^\circ$ ), no distortion in the conductor cross sections was observed in either FEA or optical measurements. However, for wires with larger lay angles, it is understood that the lay angle can have an effect on the cross sectional shape of the conductors. To account for this change in cross sectional shape, the algorithm can be modified to pack ellipses within a circle [22]. The algorithm above is restricted to conductors with equal diameters, but can be readily modified to model wires having layers composed of conductors with different diameters [44].

## 3.2 Stick-slip model

The wire conductor is made of helically-wound metal conductors. Due to its stranded nature, a wire in bending exhibits two kinematic states: stick state and slip state. Initially, the wire is in a stick state and bends as a single beam. With increasing curvature, the axial forces induced in the conductors due to bending exceed the frictional force and the conductors start to slip against adjacent surfaces, causing the wire to be in the slip state.

### 3.2.1 Stick state

Conductors in the stick state are modeled as Euler-Bernoulli beams and the axial strain in a conductor is the sum of responses from torsion, elongation, and bending of the wire. The axial strain in the  $p^{\text{th}}$  conductor in the  $q^{\text{th}}$  layer is given as

$$\epsilon_{p,q} = \kappa_w r_q \sin \theta_{p,q} \cos^2 \alpha_q + \epsilon_w \cos^2 \alpha_q + \tau_w r_q \sin \alpha_q \cos \alpha_q, \quad (3.6)$$

where  $\kappa_w$ ,  $\epsilon_w$ , and  $\tau_w$  respectively denote curvature, elongation, and twist in a wire,  $r_q$  is distance from the wire center to the  $q^{th}$  layer,  $\theta_{p,q}$  is the angular position of the conductor from the x-axis, and  $\alpha_q$  is the lay angle of the  $q^{th}$  layer. Multiplying (3.6) with conductor axial rigidity  $(EA)_s$  gives the axial force as

$$T_{p,q} = (EA)_s \left( \kappa_w r_q \sin \theta_{p,q} \cos^2 \alpha_q + \epsilon_w \cos^2 \alpha_q + \tau_w r_q \sin \alpha_q \cos \alpha_q \right). \quad (3.7)$$

The wires are assumed to be under pure bending. Hence, the wire elongation and twist are neglected and the conductor axial force  $T_{p,q}$  in (3.7) is directly proportional to  $r_q$ , the radial distance of the conductor centerline from the wire centerline. Therefore, slip begins in the conductors farthest from the neutral plane and progresses towards the center.

### 3.2.2 Slip state

In the slip state, the Amontons-Coulomb friction model is used to define the contact forces between conductors and between the conductors and the insulation. Helically-wound wires have a small tangential gap between conductors in the same layer [19] due to imperfections from manufacturing or the loading process. Hence, only the contact forces between conductors of adjacent layers are modeled and contact forces between conductors in the same helix layer are neglected. A differential conductor element in the  $q^{th}$  layer is selected as shown in Figure 3.3. The static equilibrium equation is given by

$$dF_{p,q} - g_{p,q} - h_{p,q} = 0, \quad (3.8)$$

$$dF_{p,q} - \mu_q H_{p,q} - \mu_{q-1} G_{p,q} = 0, \quad (3.9)$$

where  $\mu_q$  and  $H_{p,q}$  are the friction coefficient and the normal force, respectively, between layer  $q$  and layer  $q + 1$ . Similarly,  $\mu_{q-1}$  and  $G_{p,q}$  are the friction coefficient and the normal force, respectively, between layer  $q - 1$  and layer  $q$ .

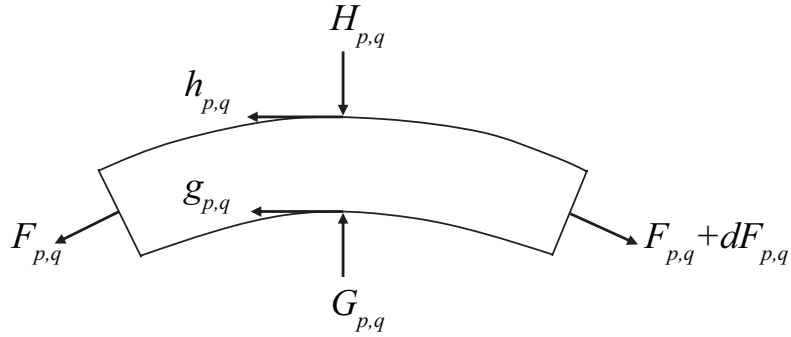


Figure 3.3: Static force diagram for a differential element of the  $p^{th}$  conductor in the  $q^{th}$  layer subjected to an axial force  $F_{p,q}$ , normal forces  $H_{p,q}$  and  $G_{p,q}$  from adjacent layers, friction forces  $h_{p,q}$  and  $g_{p,q}$  resulting from relative sliding of adjacent layers, and the resulting increment in axial force  $dF_{p,q}$ .

The radial force exerted by the insulation  $F_{ins}$  is constant throughout the wire cross section. To satisfy equilibrium between layers, the force exerted by layer  $q$  on layer  $q - 1$  layer is given by

$$H_{p,q-1} = G_{p,q} \frac{N_q}{N_{q-1}}. \quad (3.10)$$

Substituting (3.10) in (3.9) and satisfying static equilibrium, the normal forces exerted on the  $q^{th}$  layer by the surrounding layers are given by

$$H_{p,q} = \sum_{k=q+1}^Q \left( F_{p,k} \sin \alpha_k \frac{N_k}{N_q} \right) + F_{ins} \frac{N_Q}{N_q}, \quad (3.11)$$

$$G_{p,q} = H_{p,q} + F_{p,q} \sin \alpha_q. \quad (3.12)$$

Substituting (3.11) and (3.12) in (3.9) one obtains the differential increment in axial force  $dF_{p,q}$  as

$$dF_{p,q} = (\mu_q + \mu_{q-1}) \left( \sum_{k=q+1}^Q F_{p,k} \sin \alpha_k \frac{N_k}{N_q} + F_{ins} \frac{N_Q}{N_q} \right) d\theta + \mu_{q-1} F_{p,q} \sin \alpha_q d\theta. \quad (3.13)$$

Solving (3.13) with initial condition  $F_{p,q}(0)$ , the frictional force  $F_{p,q}$  in the  $p^{th}$  conductor located in the  $q^{th}$  layer is given by

$$F_{p,q} = \exp(\mu_{q-1} \sin \alpha_q \theta_{p,q}) \left( F_{p,q}(0) + \frac{\mu_q + \mu_{q-1}}{\mu_{q-1} \sin \alpha_q} B_{p,q} \right) - \frac{\mu_q + \mu_{q-1}}{\mu_{q-1} \sin \alpha_q} B_{p,q}, \quad (3.14)$$

$$B_{p,q} = \sum_{k=q+1}^Q \left( F_{p,k} \sin \alpha_k \frac{N_k}{N_q} \right) + F_{ins} \frac{N_Q}{N_q}. \quad (3.15)$$

In the solution procedure, for each increment in curvature  $\kappa$ ,  $T_{p,q}$  and  $F_{p,q}$  are compared to determine if the conductor is in the stick or slip state and the minimum of  $(T_{p,q}, F_{p,q})$  is taken as the conductor axial force. Mathematically, the axial force is represented as

$$F_{p,q} = \begin{cases} T_{p,q} & \text{if } T_{p,q} < F_{p,q} \text{ (stick state)} \\ F_{p,q} & \text{otherwise (slip state).} \end{cases} \quad (3.16)$$

Under elastic bending, the total bending moment induced in an electrical wire is the sum of moments in the conductors, moments in the insulation, and the moments

induced by the conductor's axial forces. At a curvature  $\kappa$ , the total bending moment induced in a wire is given by

$$M = \sum_{q=1}^Q \sum_{p=1}^{N_q} EI_{p,q} \kappa + EI_{ins} \kappa + \sum_{q=1}^Q \sum_{p=1}^{N_q} F_{p,q} r_q \sin \theta_{p,q}. \quad (3.17)$$

Here,  $EI_{p,q}$  is the bending stiffness of the  $p^{th}$  strand in the  $q^{th}$  layer,  $EI_{ins}$  is the bending stiffness of the insulation,  $F_{p,q}$  is the conductor axial force, and  $r_q \sin \theta_{p,q}$  is the distance from the conductor center to the wire's neutral axis. In (3.17),  $EI_{p,q}$  is given [11] by

$$EI_{p,q} = \frac{\cos(\alpha_q)}{2} EI_s \left( 1 + \cos^2 \alpha_q + \frac{\sin \alpha_q}{1 + \nu_s} \right), \quad (3.18)$$

where  $EI_s$  is the bending stiffness of the conductor assumed as a straight cylindrical beam, and  $\nu_s$  is the Poisson's ratio of the conductor.

### 3.2.3 Plastic state

During large deflection bending of a wire, the conductors undergo plastic deformation. The plastic zone begins when the maximum stress along the beam's cross section exceeds the material's yield stress. The plastic zone spreads towards the neutral axis with increasing curvature. Figure 3.4b shows the stress distribution in elastic and elasto-plastic regions.

A beam having only elastic stress distribution obeys Hooke's Law. However, in elasto-plastic stress distribution, the strain in the plastic region is not linearly related to the stress [38]. Therefore, the beam is assumed to have a laminated structure, with each lamina having different material properties. For a lamina with thickness  $dy$ , width  $b(y)$ , and located at a distance  $y$  from the neutral axis, the bending stiffness

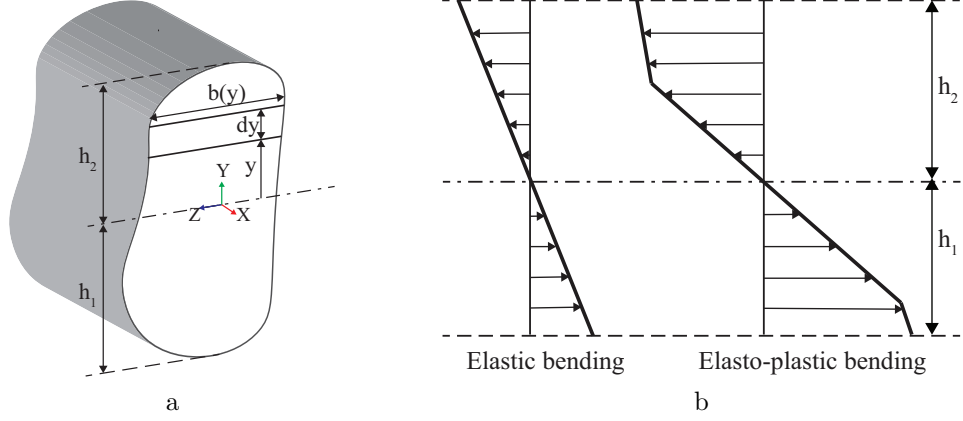


Figure 3.4: (a) Cross section of a generic beam showing a layer of differential thickness  $dy$ ; (b) stress distribution across a beam's cross section for elastic and elasto-plastic bending, showing stress reduction due to plasticity.

is given by

$$d(EI_s) = E(y) b(y) y^2 dy, \quad (3.19)$$

and integrating (3.19) across the beam's cross section, the bending stiffness of the beam is given by

$$EI_s = \int_{-h_1}^{h_2} E(y) b(y) y^2 dy. \quad (3.20)$$

Here, the elastic modulus  $E(y)$  is the secant modulus calculated from the material stress-strain curve at a local strain  $\epsilon_{xx} = y\kappa$ . The conductors are typically made with ductile metals, hence the conductor is assumed to have the same stress-strain relationship in compression and in tension. For a cylindrical conductor with radius  $r$ , the bending stiffness given by (3.20) reduces to

$$EI_s = 2 \int_{-r}^r E(y) \left( \sqrt{r^2 - y^2} \right) y^2 dy, \quad (3.21)$$

and discretizing the integral, we have

$$EI_s = 2 \sum_{v=1}^V E_v \left( \sqrt{r^2 - y_v^2} \right) y_v^2 \Delta y. \quad (3.22)$$

Here,  $V$  is the total number of laminae in the conductor's cross section,  $E_v$  is the elastic modulus of the  $v^{\text{th}}$  layer,  $y_v$  is the distance of the  $v^{\text{th}}$  lamina from the neutral axis, and  $\Delta y$  is the lamina thickness ( $\Delta y \ll R$ ). The bending stiffness given by (3.22) is for a straight cylindrical beam. Substituting (3.22) in (3.18) one obtains the bending stiffness of a helical beam. The total bending moment (3.17) is differentiated with respect to  $\kappa$  to give

$$EI_w(\kappa) = \sum_{q=1}^Q \sum_{p=1}^{N_q} EI_{p,q} + EI_{ins} + \sum_{q=1}^Q \sum_{p=1}^{N_q} \frac{dF_{p,q} r_q}{d\kappa}. \quad (3.23)$$

At each value of curvature, the homogenized bending stiffness of the wire is evaluated using (3.23) and is recorded as a lookup table. The lookup table serves as a tool for use in digital manufacturing software to simulate wires as homogenized rods.

### 3.3 Large deflection formulation

In a wire subjected to small deflections, the curvature is  $\kappa \approx \frac{d^2 y}{dx^2}$  and the bending moment is  $M \approx EI_w \frac{d^2 y}{dx^2}$ . For large deflections, elementary beam theory [41] gives the bending moment as

$$M = EI_w \kappa = EI_w \frac{\frac{d^2 y}{dx^2}}{\left[ 1 + \left( \frac{dy}{dx} \right)^2 \right]^{\frac{3}{2}}}. \quad (3.24)$$

Here,  $EI_w$  is the homogenized bending stiffness of the wire. Expanding the denominator in (3.24) using binomial expansion and substituting  $M$  with  $P(l - x)$  one obtains

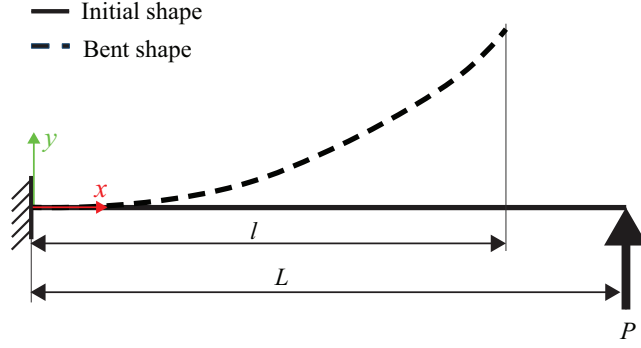


Figure 3.5: Large deflection bending of a cantilever beam subjected to a point load at its free end, showing the beam length  $L$  and the projected length  $l$ .

$$\frac{d^2 y}{dx^2} = \frac{P(l-x)}{EI_w(\kappa)} \sum_{r=0}^{\infty} \left(\frac{\frac{3}{2}}{r}\right) \left(\frac{dy}{dx}\right)^{2r}, \quad (3.25)$$

where  $P$  is the point load applied at the free end of the cantilever,  $l$  is the projection of the cantilever beam on the x-axis,  $x$  is the distance from the free end as shown in Figure 3.5, and  $EI_w(\kappa)$  is a function of curvature  $\kappa$  as shown in (3.23). Solving the nonlinear differential equation (3.25) [33] using reversion [1], the beam equation  $y(x)$  is derived as

$$y(x) = \left(\frac{P}{2EI_w(\kappa)}\right) \left(-\frac{x^3}{3} + lx^2\right) + \frac{1}{2} \left(\frac{P}{2EI_w(\kappa)}\right)^3 \left(-\frac{x^7}{7} + lx^6 - \frac{12}{5}l^2x^5 + 2l^3x^4\right) + \text{higher order terms.} \quad (3.26)$$

In the simulation procedure, the force  $P$  is increased in steps and at each increment the shape of the beam is evaluated using (3.26). The bending stiffness  $EI_w$  varies with curvature and is determined from a look-up table of  $EI_w$  versus  $\kappa$ . Curvature at the fixed end, where slip initiates, is used to determine  $EI_w$  and at each increment

in  $P$ , the bending stiffness is assumed constant along the beam curved length  $l$ . The tip displacement  $y(l)$  is recorded as a function of the tip force  $P$ .

### 3.4 Model calibration and evaluation

The radial force exerted by the insulation  $F_{ins}$ , and the interlayer friction coefficients  $(\mu_1, \mu_2, \dots, \mu_{N-1}, \mu_N)$  are identified as the model parameters. Because all the conductors are made with copper, inter-conductor friction coefficients are assumed to be equal, i.e.,  $\mu_1 = \mu_2 = \dots = \mu_{N-1} = \mu_s$ , and the friction coefficient between the insulation and the outermost layer ( $N^{th}$  layer)  $\mu_N$  is designated as  $\mu_i$ . The parameter values are evaluated by calibrating the model to minimize the error between the model output and the test data. For minimizing the error, an objective function is defined with  $\mu_s$ ,  $\mu_i$ , and  $F_{rad}$  as the function variables and is given by

$$\epsilon = \sum_{i=1}^n [F_{m,i}(\mu_s, \mu_p, F_{rad}) - F_{e,i}]^2, \quad (3.27)$$

where  $\epsilon$  is the error sum of squares ( $SSE$ ),  $n$  is the total number of observations,  $F_{e,i}$  is the force measured at displacement  $d_i$ , and  $F_{m,i}$  is the force evaluated by the model at displacement  $d_i$ . Multivariable unconstrained optimization of the objective function using the MATLAB function *fminunc* solves for  $(\mu_s, \mu_p, F_{rad})$  such that the objective function  $\epsilon$  attains a minimum. Table 3.1 summarizes the initial and optimized values of the three model parameters. Data from testing A2 is used for model calibration and the data from testing of other wires is used for model validation.

The measured and simulated forces are normalized against the maximum overall recorded force and plotted versus tip displacement, as shown in Figure 3.6a. The wire shape is compared at six discrete tip displacement intervals and the measured

Table 3.1: Initial and optimized values of analytical model parameters: radial force exerted by the insulation ( $F_{rad}$ ), inter-conductor friction coefficient ( $\mu_s$ ), and insulation-conductor friction coefficient ( $\mu_p$ ).

Parameter	$F_{rad}$ (N)	$\mu_s$	$\mu_p$
Initial value	0.2	0.2	0.2
Optimized value	0.15	0.21	0.10

and simulated wire shapes are shown in Figure 3.6b. For each displacement interval, dots represent the motion capture markers on the experimental sample, the dashed line represents a polynomial fit of the markers, and the solid line represents the shape of the beam simulated by the analytical model. The difference in initial profile between the measured sample shape and simulated beam shape is due to variability in preparing the wire sample. Figure 3.6 shows that the model output agrees well with the experimental measurement.

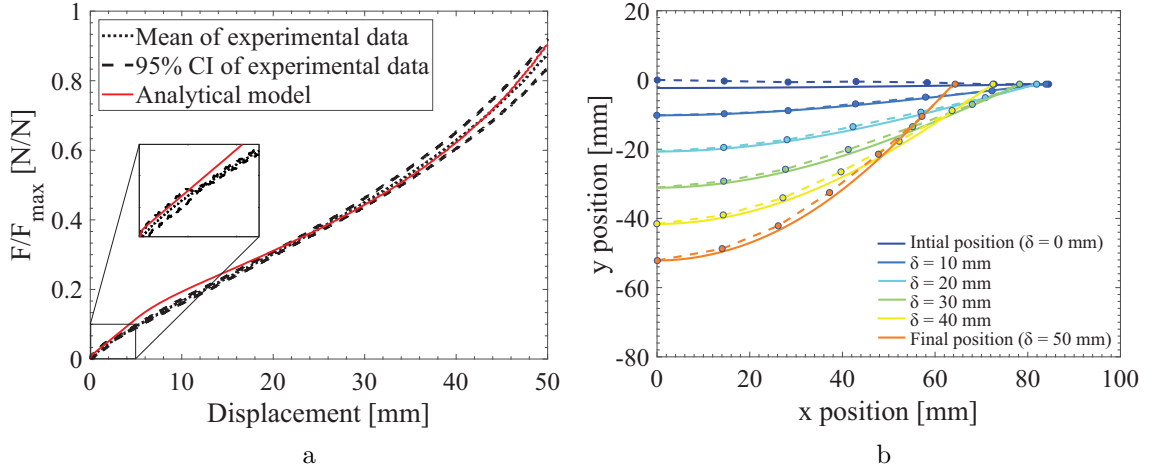


Figure 3.6: (a) Measured and simulated force versus displacement curves for cantilever bending of A2-type wire and (b) measured wire marker locations (dots), polynomial fits of marker locations (dashed lines), and the simulated wire shapes (solid lines) at various bending intervals.

The bending stiffness of A-type wires is shown as a function of curvature in Figure 3.7. As expected, the bending stiffness is highest for A3-type wire which has the largest diameter. The stick to slip transition in A3-type wire occurs over a higher range of curvature due to the higher number of conductors.

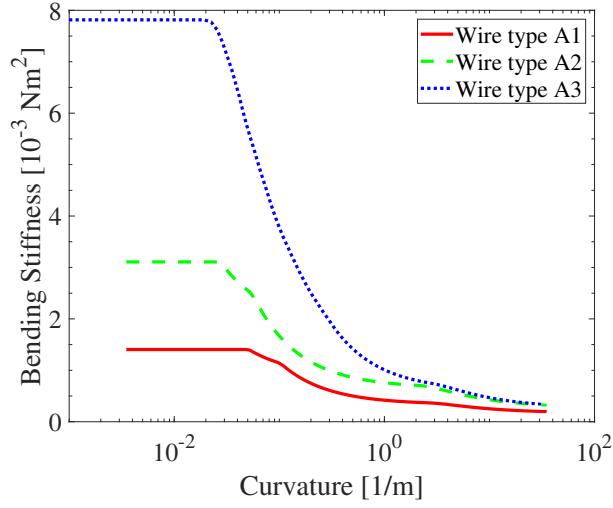


Figure 3.7: Bending stiffness versus curvature for the three A-type wires showing the difference in stick, slip, and plastic regions of the wires. A3-type wire has a more gradual transition from stick to slip state due to having two layers compared to a single layer for A1 and A2-type wires.

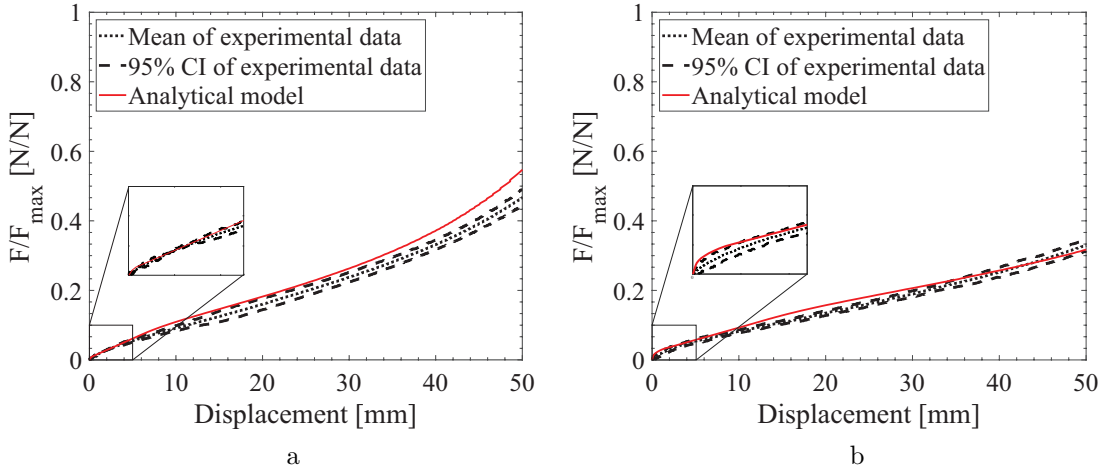


Figure 3.8: Measured and simulated force versus displacement curves for (a) A1-type wire (sample length = 85 mm) and (b) A3-type wire (sample length = 120 mm).

Figures 3.8a and 3.8b show the measured force and the simulated force versus tip displacement for A1 and A3-type wires. Samples of A1 and A2-type wires are 85 mm long, and A3-type wire samples are 120 mm long. A3-type wire samples are made longer to reduce the maximum force measured, due to the load cell capacity limit. The maximum tip displacement is 50 mm for all of the wire types. Therefore, the force observed at 50 mm displacement for A3-type wire is lower than that for A1 and A2-type wires.

As mentioned in Chapter 2, B-type wire samples were tested in two different lengths, 85 mm and 100 mm, to validate the independence of the analytical model on the sample length. Figures 3.9 and 3.10 show the measured force and the simulated force as a function of tip displacement for B1 and B2-type wires, respectively. To compare the model output, stick state bending stiffness for all the wires tabulated in Table 3.2.

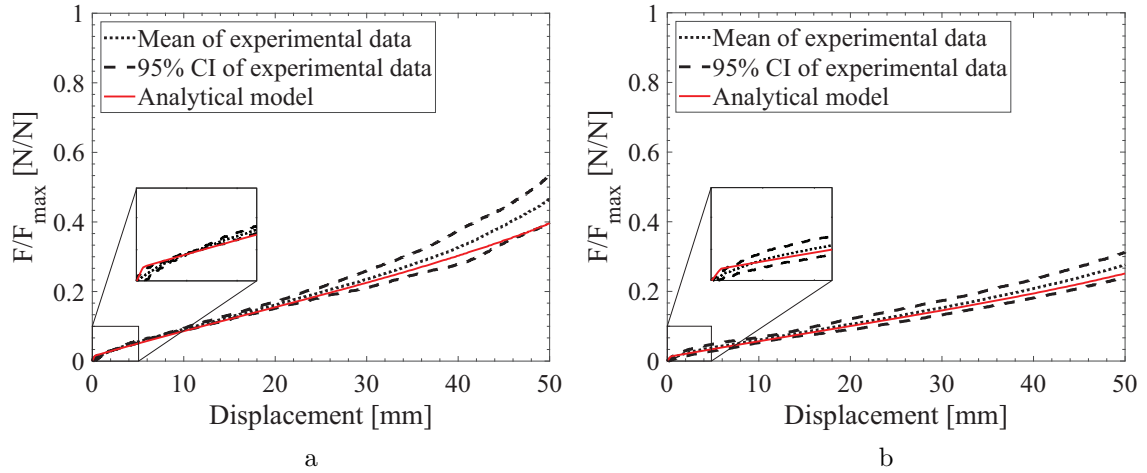


Figure 3.9: Measured and simulated force versus displacement curves for (a) 85 mm and (b) 100 mm long samples of B1-type wire.

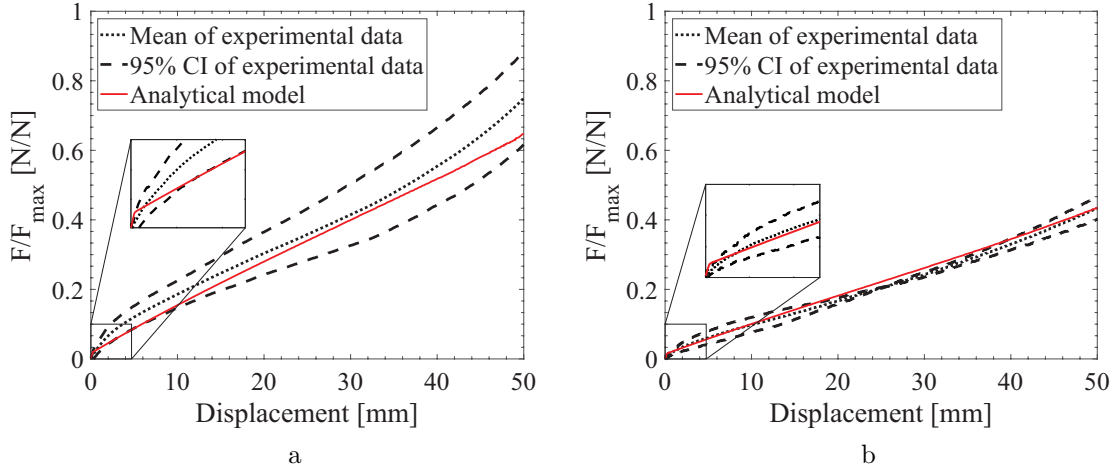


Figure 3.10: Measured and simulated force versus displacement curves for (a) 85 mm and (b) 100 mm long samples of B2-type wire.

Table 3.2: Stick-state bending stiffness of the wires as calculated by the analytical model.

Wire type	Bending stiffness [Nm <sup>2</sup> ]
A1	0.0056
A2	0.0012
A3	0.0005
B1	0.0033
B2	0.0127

Sum of squared errors ( $SSE$ ) and root of mean squares of error ( $RMSE$ ) are chosen as metrics to evaluate the model fit with respect to the experimental data. The  $SSE$  and  $RMSE$  values are calculated by

$$SSE = \sum_{i=1}^n (F_{model,i} - \bar{F}_{exp,i})^2, \quad (3.28)$$

$$RMSE = \sqrt{\frac{\sum_{i=1}^n (F_{model,i} - \bar{F}_{exp,i})^2}{n}}, \quad (3.29)$$

and are shown in Table 3.3.

Table 3.3: Sum of squared errors (SSE) and root of mean squares of error (RMSE) for the analytical model relative to experimental measurements. All of the wire types have an error  $\ll 1$ , indicating that the analytical model provides a good fit.

Wire type	<i>SSE</i>	<i>RMSE</i>
A1	0.0056	0.0059
A2	0.0012	0.0021
A3	0.0005	0.002
B1	0.0033	0.0037
B2	0.0127	0.0057

For evaluation of error metrics, the model output for each wire is compared against the experimental mean of the corresponding wire. A-type and B2-type wires have  $SSE \ll 1$  which shows that the model is a good fit. The analytical model output for B2-type wire is within the 95% confidence interval of the experimental data, but the SSE value is high because of a large variance in the test data.

### 3.5 Comparison with FEA

Due to the high computational costs associated with performing high-fidelity simulations of wire bending, only A2-type and B2-type were chosen for the FEA study in Abaqus FEA. The geometry, FE mesh, and deformed shapes of these wires are shown in Figure 3.11. The conductors are discretized using 8-node hexahedral elements, where a custom Python script was developed for meshing compressed conductors in

B2-type wires. The PVC insulation is meshed using 8-node 3D continuum shell elements, which account for the insulation thickness the same way as 3D solid elements. The conductor cross section is discretized into 10 elements and the aspect ratio of each element is less than 3. An explicit integration scheme with a mass scaling factor of 20 is used to perform the simulation. Note that the mass scaling factor and the mesh size were chosen after a parametric study to ensure kinetic forces are insignificant, i.e., less than 5% of inertia forces at each time increment. In the cantilever bending simulation, one end of the wire is fixed by constraining all degrees of freedom, while the other end is vertically displaced. The friction coefficients, radial force exerted by the insulation, material properties, and geometrical properties are the same as those used with the analytical model.

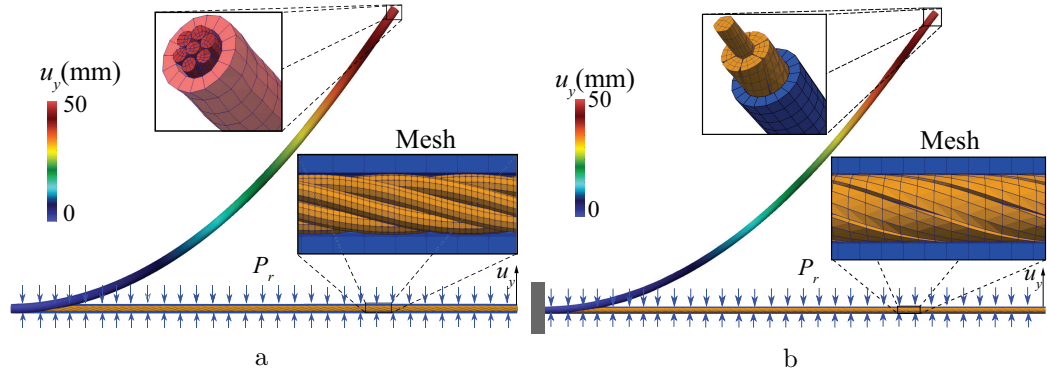


Figure 3.11: FE models of (a) A2-type and (b) B2-type wires showing portions of the mesh and simulated bent shape of the wires.

Figure 3.12 shows the measure force, simulated force, and analytical model output force as a function of tip displacement for A2 and B2-type wires .

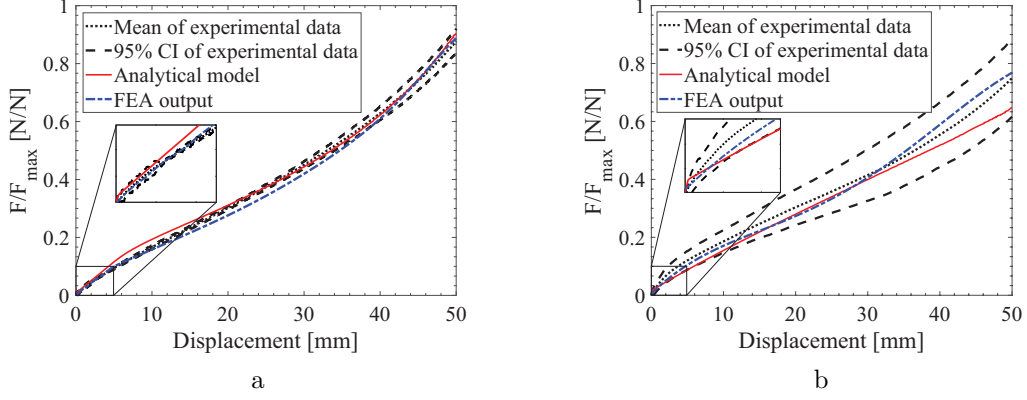


Figure 3.12: Force versus displacement plots showing the experimental data, analytical model output, and FE model output for wires (a) A2 and (b) B2.

The RMS error between the FE model output and the experiments is 0.0031 for A2-type wire and 0.0038 for B2-type wire. For the latter, there is a notable difference between the force outputs of the FE model and the analytical model at higher deflections. This difference could be due to higher friction between conductors resulting from a larger contact area with the compressed wires, as well as the different cross section geometry of compressed conductors. In the analytical model, the compressed conductor cross sections are modeled as perfect polygons to simplify calculations, while the polygon edges are rounded in the FE model to improve the fidelity of simulations. However, outputs of both the analytical model and the FE model are still within the 95% CI of the experimental data. The wavy nature of the FE model force output is caused by the mass scaling factor used to reduce the computational cost, as described by (author?) [39].

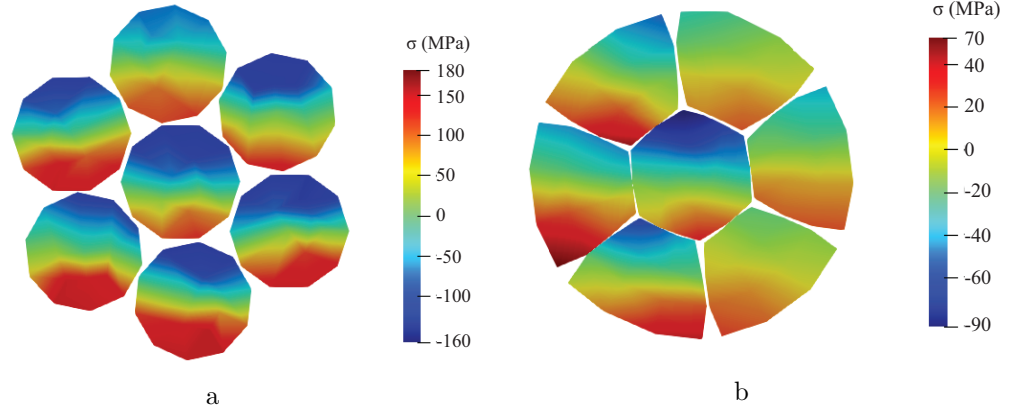


Figure 3.13: Von Mises stress distribution at the fixed end for (a) A2-type and (b) B2-type wires. The symmetric stress distribution in each wire supports the laminated stress distribution assumption presented in subsection 3.2.3.

Figure 3.13 shows that the stress profile in the conductors has a laminar form as proposed in subsection 3.2.3. Stress profiles in A2 are fairly uniform for all the conductors. However the stress profiles in B2-type wires are biased about the horizontal plane of symmetry. It is conjectured that this bias is due to the polygonal shape of the conductor cross sections, which interlock to resist twisting of the conductors, thus resulting in multiple sites of stress concentration.

### 3.6 Application

The analytical model presented in this chapter can be used to calculate the bending stiffness of a wire, given its dimensions and material properties. The procedure is:

1. The wire material properties and the dimensions are input in the form of an excel sheet.

2. The axial forces due to bending and friction (3.7), (3.14), (3.15) are calculated
3. An if-else condition is used to determine whether the wire strand is sticking or slipping w.r.t to the other strands
4. Based on the selected axial force the bending moment (3.17) in the wire is calculated as a function of curvature
5. An effective bending stiffness is derived from the moment-curvature relation assuming the wire to be a uniform cylindrical beam.

For calibration of new type of wires, i.e. different material properties, architecture, in addition to steps 1-5, the following steps need to be followed:

6. The large deflection formulations (equations (14) and (15)) are used to calculate the force-displacement response
7. The model parameters are tuned to minimize error between the experiment and the analytical model

The logic flow of the process is presented in Figure 3.14.

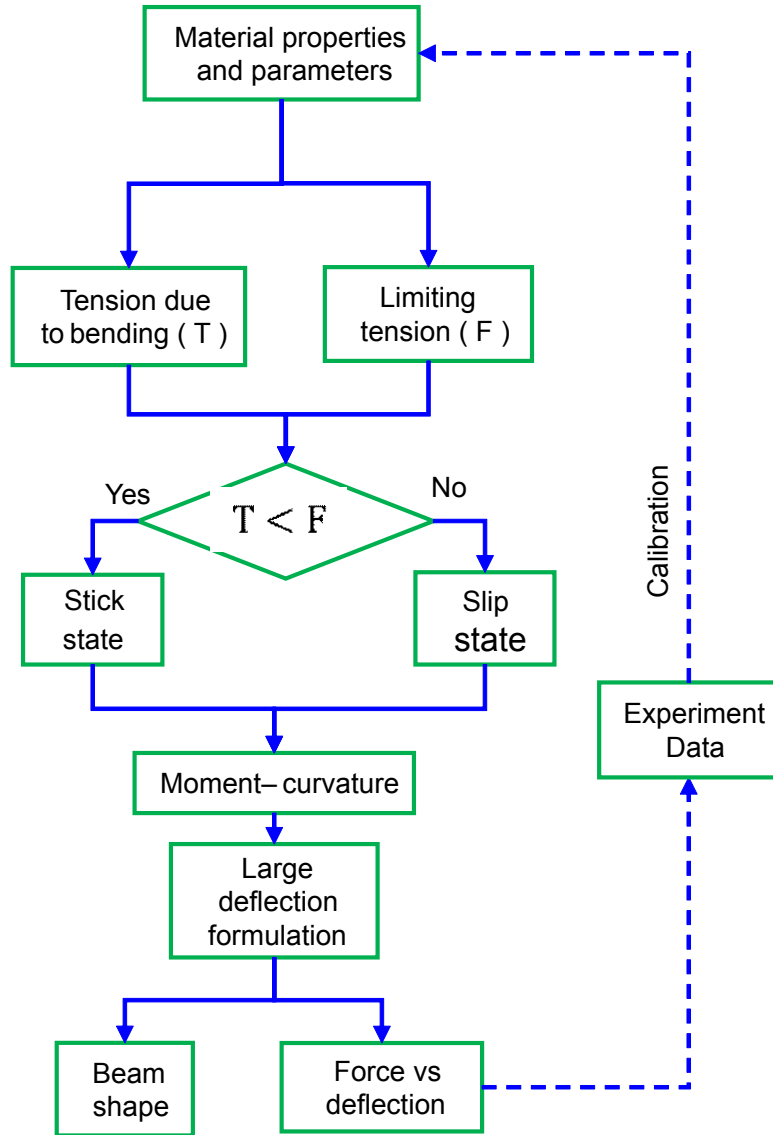


Figure 3.14: Logic flow of the analytical model.

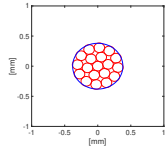
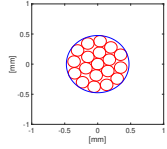
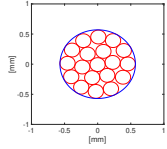
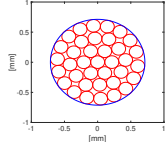
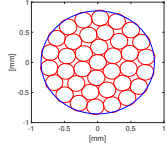
To demonstrate the use of the analytical model, a new wire type called C was chosen from the manufacturer's specification sheet. C-type wires are made of cylindrical copper strands wound in PVC insulation, similar to A-type wires. The dimensions of the wires modeled are shown in Table 3.4.

Table 3.4: Wire diameter, conductor area, number of conductors, and lay angles of the conductors of the five types of wires characterized using the analytical model.

Wire	$d_w$ (mm)	$A_c$ (mm <sup>2</sup> )	$N_s$	$\alpha_q$ ( $^\circ$ )
C1	1.4	0.38	19	12, -15
C2	1.6	0.54	19	12, -15
C3	1.8	0.79	19	12, -15
C4	2.1	1.28	37	12, -15, 12
C5	2.6	1.96	37	12, -15, 12

The model outputs bending stiffness and the predicted cross section of the wires, which are presented in Table 3.5. The wire strand layout matches the actual layout for typical helically wound 2-layered (19 strands) and 3-layered (37 strands) wires.

Table 3.5: Stick-state bending stiffness and predicted cross section of the five different sizes of C-type wires.

Wire	Stick state bending stiffness ( $\text{Nm}^2$ )	Cross section
C1	$1.46 \times 10^{-3}$	
C2	$2.75 \times 10^{-3}$	
C3	$6.22 \times 10^{-3}$	
C4	$16.96 \times 10^{-3}$	
C5	$39.87 \times 10^{-3}$	

## Chapter 4: Wire harness characterization

### Overview

*In the previous chapters, models and methods were presented for characterizing the mechanical behavior of individual components. In this chapter methods for characterizing two different types of harness bundles are presented. The taped wire bundle (TWB) and the conduit wire bundle (CWB). Samples were prepared to account for various types of wires, conduits, tapes and the method of taping. The objective of this section is to study and understand the interactions between various components of a wire harness.*

## 4.1 Introduction

As mentioned in Chapter 2, a wire harness is made by enclosing a bunch of wires in a protective covering such as a corrugated tube, twist tube, or tape. In order to characterize the whole wire harness, two types of harness samples were designed: taped wire bundles (TWB) and conduit wire bundles (CWB). Depending on the application, a wire harness may or may not include a protective conduit. In harnesses without the conduits the wires are taped over. Hence, the TWB and CWB samples cover both cases with and without protective conduit. Taped wire bundles are prepared by enclosing a bunch of wires in an insulation tape. Conduit wire bundles are prepared by enclosing a bunch of wires in a conduit and then taping around the conduit in different configurations.

## 4.2 Taped wire bundles

### 4.2.1 Sample preparation

Taped wire bundle samples were prepared by tightly winding a bunch of electrical wires with insulation tape. Two types of wires and tape were used for sample preparation and the different bundle configurations tested are shown in Table 4.1. B1 and B2-type wires were chosen as they are the most commonly used wires in the automobile as informed by the industry sponsor and for insulation, polyvinyl chloride (PVC) and polyester (PET) tape was used. The required number of wires ( $N$ ) are cut off from the spool, straightened and mounted in drill chucks as shown in Figure 4.1. Then the insulation tape is wound around the sample in a half-lap configuration. In a half-lap configuration, half the width of the tape overlaps in each winding. A radial force is applied during the taping process to ensure the wires are tightly enclosed.

Table 4.1: Types of taped wire bundles tested as part of this study.

Wire type	Insulation	Number of wires
B1	PVC	7
		12
		19
B2	PVC	7
		12
		19
B1 & B2	PVC	10 B1 & 9 B2 9 B1 & 10 B2
B1	PET	19
B2	PET	7
		19

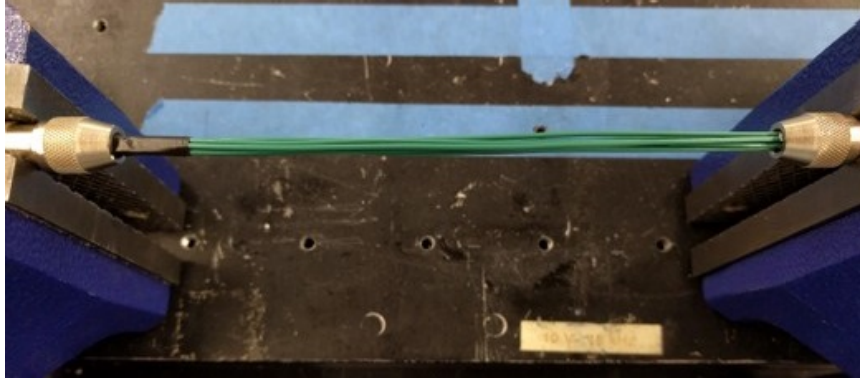


Figure 4.1: Taped wire B1 bundle mounted in drill chucks for taping.

The taped bundles are cut into 140 mm (5.5 in) long samples. One end of the sample is inserted in a 25.4 mm (1 in) long poly-carbonate tube and cast in Gorilla<sup>®</sup> epoxy and cured for 24 hours. The poly-carbonate tube is held in clamps as shown in Figure 4.1 and mounted on the load frame as mounting the sample directly would radially compress the wires. The epoxy creates a firm interface between the wire bundle and the poly-carbonate tube ensuring a perfect cantilever condition

(slope = 0 at the fixed end). The length of the cantilever beam is 114.3 mm (4.5 in). Hemispherical motion capture markers are placed along the length of the sample at 0.5 in intervals. The motion capture markers measure the shape of the wire bundles during the test. Motion capture data is also used to measure the tip displacement relative to the fixed end.

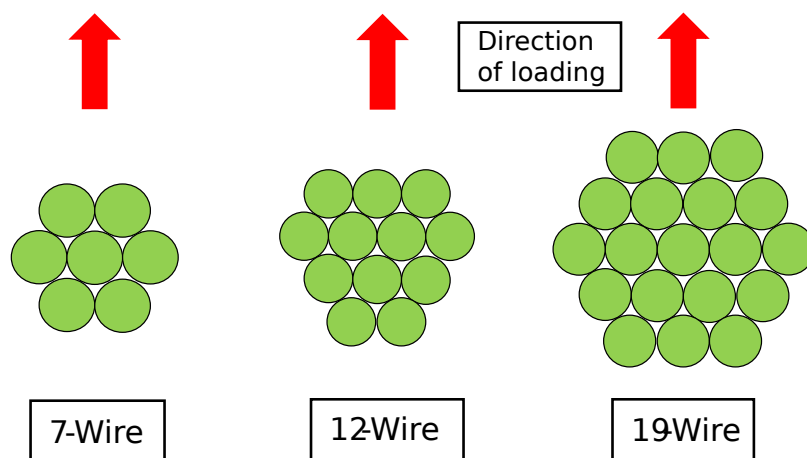


Figure 4.2: Schematic showing taping wire bundle cross sections for different number of wires.

The cross section schematic is shown in Figure 4.2. seven-wire and nineteen-wire bundles form perfect hexagons with a core and one and two layers of wires, respectively. Twelve-wire and 27-wire bundles form a distorted hexagon with three wires forming the core and one and two layers surrounding them, respectively.

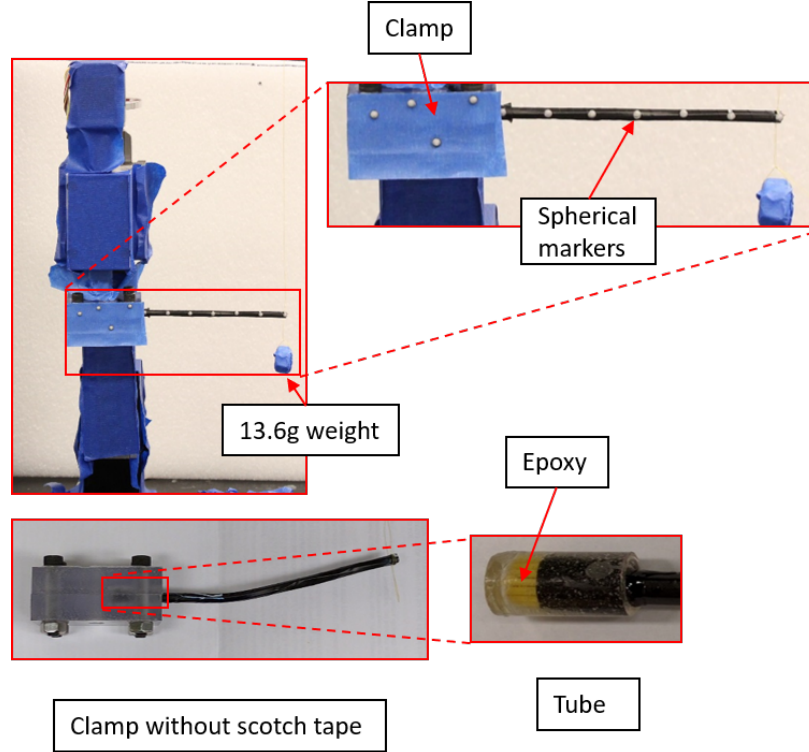


Figure 4.3: TWB sample preparation and setup showing the epoxy cast, polycarbonate clamp and the mounting of the sample.

#### 4.2.2 Test setup

A custom inverted cantilever setup was designed to characterize the bending stiffness of taped wire bundles. The setup is similar to the test setup used to characterize the singles wires presented in Chapter 2. The taped wire bundle test setup is shown in Figure 4.3. Poly-carbonate clamps are used to mount the samples on the load frame. The clamps enclose the poly-carbonate tube and are mounted using a  $1/4''$ -28 threaded bolt on to the load frame. The free end of the wire bundle is connected to a 2 lb Futek<sup>®</sup> load cell using an aramid strand. A counter weight is added to the free end to ensure the aramid strand is taut. A dSPACE<sup>®</sup> 1103 control box is used to

control the load frame motion and record the force as measured by the load cell. A SIMULINK<sup>®</sup> control algorithm is written in the ControlDesk software to control the motion of the load frame. The initial and final shapes of the TWB cantilever bending is shown in Figure 4.4

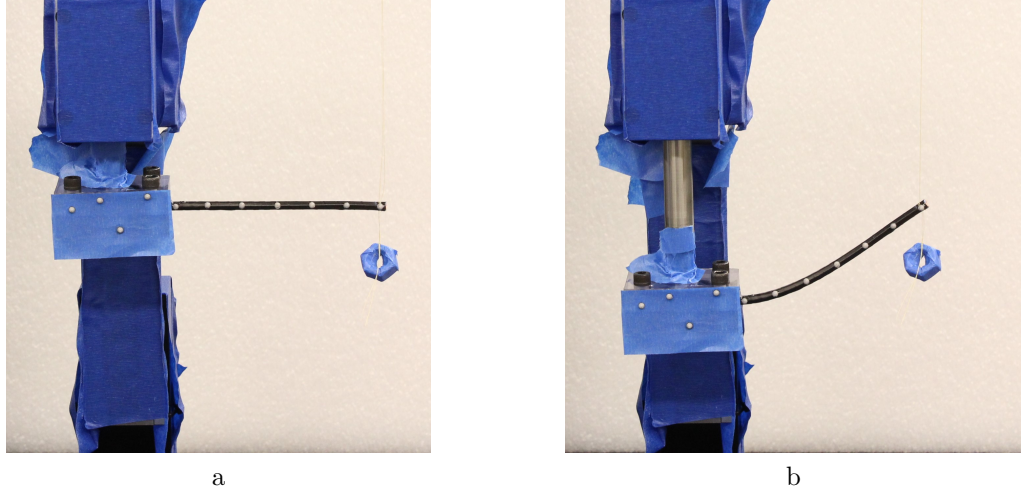


Figure 4.4: (a) Initial and (b) final stage of cantilever bending test of taped wire bundle.

### 4.2.3 Results

Three samples of each bundle type are tested. The samples are loaded and unloaded for three cycles and the load sensor data is sampled at 10 kHz. The noise is filtered during post-processing using a moving average filter in MATLAB. Figure 4.5 shows the force versus displacement and motion capture data for a B1-type nineteen-wire bundle. Cycles 2 and 3 show strain hardening. The strain hardening is due to two reasons: plastic deformation of the wires and the wires slipping against the tape during loading and locking in position during unloading.

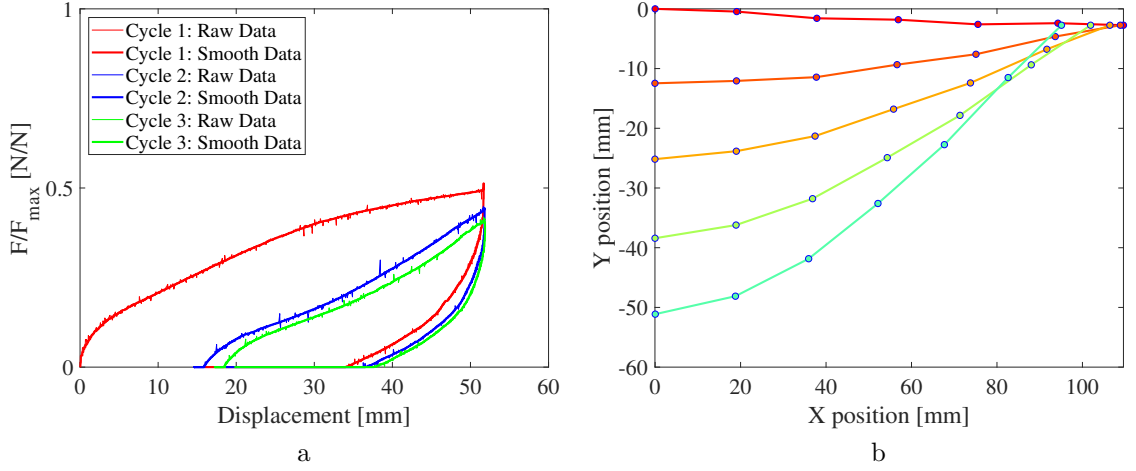


Figure 4.5: (a) Normalized force versus displacement and (b) motion capture data for cantilever bending test of B1-type nineteen wire bundle.

Normalized force of the first cycle loading is plotted as a function of the displacement as shown in Figures 4.6, 4.7, and 4.8. B2-type wire bundles have a higher bending stiffness than B1-type wire bundles, as B2-type wires are stiffer than B1-type wire (Chapter 2). Initially, wires are in firm contact with each other and are in a stick state. As the curvature increases, the wires start to slip against one another and the stiffness reduces. This change in stiffness can be observed for the TWB samples at around 2 mm displacement. The force response of nineteen-wire bundles plateaus at around 35 mm displacement as the wires start to slip against the tape. At this point, the aramid strand is pulling on the tape and not on the wires. For characterizing the wire bundles the initial 5 mm region is chosen.

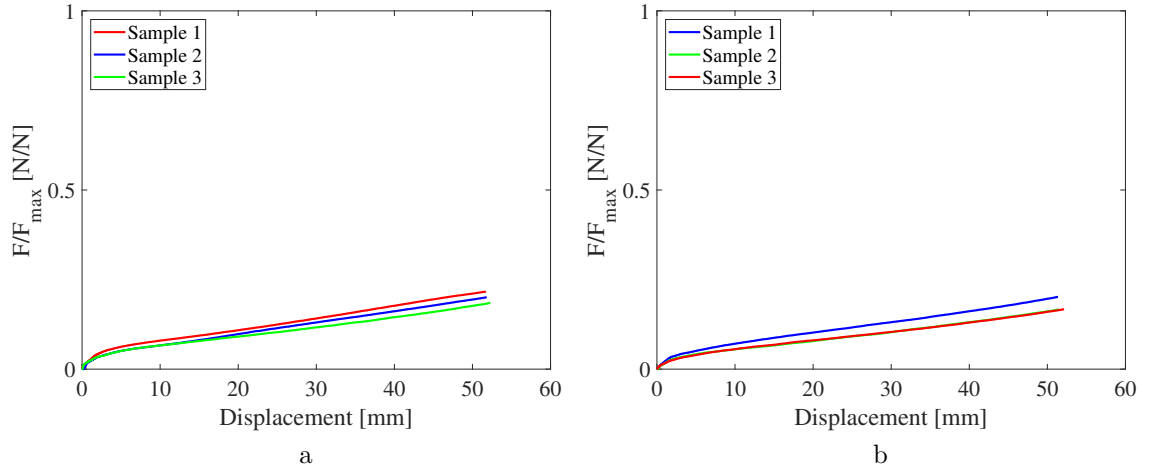


Figure 4.6: Plot showing the normalized force versus displacement of (a) B1-type and (b) B2-type seven-wire bundles.

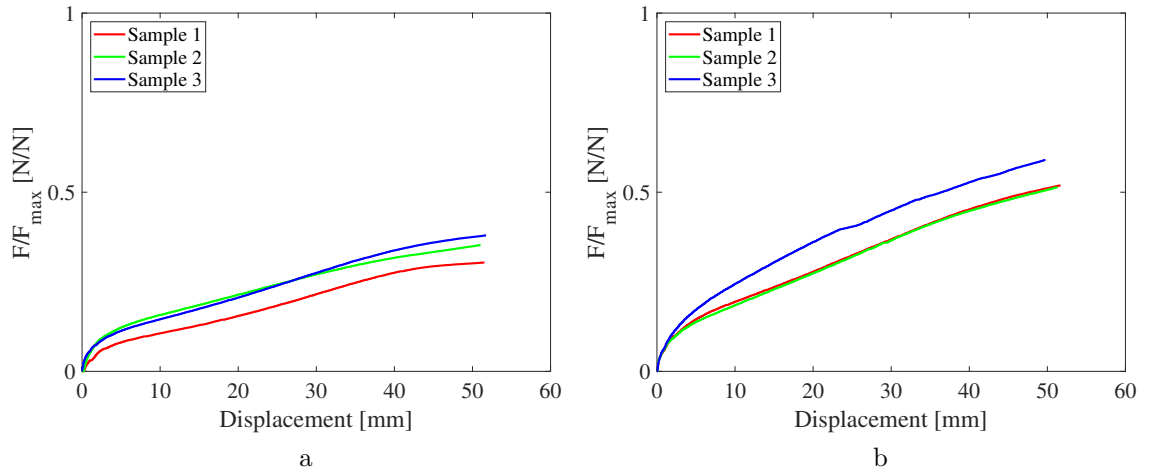


Figure 4.7: Plot showing the normalized force versus displacement of (a) B1-type and (b) B2-type twelve-wire bundles.

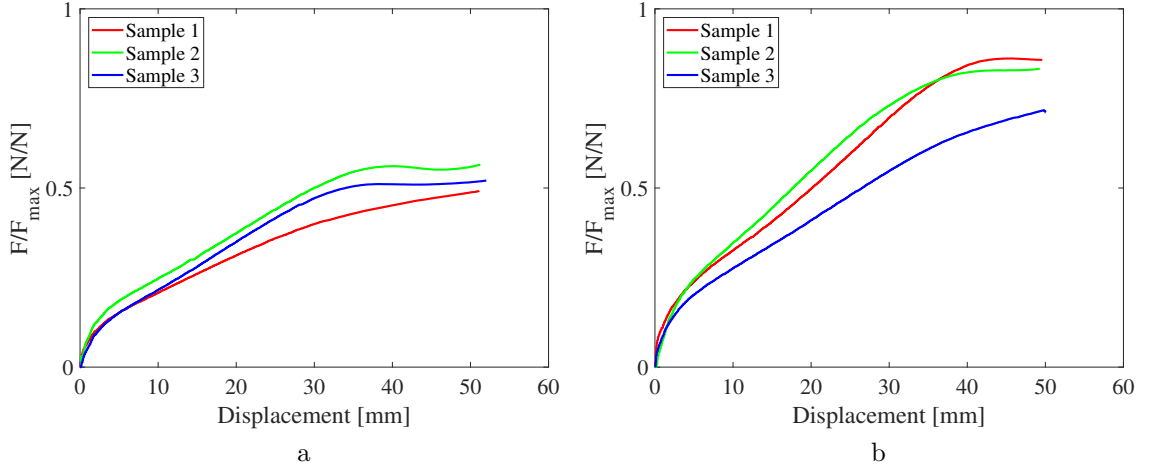


Figure 4.8: Plot showing the normalized force versus displacement of (a) B1-type and (b) B2-type nineteen-wire bundle.

As shown in Table 4.1, in addition to B1 and B2-type wire bundles, mixed wire bundles were also tested. A schematic of the mixed wire bundles is shown in Figure 4.9. Two different wire bundles with same number were tested to study the effect of the wire radial position on the bending stiffness of the wire bundle. Figure 4.9 shows a symmetric and asymmetric configurations of the wire bundles. In the symmetric configuration, the wires are evenly distributed across the bundle cross-section and in the asymmetric configuration the wires are biased towards one particular direction.

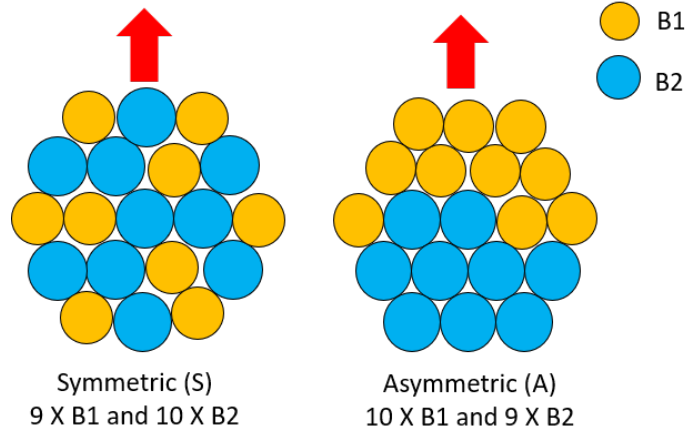


Figure 4.9: Mixed TWB samples showing two different configurations of the wire bundles.

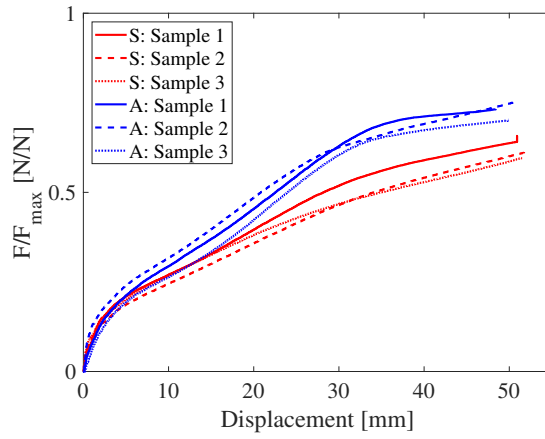


Figure 4.10: Normalized force versus displacement plots of two different cases of mixed wire TWBs.

The normalized force versus displacement plots for the mixed TWB are shown in Figure 4.9. The force profile shows that the asymmetric bundle has a higher stiffness

than the symmetric bundle, even though the asymmetric bundle only has nine B2-type wires. It can be inferred that the radial position of the wire in a wire bundle affects the bending stiffness of the bundle. This can also be proved from Euler's beam theory, which states that the bending stiffness is proportional to the distance from the neutral plane.

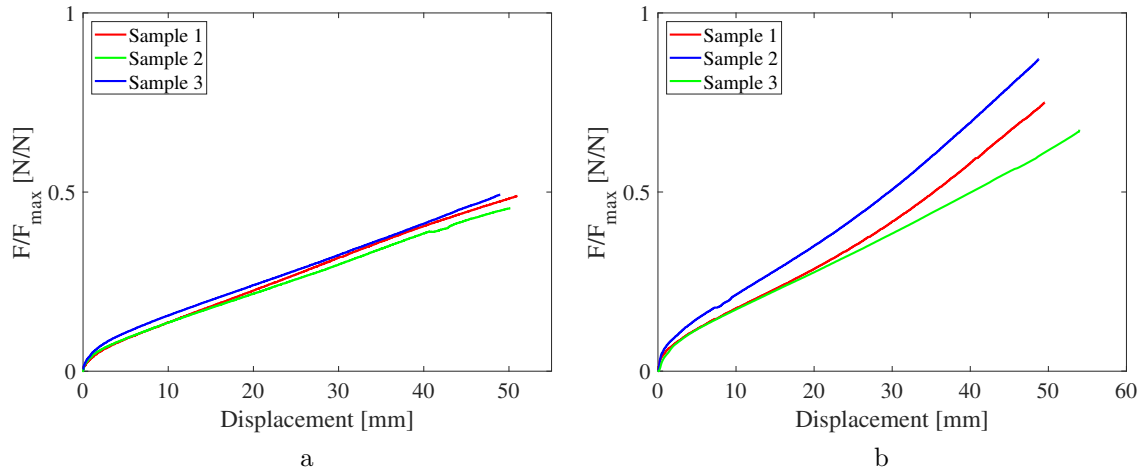


Figure 4.11: Plot showing the normalized force versus displacement of (a) B1-type and (b) B2-type nineteen-wire bundle with PET tape.

As shown in Table 4.1, TWB samples were also made with PET tape. nineteen-wire bundles with B1-type and B2-type wires are prepared and the force versus displacement plot is shown in Figure 4.11. The force response does not show a plateau, indicating no slip between the tape and the wires. It can be inferred that the glue used in the PET tape is stronger than the glue used in the PVC tape.

### 4.3 Conduit wire bundles

Conduit wire bundles are prepared by enclosing a bunch of electrical wires in a conduit and taping over the conduit. The different configurations of conduit wire bundles tested are shown in Table 4.2. The bundles can be without the insulation tape or with either coarse taping or half-lap taping. In 'no tape' configuration, only the exposed wires are taped, the conduit is not taped and only unslit corrugated tube is used in that configuration as using a slit conduit without taping results in the wires getting exposed. In coarse taping, the tape is applied at an interval equal to the tape width. In half-lap taping, the tape is applied such that half the width of the tape in a winding overlaps half the width of the previous winding. The protective conduit can be a slit corrugated tube, an unslit corrugated tube, or a PET twist tube.

Table 4.2: Types of composite wire bundles tested as part of this study.

Case	Wire type	Number of wires	Conduit	Taping
1	B1	19	Corrugated tube	No tape
2	B2	19	Corrugated tube	(a) No tape (b) Coarse tape (c) Half-lap tape
3	B2	12	Corrugated tube	No tape
4	B1 & B2	10×B1 9×B2	Corrugated tube	No tape
5	B1	19	Twist tube	No tape
6	B2	19	Twist tube	No tape

### 4.3.1 Sample preparation

The test setup and the sample dimensions were chosen based on ASTM D790 [3] for measuring the flexural properties of unreinforced and reinforced plastics and electrical insulating materials. Conduit wire bundle (CWB) samples are made of wires, protective conduits, and tape. The required number of electrical wires are cut off the spool and gently straightened and trimmed to 8 in length. A 6 in long protective conduit is inserted around the wires such that 1 in of the wire is out of the conduit on each side. The ends of the CWB are taped to cover any exposed wires. Depending on the chosen configuration, the conduits are also taped. Spherical motion capture markers are placed along the length of the CWB at 0.5 in intervals. The CWB sample can be compared to a human limb, where the wire bundle is similar to the bone and the conduit is similar to the skin. Hence, the sample is initially straight as the conduit takes the shape of the wires.

### 4.3.2 Test setup

The test setup for characterizing CWBs is shown in Figure 4.12. An MTS Criterion 43 load frame is used for the test. The sample is mounted using MTS three-point-bend fixtures with 10 mm diameter roll pin. The built-in MTS load cell has a rating of 50 kN, but the maximum force in the test is less than 10 N. Hence a 500 lb load cell is mounted on the load frame using a custom adapter. Data from the 500 lb load cell is recorded using a dSPACE 1103 data acquisition system. The loading rate is setup in the MTS TestSuite software which controls the load frame. The dSPACE system is synced with the load frame to start simultaneously. When

the test is started, the TestSuite software triggers the dSPACE 1103 system to start recording.

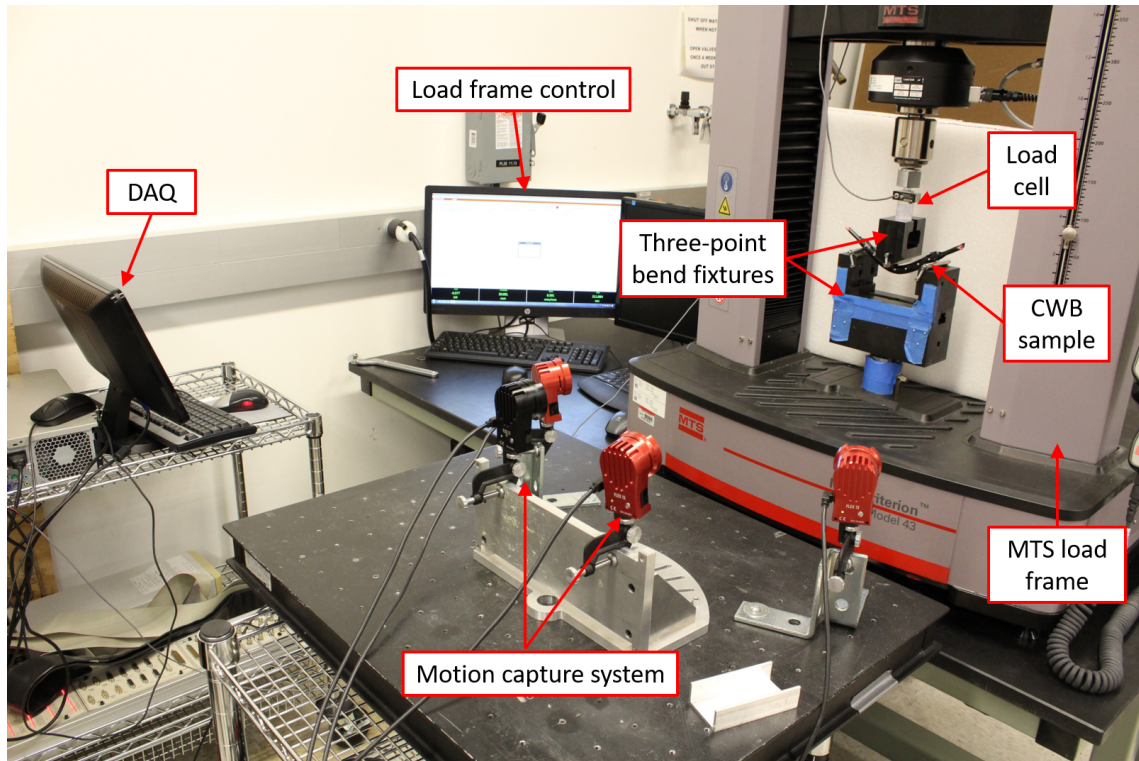


Figure 4.12: Conduit wire bundle test setup showing the load frame, fixtures, data acquisition, and motion capture system.

To record the shape of the CWB sample during the test, an OptiTrack motion capture system with 4 cameras is used. The motion capture system is calibrated to record any reflections in the test area, hence the test fixtures are covered in anti-reflective tape. 3 mm diameter spherical markers are placed along the length of the CWB sample at 0.5 in intervals. As the sample is cylindrical in shape, the motion capture markers also allow for correcting any twist in the sample during loading.

Procedure of testing a CWB sample:

1. Cut electrical wires off the spool and gently straighten them
2. Choose a protective conduit of a suitable diameter such that the packing fraction is approximately 0.7
3. Start taping over the wires and tape on to the tube according to the chosen configuration, i.e., untaped, half-lap, or coarse tape
4. Setup the motion capture system and calibrate the space around the three-point bend fixtures
5. Mount the sample on the MTS frame such that the sample overhangs by 1 in on either side
6. Place 3 mm diameter motion capture markers along the length of the sample
7. Initialize the load frame such that the top fixture touches the sample
8. Set the test parameters in the MTS TestSuite software
9. Start the test and the motion capture system system
10. Once the test ends, export the data as a .xlsx file for post processing

Figure 4.13 shows the initial, fully bent, and final shapes of a CWB sample under three-point bending.

### **4.3.3 Results**

Three samples of each CWB type are tested under three-point-bending and the normalized force versus displacement response of three-point bending of conduit wire bundles is presented in this section. The results show that the wires are a major

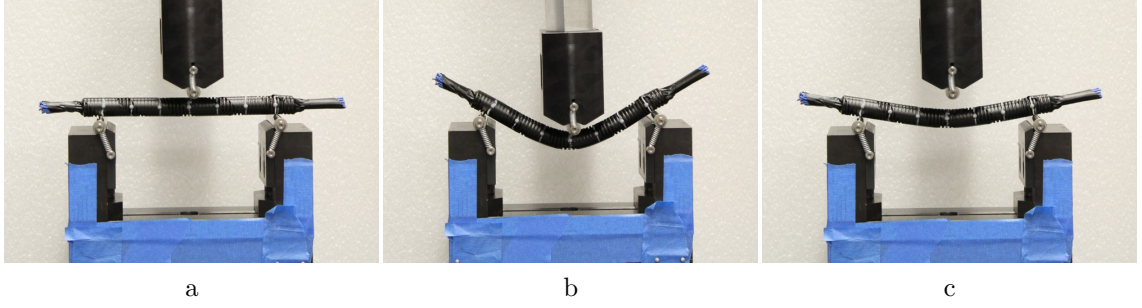


Figure 4.13: (a) Initial, (b) fully bent, and (c) final shape of a conduit wire bundle under three-point-bending.

contributor to the bending stiffness of a conduit wire bundle. Figure 4.14 shows the normalized force versus displacement plot and the motion capture plot of CWB case 1. The motion capture data shows the shape of the sample at intervals of 10 mm vertical deflection.

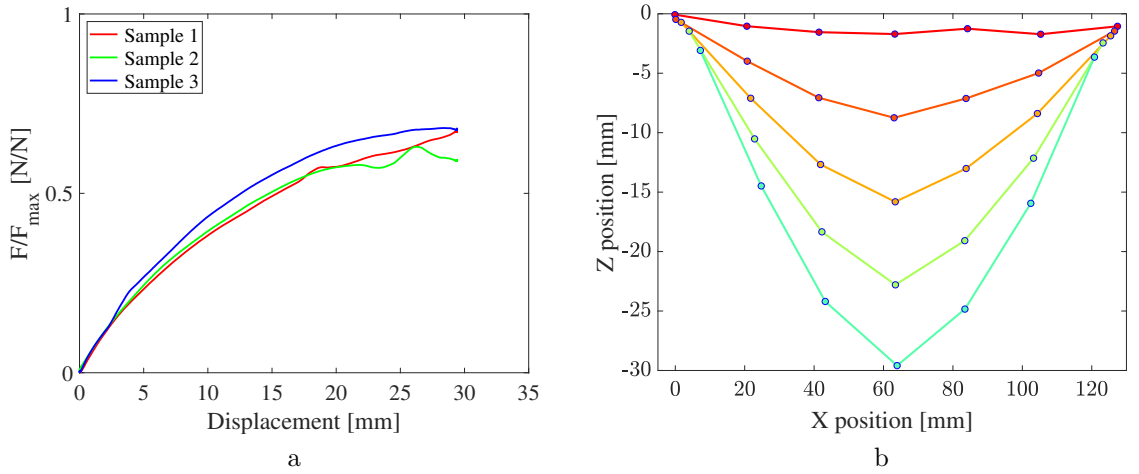


Figure 4.14: Normalized force versus displacement and motion capture plot of a B1-type nineteen-wire CWB sample.

The plateau in force displacement suggests that slip occurs between the wires and the tape at high deflections. Figure 4.15 shows the normalized force versus displacement plot of a B2-type nineteen-wire CWB bundle. The force response of the three types of samples are in same region. This suggests that the wires dominate the stiffness of the CWBs and the type of tape or conduit has a minimal effect.

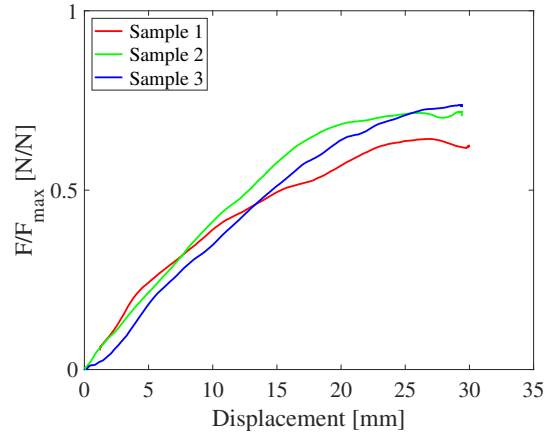


Figure 4.15: Normalized force versus displacement of a B2-type 19-wire CWB sample. The three cases of no tape, coarse tape, and half-lap tape are shown

Cases 3 and 4 represent the B2-type 12-wire bundles and mixed bundles respectively. The force response of the 19 wire mixed bundle is in between the force response of cases 1 and 2.

Cases 5 and 6 are for CWBs made with twist tube. The force response of testing cases 5 and 6 is similar to cases 1 and 2. This reinforces the inference that the wires have a major effect on the bundle bending stiffness.

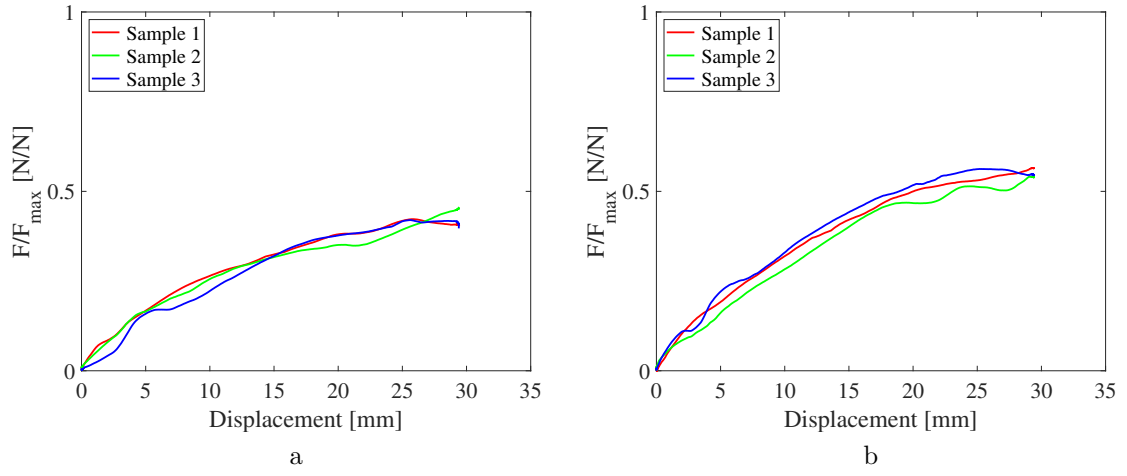


Figure 4.16: Normalized force versus displacement of B2-type twelve-wire sample and a mixed wire CWB sample.

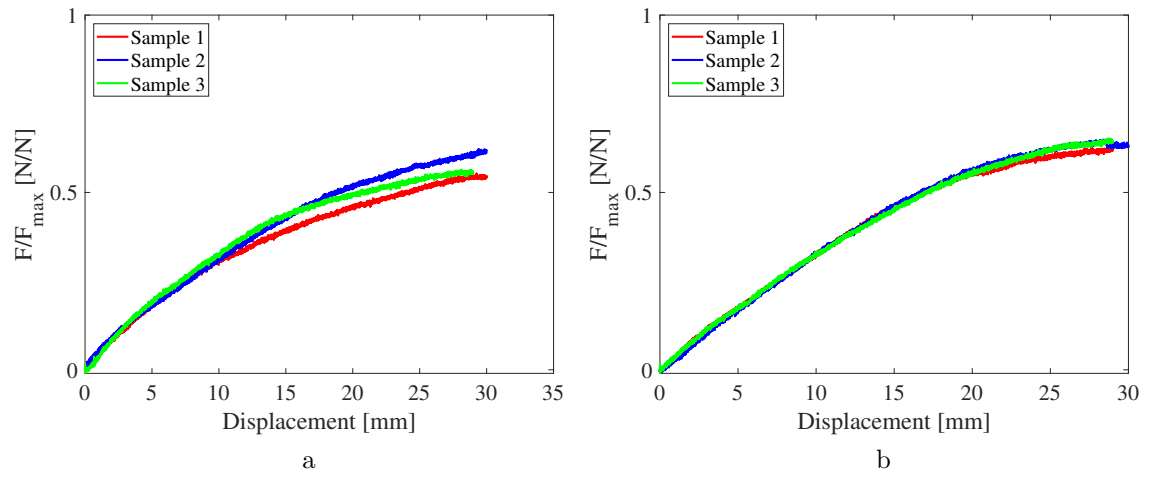


Figure 4.17: Normalized force versus displacement of B1-type and B2-type nineteen-wire CWB samples made with twist tube.

## Chapter 5: Conclusion

### 5.1 Summary of findings

Digital manufacturing allows for faster development time, reduced number of prototypes, and finally allows proper assembly to reduce after market issues. However, current software lack accurate material properties to model the behavior of flexible components such as wire harnesses and also lack models to predict the exact behavior of wire harnesses. To bridge this gap, experimental techniques and analytical models were developed to accurately characterize and model the mechanical behavior of wire harnesses under various loading modes such as bending, tension, and torsion.

As a first step, experiments were developed to characterize individual harness components such as electrical wires, conduits, and insulation tape. Harnesses primarily undergo bending loads and due to the orthotropic nature of electrical wires, the experimental effort was focused on characterizing the bending behavior of electrical wires and not their tensile behavior. In developing the experimental methods for characterizing electrical wires, a literature study was conducted focusing on the experimental effort to characterize wire rope structures such as overhead electrical lines and suspension bridge cables. The protective conduits and insulation tape show a similar behavior in tension and bending due to their architecture. Hence the conduits

and the tape were characterized to measure the tensile modulus. The experiments were developed based on ASTM standards for characterizing polymers used in the manufacture of conduits and tape.

An analytical model was also developed to simulate the bending behavior of electrical wires. Due to the large number of electrical wires used by the automobile industry, developing an analytical model to characterize the bending behavior of wires with a wire-rope structure helps in complementing the experimental effort. the analytical model was developed based on various models available in the literature for characterizing the mechanical behavior of cabled structures.

As a final step, experiments were developed to study the mechanical behavior of using multiple components such as wires, conduits, and tape together. This study helps in understanding the combined effect as well as to characterize the interactions between various components. As harnesses predominantly undergo bending deformation, the experiments were focused on characterizing the bending behavior of wire harnesses. Two different cases were identified, harnesses with wires taped with insulation tape and harnesses with conduits and insulation tape. To characterize both cases, taped wire bundle (TWB) and conduit wire bundle (CWB) samples were developed. The samples were prepared covering different combinations of wires, conduits, tape, and the methods of taping. The experiments suggests that a harness is similar to a human limb, where the wires act as a bone and the protective covering acts as the skin. Hence, the wire contribute to a majority of the bending stiffness of the harnesses. The purpose of the conduits and tape is to only keep the wires in place.

## 5.2 Contributions

- **Characterization of electrical wires.** Wire harnesses predominantly experience bending loads and, as such, testing methods were developed to characterize the bending behavior of electrical wires. A custom cantilever bending test was developed to characterize the single wire. The force versus displacement data was used to calibrate the analytical modeling effort of single wires. A motion capture system was used to record the shape of the wire during bending. The shape helps in performing a qualitative validation of the analytical model.
- **Analytical model.** Analytical equations were developed to model the bending behavior of electrical wires. The equations represent a stick-slip formulation to model the interaction between the conductor strands and also between the conductor and the insulation. The model takes into account large deformation of the wire harnesses by assuming a non-linear relation between the curvature and bending moment. The model includes an algorithm to estimate the radial position of conductor strands in an electrical wires from the wire outer diameter, strand diameter, and the number of strands. This algorithm enables the automation of the wire modeling process by allowing to directly input the wire dimensions from the manufacturer's specification sheet.
- **Plastic deformation of cabled structures.** A formulation was developed to model the plastic deformation of a helical structure. The model assumes the conductor strand as a laminated beam with each laminate having a different Young's modulus. The modulus of the laminate varies based on the longitudinal

strain in the laminate and is derived from a look-up table of annealed copper stress-strain values.

## Appendix A: MATLAB Codes

The following is a list of MATLAB codes used in the preparation of this thesis.

**NOTE:** The codes do not include the normalization factor used to protect the data.

The idea of attaching the codes is to show the procedure used in processing the raw data.

1. Single wire cantilever bend test:

Code for processing the load cell data:

```
1 % ==== SAI SIDDHARTHA VEMULA
2 % ==== Ohio State University
3 clc
4 clear all
5 close all
6
7 %% Read data from folder
8 Forcefile = '';
9 load(Forcefile);
10
11 %% Define X and Y, normalize, downsample, smooth, and find
    the peak in cycle 1
12 X = Force_data.X.Data;
13 X = X - X(1);
14 Y = Force_data.Y(3).Data;
15 DS_ratio = 200;
16 Y_D = downsample(Y,DS_ratio);
17 X_D = downsample(X,DS_ratio);
18 Y_DS = smooth(Y_D,0.001,'moving');
19 L_YD = length(Y_D);
20 [YD_max,YD_m_id] = max(Y_D(1:floor(L_YD/3+L_YD/8)));
21
22 figure;
23 plot(X,Y,'y');hold on;
24 plot(X_D,Y_D,'r');
25 plot(X_D,Y_DS,'g');
26 hold on
27
28 Start = max(find(X_D<=(X_D(YD_m_id)-53)) );% find starting
    point
29 X_N = X_D(Start:end);
30 X_N = X_N-X_N(1); %Normalize time again
31 Y_N = Y_D(Start:end);
32
33 L_YN = length(Y_N);
34 [Y_Nmax, Y_Nmax_id] = max(Y_N(1:floor(L_YN/3+L_YN/8)));
35 Peak1 = X_N(Y_Nmax_id);
36
37 %% Separate the force data into different cycles
38 j1=1;k1=1;j2=1;k2=1;j3=1;k3=1;
39
40 C_t = 53;
```

```

41 Y1 = 0;
42 Y2 = 0;
43 Y3 = 0;
44 Y4 = 0;
45 Y5 = 0;
46 Y6 = 0;
47 for i=1:length(X_N)
48     if X_N(i)<=X_N(Y_Nmax_id)
49         Y1(j1) = Y_N(i);
50         j1=j1+1;
51     elseif( X_N(i)>X_N(Y_Nmax_id) && X_N(i)<=X_N(Y_Nmax_id)+
        C_t)
52         Y2(k1) = Y_N(i);
53         k1=k1+1;
54     elseif( X_N(i)>X_N(Y_Nmax_id)+C_t && X_N(i)<=X_N(
        Y_Nmax_id)+2*C_t)
55         Y3(j2) = Y_N(i);
56         j2=j2+1;
57     elseif( X_N(i)>X_N(Y_Nmax_id)+2*C_t && X_N(i)<=X_N(
        Y_Nmax_id)+3*C_t)
58         Y4(k2) = Y_N(i);
59         k2=k2+1;
60     elseif( X_N(i)>X_N(Y_Nmax_id)+3*C_t && X_N(i)<=X_N(
        Y_Nmax_id)+4*C_t)
61         Y5(j3) = Y_N(i);
62         j3=j3+1;
63     elseif X_N(i)>X_N(Y_Nmax_id)+4*C_t
64         Y6(k3) = Y_N(i);
65         k3=k3+1;
66     end
67 end
68
69 F_I1 = M2R(Y1);
70 F_IS1 = smooth(F_I1,0.05,'moving');
71
72 F_I2 = M2R(Y2);
73 F_IS2 = smooth(F_I2,0.05,'moving');
74
75 F_I3 = M2R(Y3);
76 F_IS3 = smooth(F_I3,0.05,'moving');
77
78 F_I4 = M2R(Y4);
79 F_IS4 = smooth(F_I4,0.05,'moving');
80
81 F_I5 = M2R(Y5);

```

```

82 F_IS5 = smooth(F_I5,0.05,'moving');
83
84 F_I6 = M2R(Y6);
85 F_IS6 = smooth(F_I6,0.05,'moving');
86
87 F_I = horzcat(F_I1,F_I2,F_I3,F_I4,F_I5,F_I6);
88 F_I = F_I - F_I(1);
89 F_IS = horzcat(F_IS1',F_IS2',F_IS3',F_IS4',F_IS5',F_IS6');
90 F_IS = F_IS - F_IS(1);
91 X_N = X_N - X_N(1);
92 figure;
93 plot(X_N,F_I);
94 hold on;
95 plot(X_N,F_IS)
96
97 save ForceData

```

Code for processing motion capture data:

```

1  % ==== SAI SIDDHARTHA VEMULA
2  % ==== Ohio State University
3  clc
4  clear all
5  close all
6  warning off
7  %% Read data from folder
8  MoCapfile = ''; % Motion capture file
9  MoCap = xlsread(MoCapfile);
10 %% Parameters of sample
11 Wire_length_measured = 116.85;
12 Wire_type = ''; % Wire type
13 Wire_size = ''; % Wire size
14 Sample = ; % Sample number
15
16 time_i = MoCap(8:end,2);
17 x_i = zeros(length(time_i),8);
18 y_i = zeros(length(time_i),8);
19 z_i = zeros(length(time_i),8);
20 for j = 1:7
21     k(j) = j*2+j;
22     p((k(j)-2):k(j)) = find(MoCap(4,MarkerStart:MarkerEnd)==j
23         );
24 end
25 for i = 1:7
26     x_i(:,i+1) = MoCap(8:end,MarkerStart+p(3*i-2)-1);
27     y_i(:,i+1) = MoCap(8:end,MarkerStart+p(3*i-2));

```

```

27     z_i(:,i+1) = MoCap(8:end,MarkerStart+p(3*i-2)+1);
28 end
29
30 % Add rigid body to the first column
31 RB_x1 = 27;
32 x_i(:,1) = MoCap(8:end,RB_x1);
33 y_i(:,1) = MoCap(8:end,RB_x1+1);
34 z_i(:,1) = MoCap(8:end,RB_x1+2);
35
36 % Normalize coordinates
37 time_i = time_i - time_i(1);
38 x_i = x_i-x_i(1,1);
39 y_i = y_i-y_i(1,1);
40 z_i = z_i-z_i(1,1);
41
42 L_i = length(y_i)/3+length(y_i)/8;
43 [m1,q1] = min((y_i(1:floor(L_i),1))); % Find the min y which
    is the first peak
44 Start_M = max(find(time_i<=(time_i(q1)-53)));
45 if time_i(q1)-53>=0;
46     x = x_i(Start_M:end,:);
47     y = y_i(Start_M:end,:);
48     z = z_i(Start_M:end,:);
49     time = time_i(Start_M:end,:);
50 else
51     x = x_i;
52     y = y_i;
53     z = z_i;
54     time = time_i;
55 end
56
57 % Normalize coordinates according to rigid body
58 x = x-x(1,1);
59 y = y-y(1,1);
60 z = z-z(1,1);
61 time = time - time(1,1);
62 plot(time,y)
63
64 %% Coordinates Rotation: Coordinates rotate to the axis where
    stepper motor moves to
65 L = length(y)/3+length(y)/8;
66 [m,q] = min((y(1:floor(L),1)));
67 v1 = [x(q,1),m,z(q,1)];
68 v2 = [0,-norm(v1),0];

```

```

69 R = rotationmatrix(v1,v2); % Use function to find out the
    rotational matrix
70
71 % Calculation results: each column is each marker
72 x_r0 = zeros(8,length(time));
73 y_r0 = zeros(8,length(time));
74 z_r0 = zeros(8,length(time));
75
76 for i = 1:8
77     v1_mat = [x(:,i) y(:,i) z(:,i)];
78     v2_mat = R*v1_mat';
79     x_r0(i,:) = v2_mat(1,:);
80     y_r0(i,:) = v2_mat(2,:);
81     z_r0(i,:) = v2_mat(3,:);
82 end
83
84 % Define grip point
85 x0_ini = x_r0(2,1) + Grip_Point;
86 y0_ini = y_r0(2,1);
87 z0_ini = z_r0(2,1);
88 x0 = x_r0(1,:)+x0_ini;
89 y0 = y_r0(1,:)+y0_ini;
90 z0 = z_r0(1,:)+z0_ini;
91
92 % New data adding grip point
93 x_r0g = [x_r0(1,:); x0; x_r0(2:end,:)];
94 y_r0g = [y_r0(1,:); y0; y_r0(2:end,:)];
95 z_r0g = [z_r0(1,:); z0; z_r0(2:end,:)];
96
97 %% Define pull point
98 % Define x-step in derivative
99 Del_x = 0.0001;
100
101 % Present last marker points
102 x_r0g_end = x_r0g(end,:);
103 y_r0g_end = y_r0g(end,:);
104 z_r0g_end = z_r0g(end,:);
105
106 % Define a point very close to present last marker points
107 x_r0g_n_end = x_r0g(end,:)- Del_x;
108 n = length(time);
109 Del_y = zeros(1,n);
110
111 for i = 1:n
112     f = polyfit(x_r0g(2:end,i),y_r0g(2:end,i),4);

```

```

113     Fit_end = polyval(f,x_r0g_end(i));
114     Fit_n_end = polyval(f,x_r0g_n_end(i));
115     Del_y(1,i) = Fit_end - Fit_n_end;
116 end
117
118 Slope = Del_y/Del_x;
119 x_pl = P2RM*cos(atan(Slope))+x_r0g_end;
120 y_pl = P2RM*sin(atan(Slope))+y_r0g_end;
121 z_pl = z_r0g_end;
122
123 % Final data adding pull point
124 x_r = [x_r0g;x_pl];
125 y_r = [y_r0g;y_pl];
126 z_r = [z_r0g;z_pl];
127 x_r = x_r';
128 y_r = y_r';
129 z_r = z_r';
130
131 plot(time,y_r)
132 hold on;
133 legend('1','2','3','4','5','6','7','8','9','10');
134
135 save Motion_Capture

```

Code for plotting the force - displacement data

```

1 % ==== SAI SIDDHARTHA VEMULA
2 % ==== Ohio State University
3 clc
4 close all
5 clear all
6
7 %% Data processing
8 load Motion_Capture
9 load ForceData
10
11 % Calculate the net deflection of the tip from the fixed end;
12 tip_deflection = y_r(:,10) - y_r(:,2);
13 tip_deflection = tip_deflection - tip_deflection(1); %
    Normalize tip deflection
14 tip_deflection = tip_deflection*1e3; % from [
    m] to [mm]
15
16 %% Separate the cycles
17 j = 1;k = 1;n = 1;

```

```

18 [y_max,y_m_index] = max(tip_deflection(1:floor(length(time)
    /3+length(time)/8)));
19 Peak_M1 = time(y_m_index);
20 comp = Peak1-Peak_M1;
21
22 for i=1:length(time)
23
24     if(time(i)<Peak_M1+C_t)
25         cycle1_deflection(j) = tip_deflection(i);
26         cycle1_time(j) = time(i);
27         j=j+1;
28     elseif(time(i)>=Peak_M1+C_t && time(i)<Peak_M1+3*C_t)
29         cycle2_deflection(k) = tip_deflection(i);
30         cycle2_time(k) = time(i);
31         k=k+1;
32     elseif(time(i)>=Peak_M1+3*C_t && time(i)<Peak_M1+5*C_t)
33         cycle3_deflection(n) = tip_deflection(i);
34         cycle3_time(n) = time(i);
35         n=n+1;
36     end
37 end
38
39 % time in motion capture is lacking initially, thus
40 % compensate here, which we can see from plot(time,
    tip_deflection)
41 cycle1_time = cycle1_time+comp;
42 cycle2_time = cycle2_time+comp;
43 cycle3_time = cycle3_time+comp;
44
45 % If cycle1_time < 0, eliminate these data
46 if cycle1_time(1) < 0;
47     index = find(cycle1_time>=0);
48     cycle1_time_N = cycle1_time(index);
49     cycle1_deflection_N = cycle1_deflection(index);
50 elseif cycle1_time(1) >= 0;
51     cycle1_time_N = cycle1_time;
52     cycle1_deflection_N = cycle1_deflection;
53 end
54 figure;
55 plot(cycle1_time_N,cycle1_deflection_N)
56
57 % To interpolate and call forces from force-time data
58
59 [cycle1_Force, cycle1_Force_S] = ForceDispLookup(
    cycle1_time_N);

```

```

60 [cycle2_Force, cycle2_Force_S] = ForceDispLookup(cycle2_time)
    ;
61 [cycle3_Force, cycle3_Force_S] = ForceDispLookup(cycle3_time)
    ;
62
63 % Normalize force
64 F_ini = cycle1_Force(1);
65 F_ini_S = cycle1_Force_S(1);
66 cycle1_Force = cycle1_Force - F_ini;
67 cycle2_Force = cycle2_Force - F_ini;
68 cycle3_Force = cycle3_Force - F_ini;
69 cycle1_Force_S = cycle1_Force_S - F_ini_S;
70 cycle2_Force_S = cycle2_Force_S - F_ini_S;
71 cycle3_Force_S = cycle3_Force_S - F_ini_S;
72 for i=1:length(cycle1_Force)
73
74     if(cycle1_Force(i)<0)
75         cycle1_Force(i) = 0;
76     end
77     if(cycle1_Force_S(i)<0)
78         cycle1_Force_S(i) = 0;
79     end
80
81 end
82
83 for i=1:length(cycle2_Force)
84
85     if(cycle2_Force(i)<0)
86         cycle2_Force(i) = 0;
87     end
88     if(cycle2_Force_S(i)<0)
89         cycle2_Force_S(i) = 0;
90     end
91
92 end
93
94 for i=1:length(cycle3_Force)
95
96     if(cycle3_Force(i)<0)
97         cycle3_Force(i) = 0;
98     end
99     if(cycle3_Force_S(i)<0)
100         cycle3_Force_S(i) = 0;
101     end
102

```

```

103 end
104
105 Displ_all = [cycle1_deflection_N cycle2_deflection
               cycle3_deflection];
106 Force_all = [cycle1_Force cycle2_Force cycle3_Force];
107 Force_all_S = [cycle1_Force_S cycle2_Force_S cycle3_Force_S];
108 [Peak_L1,Peak_L1_I] = max(cycle1_deflection_N);
109 Peak_L1_I = Peak_L1_I - 45;
110 Displ_1stload = Displ_all(1:Peak_L1_I);
111 Force_1stload = Force_all(1:Peak_L1_I);
112 Force_1stload_S = Force_all_S(1:Peak_L1_I);
113 time_cycles = [cycle1_time_N,cycle2_time,cycle3_time];
114 time_cycles = time_cycles-time_cycles(1);
115 time_1stload = time_cycles(1:Peak_L1_I);
116 %% Plot displacement v/s Force
117
118 Colors = colormap(jet(11));
119 Colors = Colors([1:7,9:11],:);
120 Colors = flipud(Colors);
121 Colors = [Colors;[0 0 0]];
122
123 % All cycles
124 figure;
125 plot(cycle1_deflection_N,cycle1_Force,'r','linewidth',0.5)
126 hold on
127 plot(cycle1_deflection_N,cycle1_Force_S,'r','linewidth',2)
128 hold on
129 plot(cycle2_deflection,cycle2_Force,'b','linewidth',0.5)
130 hold on
131 plot(cycle2_deflection,cycle2_Force_S,'b','linewidth',2)
132 hold on
133 plot(cycle3_deflection,cycle3_Force,'g','linewidth',0.5)
134 hold on
135 plot(cycle3_deflection,cycle3_Force_S,'g','linewidth',2)
136 grid on;
137 xlabel('Displacement [mm]');
138 ylabel('Force [N]');
139 title([Wire_type ' ' Wire_size ' ' Wire_length ' sample '
          num2str(Sample) ' - cyclic test' ' ( test length : '
          num2str(Wire_length_measured) ' mm) '], 'FontSize',28, '
          FontWeight','bold');
140 legend('Cycle 1: Raw Data','Cycle 1: Smooth Data','Cycle 2:
          Raw Data','Cycle 2: Smooth Data','Cycle 3: Raw Data','
          Cycle 3: Smooth Data','Location','northwest');
141 savefig('Force_Displ.fig')

```

```

142
143 % Fisrt cycle
144 figure;
145 plot(Displ_1stload,Force_1stload,'r','linewidth',0.5);
146 hold on
147 plot(Displ_1stload,Force_1stload_S,'r','linewidth',2);
148 xlabel('Displacement [mm]');
149 ylabel('Force [N]');
150 title([Wire_type ' ' Wire_size ' ' Wire_length ' sample '
        num2str(Sample) ' - load 1'], 'FontSize',28,'FontWeight','
        bold');
151 legend('Raw Data','Smooth Data','Location','northwest');
152 savefig('Force_Displ_1.fig')
153
154 %% Plot Motion capture deformation
155 Y_mat = 0;
156 X_mat = 0;
157
158 for i=1:length(time);
159     j = 1:10 ;
160     if time(i) <= time_1stload(end);
161         Y_mat(i,j) = -(y_r(i,10) - y_r(i,j));
162         X_mat(i,j) = x_r(i,j);
163     end
164 end
165
166
167 Y_mat = Y_mat - Y_mat(1,2);
168 X_mat = X_mat - X_mat(1,2);
169
170 X_mat_final = [X_mat(:,2) X_mat(:,4:8) X_mat(:,10)];
171 Y_mat_final = [Y_mat(:,2) Y_mat(:,4:8) Y_mat(:,10)];
172 k = round(linspace(1,length(Y_mat_final),5));
173 figure
174 for i=1:5
175     j = k(i);
176     plot(X_mat_final(j,:)*1e3,Y_mat_final(j,:)*1e3,'Color',
          Colors(i,:), 'MarkerSize',10);
177     hold on;
178     s(i) = scatter(X_mat_final(j,:)*1e3,Y_mat_final(j,:)*1e3,
                    'filled');
179     s(i).MarkerEdgeColor = 'b';
180     s(i).MarkerFaceColor = Colors(i,:);
181     hold on;
182

```

```

183 end
184 xlabel('X position [mm]');
185 ylabel('Y position [mm]');
186 title([Wire_type ' ' Wire_size ' MoCap ' Wire_length ' sample
        ' num2str(Sample)']);
187 savefig('MoCap.fig')
188
189 X_mat_f_1stload = X_mat_final(1:Peak_L1_I,:);
190 Y_mat_f_1stload = Y_mat_final(1:Peak_L1_I,:);
191
192 save data_all

```

## 2. Corrugated tube tensile test

Code for processing and plotting corrugated tube tensile test data:

```
1 % ==== SAI SIDDHARTHA VEMULA
2 % ==== Ohio State University
3 clc
4 clear all
5 close all
6
7 %% Read and plot data
8 MoCapfile = ''; % Input file name
9 MoCap = xlsread(MoCapfile);
10
11 time = MoCap(:,1); % Time in [secs]
12 Force = MoCap(:,2); % Force in [lbs]
13 Force_SI = Force*4.4482; % Force in [N]
14 Displ = MoCap(:,3); % Displacement in [in]
15 Displ_SI = Displ*25.4; % Displacement in [mm]
16
17 Force_SI = Force_SI-Force_SI(1);
18 Displ_SI = Displ_SI;
19
20 % Separate the data into 3 cycles
21 for i = 1:length(Force_SI)
22     if Displ_SI(i)<=18.75
23         Force_SI_1(i) = Force_SI(i);
24         Displ_SI_1(i) = Displ_SI(i);
25     elseif Displ_SI(i)>18.75 && Displ_SI(i)<=30.85
26         Force_SI_1(i) = Force_SI(i)+(31.33-30.86);
27         Displ_SI_1(i) = Displ_SI(i);
28     else
29         Force_SI_1(i) = Force_SI(i)+(31.33-30.86)
30             +(44.19-43.38);
31         Displ_SI_1(i) = Displ_SI(i);
32     end
33 end
34 % Load and unload division
35 [Peak_Force,Peak_index] = max(Force_SI);
36
37 j=1;k=1;
38 for i = 1:length(Force_SI)
39     if i<=Peak_index
40         Force_SI_Load(j) = Force_SI(i);
41         Displ_SI_Load(j) = Displ_SI(i);
```

```

42         Force_SI_Load_1(j) = Force_SI_1(i);
43         Displ_SI_Load_1(j) = Displ_SI_1(i);
44         j = j+1;
45     else
46         Force_SI_unload(k) = Force_SI(i);
47         k = k+1;
48     end
49 end
50
51 % Plotting the output
52 figure
53 plot(Displ_SI,Force_SI,'b');
54 hold on
55 plot(Displ_SI_1,Force_SI_1,'c');
56 grid on;
57 xlabel('Displacement [mm]')
58 ylabel('Force [N]')
59 title('Force v/s Displacement');
60 ylim([0 60]);
61 savefig('Force_Displ.fig')
62
63 figure
64 plot(Displ_SI_Load,Force_SI_Load,'b');
65 hold on
66 plot(Displ_SI_Load_1,Force_SI_Load_1,'c');
67 grid on;
68 xlabel('Displacement [mm]')
69 ylabel('Force [N]')
70 title('Force v/s Displacement');
71 ylim([0 60]);
72 savefig('Force_Displ_Load.fig')
73
74 save('Data','time','Force_SI','Displ_SI');

```

### 3. Twist tube tensile test

Code for processing and plotting twist tube tensile test data:

```
1  % ==== SAI SIDDHARTHA VEMULA
2  % ==== Ohio State University
3  clc
4  clear all
5  close all
6
7  %% Force-Disp Plot
8  a = xlsread(''); % raw data file name
9  Disp = a(:,1)-a(1,1);
10 Load = (a(:,2)-a(1,2))*1000;
11
12 %% Elastic region (Calculate stiffness of both the linear
    regions)
13 j=1;k=1;
14 for i =1:length(Disp)
15
16     if Disp(i)>2 && Disp(i)<8
17         Disp_e1(j) = Disp(i);
18         Force_e1(j) = Load(i);
19         j=j+1;
20     elseif Disp(i)>=10 && Disp(i)<20
21         Disp_e2(k) = Disp(i);
22         Force_e2(k) = Load(i);
23         k=k+1;
24     end
25 end
26
27 Y_modulus_1 = Disp_e1'\Force_e1';
28 Y_modulus_2 = Disp_e2'\Force_e2';
29
30 Y_modulus_1 = polyfit(Disp_e1,Force_e1,1);
31 Y_modulus_2 = polyfit(Disp_e2,Force_e2,1);
32
33 lin_Force_e1 = polyval(Y_modulus_1,Disp_e1);
34 lin_Force_e2 = polyval(Y_modulus_2,Disp_e2);
35 %% Load region
36 for i =1:length(Disp)
37
38     if Disp(i) <= 25
39         Disp_load(i) = Disp(i);
40         Force_load(i) = Load(i);
41     else
```

```

42         break;
43     end
44 end
45
46 figure
47 plot(Disp_load,Force_load,'r');
48 hold on;
49 grid on
50 xlabel('Displacement [mm]');
51 ylabel('Load [N]');
52 title('Force v/s Displacement');
53 savefig([name '_Load']);
54
55 figure
56 plot(Disp_load,Force_load,'r--');
57 hold on;
58 plot(Disp_e1,lin_Force_e1,'b');
59 plot(Disp_e2,lin_Force_e2,'b');
60 grid on
61 xlabel('Displacement [mm]');
62 ylabel('Load [N]');
63 title('Force v/s Displacement');
64 savefig([name '_Elastic']);

```

#### 4. Single wire analytical model

Analytical model code:

```
1 %%===== SAI SIDDHARTHA VEMULA
   =====
2 %%===== Analytical Model for plastic wire bending
   =====
3
4 clc
5 clear all
6 close all
7
8 %% Part 1: Initialization (Defining Inputs)
9
10 % Properties (Wire specific)
11 D_wire = ;
12 D_strand = ; % [m] Conductor strand
   radius;
13 K_w = 6; % No of strands in each
   layer
14 alpha(1:1:K_w(1)) = 0.2618; % [rads] lay angle of wire
   radians
15 layer_num = 1; % No of layers in the
   structure
16 Pc = 0.2;
17
18 % Properties (General)
19 ini_length = 85e-3; % [m] Initial length of the
   wire
20 ins_t = 0.3e-3; % [m] Insulation thickness
21 L_string = 760e-3; % [m] Axial length of the
   bundle
22 E_Cu = 110E9; % [Pa] Elastic modulus of
   Copper
23 E_ins = 1000E6; % [Pa] Elastic modulus of
   insulation
24
25 % Primary (AVSS) / Annealed steel
26 epsilon_Cu = []; % get from datasheet
27 [epsilon_Cu, index] = unique(epsilon_Cu);
28 E_Cu_t = []; % Get from datasheet
29 % Model parameters
30 mu_cc = 0.2; % [n/a] Cu-Cu coefficient
   of friction
```

```

31 mu_cp = 0.1; % [n/a] Cu-PVC coefficient
    of friction
32 Pc = 0.2; % [N] Normal force applied
    by insulation
33
34 %% Part 2a: Moment-Curvature formulation
35
36 % Required calculations
37 Tau = zeros(1,6); % [rads] Twist of the wire
    core
38 epsilon_ini = zeros(1,6); % Elongation of the wire
    core
39 R_w1 = D_strand; % [mm] Radius of circle for
    outer layer.
40 Kappa = linspace(0,35,10000); % [1/m] Curvature of the
    wire bundle
41 Area = pi*(D_strand^2)/4; % [mm^4] 0.5 mm^2
42 I_ins = (pi/64)*((D_wire)^4 ... % [m^4] MoI of insulation
    tube
    - (D_wire-2*ins_t)^4);
43 EI_ins = E_ins*I_ins; % [Nm^4] Stiffness of
    insulation tube
44
45
46 theta_w1 = [0 pi/3 2*pi/3 -pi/3 -2*pi/3 -pi];
47 % [rads] Angular positions of the wire strands
48
49 tic % To estimate the simulation time
50 for i = 1:length(Kappa)
51
52 %===== FIRST
    LAYER =====
53 %
    =====
54     for j = 1:K_w(1) % No of wire strands in the layer, 1st
        layer: 6
55
56         % Change in lay angle during bending
57         alpha_w1(j) = atan((tan(alpha(j))+R_w1*Tau(1))/(1+
            epsilon_ini(1)));
58
59         % Estimated elongation in the wire due to bending
60         epsilon_w1(i,j) = (cos(alpha_w1(j))^2)*(epsilon_ini
            (1)...
61             + R_w1*sin(theta_w1(j))*Kappa(i))...

```

```

62         + R_w1*sin(alpha_w1(j))*cos(alpha_w1(j))*Tau(1);
63 % Due to elongation [axial strain] +
64 % Due to bending [curvature
65 % Due to twisting [torsional strain] +
66
67 % Maximum Friction contact force
68 Tc_f(i,j) = ((mu_cp+mu_cc)*Pc)/(mu_cc*sin(alpha_w1(j)
69             ))*...
70             (exp(mu_cc*sin(alpha_w1(j))*theta_w1(j))-1);
71
72 % Estimated tension in the wire due to bending
73 Tc_b(i,j) = Area*E_Cu*Kappa(i)*R_w1*sin(theta_w1(j))
74             ...
75             *(cos(alpha_w1(j)))^2;
76
77 % Switching statement (From stick to slip)
78 if abs(Tc_b(i,j))<abs(Tc_f(i,j))
79     Tc(i,j) = Tc_b(i,j); % Stick state
80 else
81     Tc(i,j) = Tc_f(i,j); % Slip state
82 end
83
84 % Moment in the wire due to tension
85 M1(i,j) = Tc(i,j)*cos(alpha_w1(j))*R_w1*sin(theta_w1(
86     j));
87
88 % Minimum bending stiffness of the strand
89 h = D_strand;
90
91 kappa_no = Kappa(i)*cos(alpha_w1(j))*cos(theta_w1(j))
92     ;
93 kappa_bi = -Kappa(i)*(cos(alpha_w1(j))^2)*cos(
94     theta_w1(j));
95 epsilon_no(i,j) = (2*D_strand/(3*pi))*kappa_no;
96 epsilon_bi(i,j) = (D_strand/2)*kappa_bi;
97
98 div = 11;
99 y_Cu = linspace(0,h/2,div);
100
101 EJ_min1(i,j) = 0;
102 for ij = 1:length(y_Cu)
103     strain_Cu = y_Cu(ij)*Kappa(i);
104     del_y = y_Cu(2)-y_Cu(1);

```

```

102         E_Cu_n = interp1(epsilon_Cu, E_Cu_t(index), abs(
            strain_Cu)...
103         , 'linear', 'extrap');
104         EJ_min1(i, j) = (4*(E_Cu_n)*sqrt((h/2)^2 - y_Cu(ij)
            )^2)...
105         *(y_Cu(ij)^2)*del_y)*cos(alpha_w1(j))*1.06 +
            EJ_min1(i, j);
106
107     end
108
109 end
110 %
=====

111     alpha = alpha_w1;
112
113     EJ_core = E_Cu*pi*(h^4)/64;           % Stiffness of core
114
115     EJ_core = 0;
116     for ij = 1:length(y_Cu)
117
118         strain_Cu(ij) = y_Cu(ij)*Kappa(i);
119         del_y = y_Cu(2)-y_Cu(1);
120
121         E_Cu_n = interp1(epsilon_Cu, E_Cu_t(index), abs(
            strain_Cu(ij))...
122         , 'linear', 'extrap');
123         EJ_core = (4*(E_Cu_n)*sqrt((h/2)^2 - y_Cu(ij)^2)...
124         *(y_Cu(ij)^2)*del_y) + EJ_core;
125
126     end
127
128     Mom_bend_wir(i) = EJ_core*Kappa(i)+sum(EJ_min1(i,:))*
        Kappa(i);
129     Mom_bend_ins(i) = EI_ins*Kappa(i);
130     Mom_bend(i) = Mom_bend_wir(i) + Mom_bend_ins(i);
131
132     % Moment due to wire tension
133     Mom_tension(i) = sum(M1(i,:));
134
135     % Total Moment
136     Mom(i) = Mom_bend(i) + Mom_tension(i);
137
138     % Estimated bending moment
139     EJ_est(i) = Mom(i)/Kappa(i);

```

```

140
141 end
142 EJ_est(1) = EJ_est(2);
143 EJ_est_emp = gradient(Mom);
144 toc;
145
146 % Moment - Curvature
147 figure
148 plot(Kappa,Mom,'b')
149 hold on
150 grid on
151 xlabel('Curvature [1/m]');
152 ylabel('Moment [Nm]');
153 title('Moment v/s Curvature');
154
155 % Equivalent Stiffness - Curvature
156 figure
157 subplot(211)
158 plot(Kappa,EJ_est,'b');
159 hold on
160 xlabel('Curvature [1/m]');
161 ylabel('Bending Stifnness [Nm^2]');
162 title('Linear Plot')
163 subplot(212)
164 semilogx(Kappa,EJ_est,'b');
165 hold on
166 xlabel('Curvature [1/m]');
167 ylabel('Bending Stifnness [Nm^2]');
168 title('Log Plot')
169
170 figure
171 semilogx(Kappa,EJ_est*1e3,'b');
172 hold on
173 xlabel('Curvature [1/m]');
174 ylabel('Bending Stifnness [10^-^3 Nm^2]');
175 title('Linear Plot')
176
177 %% Part 3a: Force-Displacement conversion
178
179 tic
180 iter = 1000;
181 Load = linspace(0,0.5,iter);
182
183 defl_req = 0.050; % [m] Desired deflection

```

```

184 l = ini_length; % [m] Initial value of l =
    wire length
185 for j = 1:length(Load)
186
187     Load_new(j) = Load(j); % [N] Applied load
        in newtons
188     M(j) = Load_new(j)*l; % [Nm] Estimated
        moment
189
190     % Estimated stiffness [Nm^4]
191     EJ_new(j) = interp1(Mom,EJ_est,M(j),'linear','extrap');
192     curv_new(j) = interp1(Mom,Kappa,M(j),'linear','extrap');
193 %     EJ_new(j) = median(EJ_est);
194
195     a = Load_new(j)/(2*EJ_new(j));
196
197     % Length projected on x-axis [m]
198     l = fminsearch(@(l_xproj)x_projection(l_xproj,a,
        ini_length)...
199         ,ini_length);
200
201     % Beam position function
202     x_posn(j,:) = linspace(0,l,100);
203     dydx = @(x1) a.*x1.*(2.*l-x1) + 0.5*(a.*x1.*(2.*l-x1))
        .^3...
204     + (3/8).*(a.*x1.*(2.*l-x1)).^5 + (51/280).*(a.*x1.*(2.*l-
        x1)).^7;
205     for i = 1:size(x_posn,2)
206         y_posn(j,i) = quadgk(dydx,0,x_posn(j,i),...
207             'RelTol',1e-8,'AbsTol',1e-13);
208     end
209
210     % Termination condition
211     if y_posn(j,end)>defl_req % deflection > desired
        deflection
212         break;
213     end
214
215 end
216 toc
217
218 %% Part 3b: Plots
219 % Load-displacement plot
220 figure
221 plot(y_posn(:,end)*1e3,Load_new,'b-');

```

```

222 hold on;
223 grid on;
224 xlabel('Vertical deflection [mm]');
225 ylabel('Force [N]');
226 title('Force v/s Deflection');
227
228 %% ===== THE END
      =====

```

Large deflection function:

```

1 function L = x_projection(l,a,ini_length)
2
3     L_est = @(x) sqrt(1+(a.*x.*(2.*l-x) + 0.5*(a.*x.*(2.*l-x)
4         ).^3 + ...
5         (3/8).*(a.*x.*(2.*l-x)).^5 + (51/280).*(a.*x.*(2.*l-x)
6         ).^7).^2);
7     L2 = quadgk(L_est,0,l,'RelTol',1e-8,'AbsTol',1e-13);
8
9     L = abs(L2-ini_length);

```

## 5. Taped wire bundle characterization

For processing the motion capture data, code similar to the single wire experiment is used.

Code for plotting the force - displacement data:

```
1 % ==== SAI SIDDHARTHA VEMULA
2 % ==== Ohio State University
3 clc
4 clear all
5 close all
6
7 %% Data processing
8 load Motion_Capture
9 load ForceData
10
11 %% Calculate the net deflection of the tip from the fixed
    end;
12
13 tip_deflection = y_r(:,9) - y_r(:,1);
14 tip_deflection = tip_deflection - tip_deflection(1);%
    Normalize tip deflection
15 tip_deflection = tip_deflection*1e3;% from unit m to mm
16
17 %% devide cycles
18 j = 1;k = 1;n = 1;
19 [y_max,y_m_index] = max(tip_deflection(1:floor(length(time)
    /3+length(time)/8)));
20 Peak_M1 = time(y_m_index);
21 comp = Peak1-Peak_M1;
22
23 for i=1:length(time)
24
25     if(time(i)<Peak_M1+C_t)
26         cycle1_deflection(j) = tip_deflection(i);
27         cycle1_time(j) = time(i);
28         j=j+1;
29     elseif(time(i)>=Peak_M1+C_t && time(i)<Peak_M1+3*C_t)
30         cycle2_deflection(k) = tip_deflection(i);
31         cycle2_time(k) = time(i);
32         k=k+1;
33     elseif(time(i)>=Peak_M1+3*C_t && time(i)<Peak_M1+5*C_t)
34         cycle3_deflection(n) = tip_deflection(i);
35         cycle3_time(n) = time(i);
```

```

36         n=n+1;
37     end
38 end
39
40 % time in motion capture is lacking of the first 0.2 seconds,
    thus
41 % compensate here, which we can see from plot(time,
    tip_deflection)
42 cycle1_time = cycle1_time+comp;
43 cycle2_time = cycle2_time+comp;
44 cycle3_time = cycle3_time+comp;
45
46 % If cycle1_time < 0, eliminate these data
47 if cycle1_time(1) < 0;
48     index = find(cycle1_time>=0);
49     cycle1_time_N = cycle1_time(index);
50     cycle1_deflection_N = cycle1_deflection(index);
51 elseif cycle1_time(1) >= 0;
52     cycle1_time_N = cycle1_time;
53     cycle1_deflection_N = cycle1_deflection;
54 end
55 figure;
56 plot(cycle1_time_N,cycle1_deflection_N)
57
58 %%% To interpolate and call forces from force-time data
59
60 [cycle1_Force, cycle1_Force_S] = ForceDispLookup(
    cycle1_time_N);
61 [cycle2_Force, cycle2_Force_S] = ForceDispLookup(cycle2_time)
    ;
62 [cycle3_Force, cycle3_Force_S] = ForceDispLookup(cycle3_time)
    ;
63
64 % %%% Normalize force
65 F_ini = cycle1_Force(1);
66 F_ini_S = cycle1_Force_S(1);
67 cycle1_Force = cycle1_Force - F_ini;
68 cycle2_Force = cycle2_Force - F_ini;
69 cycle3_Force = cycle3_Force - F_ini;
70 cycle1_Force_S = cycle1_Force_S - F_ini_S;
71 cycle2_Force_S = cycle2_Force_S - F_ini_S;
72 cycle3_Force_S = cycle3_Force_S - F_ini_S;
73 for i=1:length(cycle1_Force)
74
75     if(cycle1_Force(i)<0)

```

```

76         cycle1_Force(i) = 0;
77     end
78     if(cycle1_Force_S(i)<0)
79         cycle1_Force_S(i) = 0;
80     end
81
82 end
83
84 for i=1:length(cycle2_Force)
85
86     if(cycle2_Force(i)<0)
87         cycle2_Force(i) = 0;
88     end
89     if(cycle2_Force_S(i)<0)
90         cycle2_Force_S(i) = 0;
91     end
92
93 end
94
95 for i=1:length(cycle3_Force)
96
97     if(cycle3_Force(i)<0)
98         cycle3_Force(i) = 0;
99     end
100    if(cycle3_Force_S(i)<0)
101        cycle3_Force_S(i) = 0;
102    end
103
104 end
105
106 Displ_all = [cycle1_deflection_N cycle2_deflection
              cycle3_deflection];
107 Force_all = [cycle1_Force cycle2_Force cycle3_Force];
108 Force_all_S = [cycle1_Force_S cycle2_Force_S cycle3_Force_S];
109 [Peak_L1,Peak_L1_I] = max(cycle1_deflection_N);
110 Peak_L1_I = Peak_L1_I - 45;
111 Displ_1stload = Displ_all(1:Peak_L1_I);
112 Force_1stload = Force_all(1:Peak_L1_I);
113 Force_1stload_S = Force_all_S(1:Peak_L1_I);
114 time_cycles = [cycle1_time_N,cycle2_time,cycle3_time];
115 time_cycles = time_cycles-time_cycles(1);
116 time_1stload = time_cycles(1:Peak_L1_I);
117 %% Plot displacement v/s Force
118
119 Colors = colormap(jet(11));

```

```

120 Colors = Colors([1:7,9:11],:);
121 Colors = flipud(Colors);
122 Colors = [Colors;[0 0 0]];
123 figure;
124 plot(cycle1_deflection_N,cycle1_Force,'r','linewidth',0.5)
125 hold on
126 plot(cycle1_deflection_N,cycle1_Force_S,'r','linewidth',2)
127 hold on
128 plot(cycle2_deflection,cycle2_Force,'b','linewidth',0.5)
129 hold on
130 plot(cycle2_deflection,cycle2_Force_S,'b','linewidth',2)
131 hold on
132 plot(cycle3_deflection,cycle3_Force,'g','linewidth',0.5)
133 hold on
134 plot(cycle3_deflection,cycle3_Force_S,'g','linewidth',2)
135 grid on;
136 xlabel('Displacement [mm]');
137 ylabel('Force [N]');
138 legend('Cycle 1: Raw Data','Cycle 1: Smooth Data','Cycle 2:
        Raw Data','Cycle 2: Smooth Data','Cycle 3: Raw Data','
        Cycle 3: Smooth Data','Location','northwest');
139 savefig('Force_Displ_allcycles.fig')
140
141 figure;
142 plot(Displ_1stload,Force_1stload,'r','linewidth',0.5);
143 hold on
144 plot(Displ_1stload,Force_1stload_S,'r','linewidth',2);
145 xlabel('Displacement [mm]');
146 ylabel('Force [N]');
147 legend('Raw Data','Smooth Data','Location','northwest');
148 savefig('Force_Displ_1stload.fig')
149
150 %% Plot Motion capture deformation
151 Y_mat = 0;
152 X_mat = 0;
153
154 for i=1:length(time);
155     j = 1:10 ;
156     if time(i) <= time_1stload(end);
157         Y_mat(i,j) = -(y_r(i,10) - y_r(i,j));
158         X_mat(i,j) = x_r(i,j);
159     end
160 end
161
162

```

```

163 Y_mat = Y_mat - Y_mat(1,2);
164 X_mat = X_mat - X_mat(1,2);
165
166 X_mat_final = [X_mat(:,2) X_mat(:,4:8) X_mat(:,10)];
167 Y_mat_final = [Y_mat(:,2) Y_mat(:,4:8) Y_mat(:,10)];
168 k = round(linspace(1,length(Y_mat_final),5));
169 figure
170 for i=1:5
171     j = k(i);
172     plot(X_mat_final(j,:)*1e3,Y_mat_final(j,:)*1e3,'Color',
          Colors(i,:), 'MarkerSize',10);
173     hold on;
174     s(i) = scatter(X_mat_final(j,:)*1e3,Y_mat_final(j,:)*1e3,
          'filled');
175     s(i).MarkerEdgeColor = 'b';
176     s(i).MarkerFaceColor = Colors(i,:);
177     hold on;
178
179 end
180
181 xlabel('X position [mm]');
182 ylabel('Y position [mm]');
183 title([Wire_type ' ' Wire_size ' MoCap ' Wire_length ' sample
        ' num2str(Sample)']);
184 savefig('MoCap.fig')
185
186 %% Save data file
187 save data_all

```

## 6. Composite wire bundle characterization

Code for processing the CWB three point bending test data:

```
1 % ==== SAI SIDDHARTHA VEMULA
2 % ==== Ohio State University
3 clc
4 clear all
5 close all
6
7 %% b.Read data from folder
8 Forcefile = '';
9 load(Forcefile);
10 %% c.Define X and Y, normalize, downsampling, smooth; and
    find the peak in cycle 1, then find the starting point
11 X = Force_data.X.Data;
12 X = X - X(1);
13 Y = Force_data.Y(2).Data;
14 figure;
15 plot(X,Y);
16
17 DS_ratio = 20;
18 Y_D = downsample(Y,DS_ratio);
19 X_D = downsample(X,DS_ratio);
20
21 m = -0.21082; c = 0.002846;
22 F_D = Y_D*m + c;
23 figure;
24 plot(X_D,F_D,'r');
25
26 [F_max,F_m_id] = max(F_D);
27 F_m_id = 25426;
28 delta_time = 58.8;
29 Start = max(find(X_D<=(X_D(F_m_id)-delta_time))));
30 Finish = max(find(X_D<=(X_D(F_m_id)+60))));
31
32 [F_min, F_min_id] = min(F_D);
33
34 X_N = X_D(Start:Finish);
35 X_N = X_N-X_N(1); %Normalize time again
36 F_N = F_D(Start:Finish);
37 F_N = F_N-F_N(1);
38
39 %% d.Define displacement based on crosshead speed 0.5mm/s for
    30mm displacement
40 j=1;k=1;
```

```

41 for i = 1:length(X_N)
42
43     if X_N(i)<=delta_time;
44         X_N_load(j) = X_N(i);
45         F_N_load(j) = F_N(i);
46         j = j+1;
47     else
48         X_N_Unload(k) = X_N(i);
49         F_N_Unload(k) = F_N(i);
50         k = k+1;
51     end
52 end
53
54 limit = (X_D(F_m_id)-X_D(Start))*0.5;
55
56 Load_N = linspace(0,limit,length(X_N_load));
57 Unload_N = linspace(limit,0,length(X_N_Unload));
58 Disp_N = [Load_N Unload_N];
59
60 % moving average filtered
61 F_NS_1l = smooth(F_N_load,0.05,'moving');
62 F_NS_1ul = smooth(F_N_Unload,0.05,'moving');
63 F_NS_1 = [F_NS_1l F_NS_1ul];
64 F_NS_1 = F_NS_1-F_NS_1(1);
65
66 %% e.Output Plots
67 figure;
68 plot(Disp_N,F_N,'b');
69 hold on;
70 % plot(Disp_N,F_NS,'r');
71 plot(Disp_N,F_NS_1,'r');
72 xlim([0 35]);
73 ylim([0 10]);
74 xlabel('Displacement [mm]');
75 ylabel('Force [N]');
76 title('Force v/s Displacement');
77 legend('Raw Data','Smooth Data');
78 savefig('Force_Displ.fig')
79
80 figure;
81 plot(Load_N,F_N_load,'b');
82 hold on;
83 % plot(Disp_N,F_NS,'r');
84 plot(Load_N,F_NS_1l,'r');
85 xlim([0 35]);

```

```
86 ylim([0 10]);
87 xlabel('Displacement [mm]');
88 ylabel('Force [N]');
89 title('Force v/s Displacement : Loading');
90 legend('Raw Data','Smooth Data');
91 savefig('Force_Load.fig')
92
93 save ForceData
```

## Appendix B: Cosserat simulation of wire harnesses

### B.1 Introduction

Potential future work of this research may include the development of analytical equations to model the harness as a homogenized entity such as a slender rod or a cylinder. Simulation of slender objects by modeling them as elastic rods has been explored by researchers in the field of computer graphics. These models are typically used to accurately simulate flexible objects in video games and VR environments. One such model includes the simulation of rods based on Cosserat theory. Pai [31] was the first to use Cosserat model in the field of computer graphics. He simulated the shape of sutures in laparoscopy for a surgical simulation system by modeling the sutures as one dimensional objects in a 3D space. His model was extended by Bertails et al. [4] to include the effect of dynamics and collision. Both these models use an implicit formulation. Gregoire and Schomer [14] modeled a cable as discretized linear elements with the position denoted by Cartesian coordinates and orientation denoted by quaternions. Their model was extended by Spillman and Teschner [37] to include dynamics.

## B.2 Modeling framework

An effort was made as part of this thesis to use the Cosserat model proposed by Spillman and Teschner [37] to model the harness as a homogenized cylinder. The harness is assumed to be made of linear rods connected together. The position of the rod is denoted by  $\mathbf{x}$  and the orientation of the rod is denoted by  $\mathbf{q}$ . Figure B.1 shows the proposed framework for simulating the harness shape.

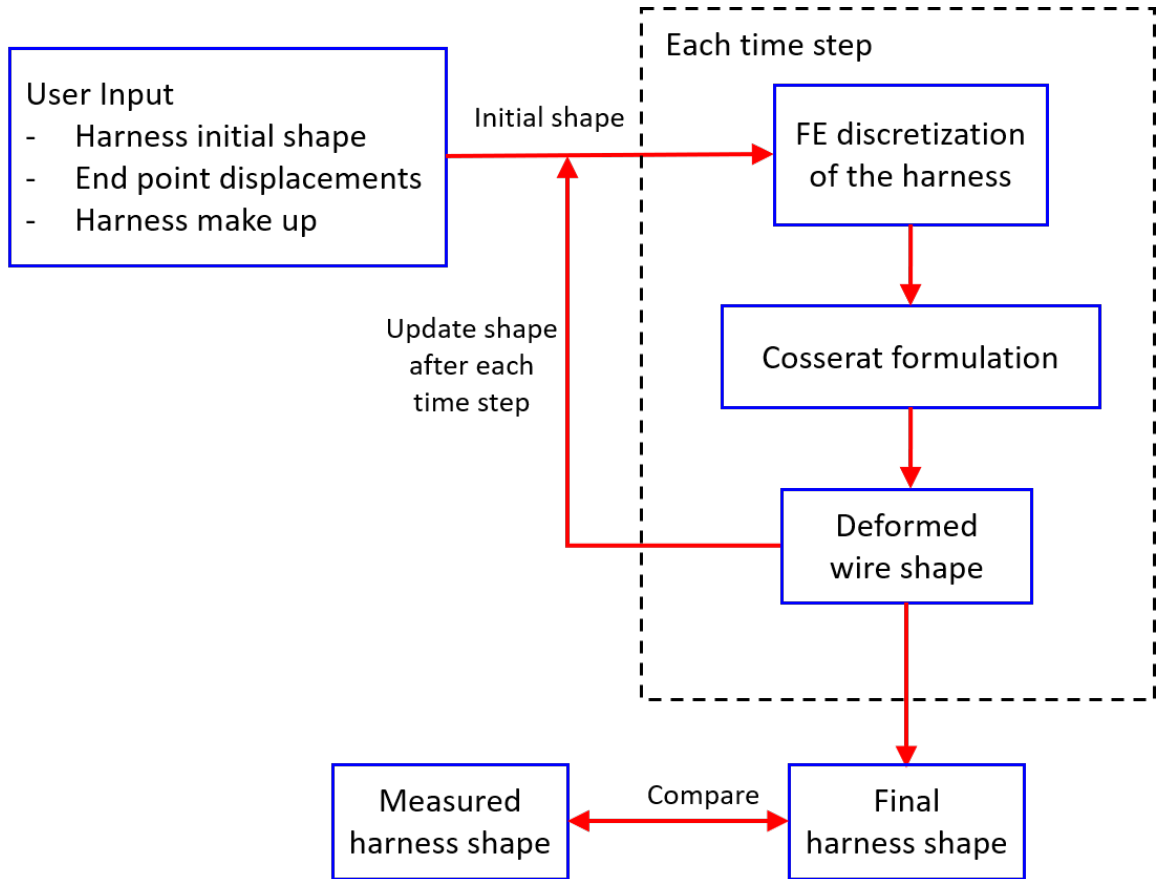


Figure B.1: Proposed harness simulation framework.

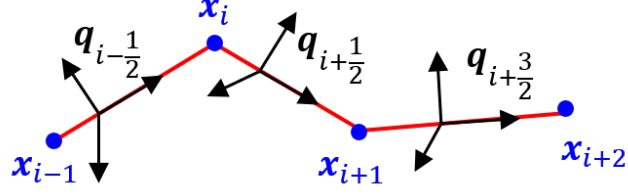


Figure B.2: A discrete Cosserat rod.

The initial shape of the harness is provided by the user. Based on the initial shape of the harness and the change in the boundary conditions the shape is updated according to the equation of the motion:

$$\begin{bmatrix} \mathbf{M} & -\mathbf{J}(\mathbf{x}^i)^T \\ \mathbf{J}(\mathbf{x}^i) & \alpha \end{bmatrix} \begin{Bmatrix} \Delta \mathbf{x} \\ \Delta \lambda \end{Bmatrix} = - \begin{Bmatrix} \mathbf{0} \\ \text{Constraints} \end{Bmatrix}. \quad (\text{B.1})$$

Where, the  $\mathbf{M}$  is the mass matrix,  $\mathbf{J}$  is the constrain Jacobian,  $\alpha$  is the compliance matrix,  $\mathbf{x}$  is the position vector,  $\lambda$  is the Lagrange multiplier and  $\lambda = -\alpha \mathbf{C}(\mathbf{x})$ , and  $\mathbf{C}(\mathbf{x})$  is the constraint matrix. The constrain matrix is made of two equations:

$$\mathbf{C} = - \left\{ \begin{array}{l} \mathbf{p}_i + \mathbf{x}_i - \mathbf{p}_{i+1} - \mathbf{x}_{i+1} \\ \frac{2}{l_i} \Im(\bar{q}_i q_{i+1} - \bar{q}_i^0 q_{i+1}^0) \end{array} \right\}. \quad (\text{B.2})$$

Where,  $\mathbf{x}_i$  and  $\mathbf{x}_{i+1}$  denote the initial position of the  $i^{\text{th}}$  and the  $(i+1)^{\text{th}}$  node respectively, similarly  $\mathbf{p}_i$  and  $\mathbf{p}_{i+1}$ ,  $q_i^0$  &  $q_{i+1}^0$  and  $q_i$  &  $q_{i+1}$  denote the initial and final quaternions of the  $i^{\text{th}}$  and the  $(i+1)^{\text{th}}$  elements respectively. The first constraint equation ensures the length of the element is constant after deformation and the second constraint equation ensures the updated quaternion has unit magnitude.

### B.3 Preliminary results

As part of a preliminary investigation into the modeling of harnesses using Cosserat theory, a simple simulation was performed by ignoring the affect of rotation. The study involved simulating a chain being lifted off a table by holding it at the centre. The results are shown in Figure B.3.

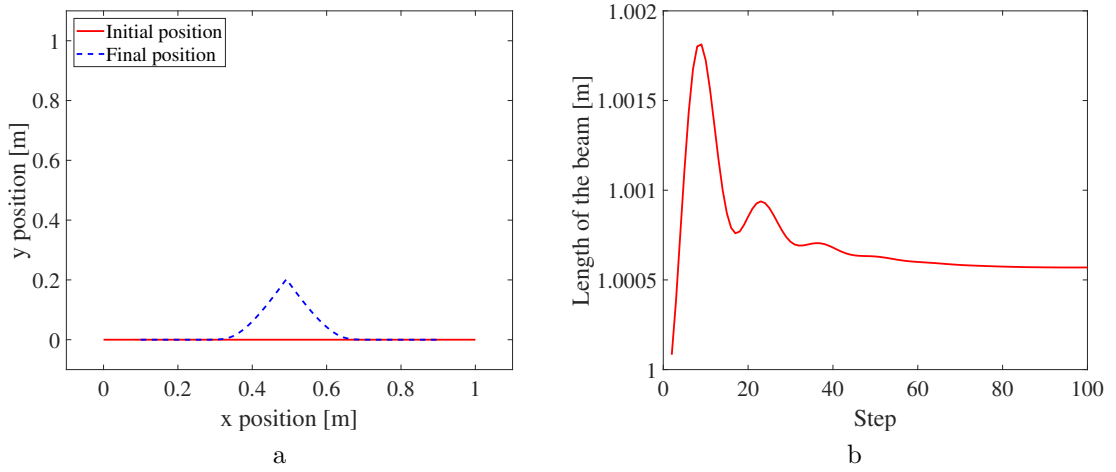


Figure B.3: (a) The initial and final shape of a chain being lifted off a table and (b) the variation in the chain length.

The preliminary results show a good agreement with expected shape and the variation in the chain length is also minimal. This model can potentially be extended to simulating the wire harness by including the effect of rotation.

## Bibliography

- [1] M.H. Ang, W. Wei, and L. Teck-Seng. On the estimation of the large deflection of a cantilever beam. In *Industrial Electronics, Control, and Instrumentation, 1993. Proceedings of the IECON'93., International Conference on*, pages 1604–1609. IEEE, November 1993.
- [2] Standard Test Methods for Tensile Testing of High Performance Polyethylene Tapes. Standard, ASTM International, West Conshohocken, PA, 2011.
- [3] Standard Test Methods for Flexural Properties of Unreinforced and Reinforced Plastics and Electrical Insulating Materials. Standard, ASTM International, West Conshohocken, PA, 2017.
- [4] Florence Bertails, Basile Audoly, Marie-Paule Cani, Bernard Querleux, Frédéric Leroy, and Jean-Luc Lévêque. Super-helices for predicting the dynamics of natural hair. *ACM Transactions on Graphics (TOG)*, 25(3):1180–1187, 2006.
- [5] A. Colozza. Wire and cable cold bending test. Technical Report NASA/CR-2010-216086, Analex Corporation, 2010.
- [6] G. A. Costello. Analytical investigation of wire rope. *Applied Mechanics Review*, 31(7):897–900, 1978.

- [7] A. Dean, D. Voss, and D. Draguljić. *Design and analysis of experiments*, volume 1. Springer, 2nd edition, 2017.
- [8] J.H. Derr, C.M. Straub, and S. Ahmed. Prediction of wiring harness reliability. *SAE Transactions*, pages 218–226, 1987.
- [9] V. Dörlich, J. Linn, T. Scheffer, and Stefan D. Towards viscoplastic constitutive models for Cosserat rods. In *ECCOMAS Thematic Conference on Multibody Dynamics*, 2015.
- [10] F. Foti and L. Martinelli. An analytical approach to model the hysteretic bending behavior of spiral strands. *Applied Mathematical Modelling*, 40(13-14):6451–6467, 2016.
- [11] F. Foti and L. Martinelli. Mechanical modeling of metallic strands subjected to tension, torsion and bending. *International Journal of Solids and Structures*, 91:1–17, 2016.
- [12] G. Goebbels, M. Göbel, T. Hambürger, N. Hornung, U. Klein, I. Nikitin, O. Rat-tay, J. Scharping, K. Troche, and C. Wieness. Real-time dynamics simulation of cables, hoses and wiring harnesses for high accuracy digital mock-ups and load analysis. In *Proceedings of Automotive Power Electronics*, 2007.
- [13] V. G. A. Goss, G. H. M. van der Heijden, J. M. T. Thompson, and S. Neukirch. Experiments on snap buckling, hysteresis and loop formation in twisted rods. *Experimental Mechanics*, 45(2):101–111, 2005.
- [14] Mireille Grégoire and Elmar Schömer. Interactive simulation of one-dimensional flexible parts. *Computer-Aided Design*, 39(8):694–707, 2007.

- [15] T. Hermansson, J. S. Carlson, S. Björkenstam, and R. Söderberg. Geometric Variation Simulation and Robust Design for Flexible Cables and Hose. *Journal of Engineering Manufacture*, 227(5):681 – 689, 2013.
- [16] John H Hollomon. Tensile deformation. *Aime Trans*, 12(4):1–22, 1945.
- [17] K.J. Hong, A.D. Kiureghian, and J.L. Sackman. Bending behavior of helically wrapped cables. *Journal of Engineering Mechanics*, 131(5):500–511, 2005.
- [18] W. Huang and R. Xu. Two personification strategies for solving circles packing problem. *Science in China Series E: Technological Sciences*, 42(6):595–602, 1999.
- [19] K. Inagaki, J. Ekh, and S. Zahrai. Mechanical analysis of second order helical structure in electrical cable. *International Journal of Solids and Structures*, 44(5):1657–1679, 2007.
- [20] T. Inoue, Y. Kawakita, H. Kawabe, Y. Kohtake, M. Furusyo, K. Ohuchi, and M. Kaji. The development of a method to estimate the bending reliability of wiring harness. *SAE Transactions*, 109(7):252–256, 2000.
- [21] W.G. Jiang. A concise finite element model for pure bending analysis of simple wire strand. *International Journal of Mechanical Sciences*, 54(1):69–73, 2012.
- [22] F.J. Kampas, J.D. Pintér, and I. Castillo. Optimal packing of general ellipses in a circle. In *Modeling and Optimization: Theory and Applications*, pages 23–37. Springer, 2016.
- [23] B. S. Kim, K. Park, and Y. W. Kim. Endurance Analysis of Automotive Vehicle’s Door W/H System Using Finite Element Analysis. *Journal of Software Engineering and Applications*, 2(5):375–382, 2009.

- [24] A. Labuschagne, N.J van Rensburg, and A.J. Van der Merwe. Comparison of linear beam theories. *Mathematical and Computer Modelling*, 49(1-2):20–30, 2009.
- [25] J. Lanteigne. Theoretical estimation of the response of helically armored cables to tension, torsion, and bending. *Journal of Applied Mechanics*, 52(2):423–432, 1985.
- [26] S.W.S. Ltd. *Wires and cables for automobiles*, April 2016.
- [27] K. G. McConnell and W. P. Zemke. The measurement of flexural stiffness of multistranded electrical conductors while under tension. *Experimental Mechanics*, 20(6):198–204, 1979.
- [28] B. L. Narayana, W. G. Strang, and A. Bhatia. Non-Linear Finite Element Analysis of Typical Wiring Harness Connector and Terminal Assembly Using ABAQUE/CAE and ABAQUS STANDARD. In *ABAQUS Users’ Conference*, 2006.
- [29] Inc. DBA OptiTrack NaturalPoint. Camera placement, 2016.
- [30] Inc. DBA OptiTrack NaturalPoint. Flex 13 parameters, 2016.
- [31] Dinesh K Pai. Strands: Interactive simulation of thin solids using cosserat models. In *Computer Graphics Forum*, volume 21, pages 347–352. Wiley Online Library, 2002.
- [32] K.O. Papailiou. On the bending stiffness of transmission line conductors. *IEEE Transactions on Power Delivery*, 12(4):1576–1588, 1997.

- [33] L.A. Pipes. The reversion method for solving nonlinear differential equations. *Journal of Applied Physics*, 23(2):202–207, 1952.
- [34] A. Pradhan. Current trends in automotive wire harness design. In *Proceedings of the International Conference on Mechanical, Production and Automobile Engineering (ICMPAE 2011), Pattaya, Thailand*, pages 28–29, 2011.
- [35] U. Rothenburg, U. Völlinger, B. Beckmann-Dobrev, Figge A., and G. Goebbels. Validation of accuracy simulating flexible, one-dimensional objects. In *Proceedings of Virtual Reality International Conference (VRIC 2010)*, 2010.
- [36] Kaitlin S Spak, Gregory S Agnes, and Daniel J Inman. Modeling vibration response and damping of cables and cabled structures. *Journal of Sound and Vibration*, 336:240–256, 2015.
- [37] Jonas Spillmann and Matthias Teschner. Corde: Cosserat rod elements for the dynamic simulation of one-dimensional elastic objects. In *Proceedings of the 2007 ACM SIGGRAPH/Eurographics symposium on Computer animation*, pages 63–72, 2007.
- [38] B. Štok and M. Halilović. Analytical solutions in elasto-plastic bending of beams with rectangular cross section. *Applied Mathematical Modelling*, 33(3):1749–1760, 2009.
- [39] E. Taghipour, S.S. Vemula, Z. Wang, Y. Zhou, H. Qarib, K. Gargesh, L.M. Headings, M.J. Dapino, and S. Soghrati. Characterization and computational modeling of electrical wires and wire bundles subject to bending loads. *International Journal of Mechanical Sciences*, 140:211–227, 2018.

- [40] A. Theetten, L. Grisoni, C. Andriot, and B. Barsky. Geometrically exact dynamic splines. *Computer-Aided Design*, 40(1):35 – 48, 2008.
- [41] S. Timoshenko. *History of strength of materials: with a brief account of the history of theory of elasticity and theory of structures*. Courier Corporation, 1983.
- [42] G.H.M. van der Heijden, S. Neukirch, V.G.A. Goss, and J.M.T. Thompson. Instability and self-contact phenomena in the writhing of clamped rods.
- [43] S.A. Velinsky. General nonlinear theory for complex wire rope. *International Journal of Mechanical Sciences*, 27(7-8):497–507, 1985.
- [44] H. Wang, W. Huang, Q. Zhang, and D. Xu. An improved algorithm for the packing of unequal circles within a larger containing circle. *European Journal of Operational Research*, 141(2):440–453, 2002.
- [45] C. Wienss, M. Göbel, and G. Goebbels. Simulation of wiring harnesses and hoses for product design and manufacturing. In *International Conference; 3rd, Supply on the wings; AIRTEC International Aerospace Supply Fair conference proceedings*, 2008.
- [46] R. N. Wright and K. Patenaude. Tensile properties of insulated electrical conductor. *Wire Journal International*, 34(5):94–96, 2001.
- [47] Yitong Zhou et al. Mechanical characterization of automotive electrical wires and wire harnesses. Master’s thesis, The Ohio State University, 2016.